Department of Physics and Astronomy

University of Heidelberg

Master Thesis

in Physics

submitted by

Tilman Hartwig

born in Karlsruhe

– 2014 –

Improving Optically Thick H_2 Line Cooling in Simulations of Primordial Star Formation and its Effect on Fragmentation

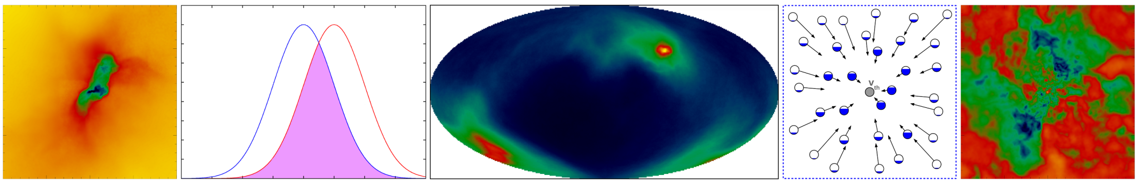

This Master Thesis has been carried out by Tilman Hartwig

at the

Institute of Theoretical Astrophysics

under the supervision of

Prof. Dr. Ralf S. Klessen

Improving Optically Thick H_2 Line Cooling in Simulations of Primordial Star Formation and its Effect on Fragmentation:

Primordial star formation is an important field of current research, because the properties of these first stars influence the chemical enrichment, turbulent mixing, and reionisation of the primordial gas. Therefore, they define the initial conditions for subsequent star and galaxy formation.

Molecular hydrogen (H_2) is the dominant coolant in primordial gas. When the H_2 lines become optically thick at high densities, we need a special numerical treatment in order to model H_2 cooling accurately. In order to do so, we implement a new method for the determination of effective column densities in the SPH code Gadget2. This new method directly sums up matter contributions and weights them with the relative spectral line overlap. A comparison to commonly used local, isotropic methods shows that these local methods generally underestimate the photon escape fraction, because they miss the flattening of the cloud. While analytical fit formulas break down completely (mean relative error of 20–70%), we find that a combination of the Sobolev and Gnedin approximation might fit the exact results (mean relative error of 5–20%).

Our new method yields lower temperatures in the centre of the cloud and hence promotes fragmentation in the density regime $10^{10}\,\mathrm{cm}^{-3} \leq n \leq 10^{12}\,\mathrm{cm}^{-3}$. This is why we expect Pop III stars to have lower masses than previously thought.

Verbesserung der Sobolev-Näherung zur Bestimmung der effektiven Säulendichte in primordialen Sternentstehungssimulationen und deren Einfluss auf Fragmentation:

Sternentstehung im frühen Universum ist von besonderer Bedeutung, da diese ersten Sterne das interstellare Medium ionisieren und mit schweren Elementen anreichern. Dadurch beeinflussen sie maßgeblich die Entstehung weiterer Sterne und Galaxien.

Primordiales Gas kühlt vor allem durch Roto-Vibrations-Übergänge des molekularen Wasserstoffs. Ab einer bestimmten Dichte wird dieser jedoch optisch dicht und die Photonen können der Wolke nicht mehr ungehindert entweichen. Die Wahrscheinlichkeit der Photonen zu entweichen muss dann über die Säulendichte berechnet werden. Dazu entwickeln wir eine neue Methode, welche das Gas entlang der Sichtlinien aufsummiert und mit dem entsprechenden Überlapp der Spektrallinien gewichtet. Diese sehr genaue Methode vergleichen wir mit bisher üblichen Näherungen (Sobolev, Gnedin, analytische Formeln) und kommen zu dem Ergebnis, dass diese Näherungen die Wahrscheinlichkeit der Photonen zu entweichen unterschätzen. Während die analytischen Formeln um 20-70% abweichen, erzielt eine Kombination aus Gnedin- und Sobolev-Näherung gute Ergebnisse mit Fehlern von lediglich 5-20%.

Die Verwendung unserer neuen Methode liefert deutlich niedrigere Temperaturen im Innern der Wolke. In einem Dichtebereich von $10^{10}\,\mathrm{cm}^{-3} \leq n \leq 10^{12}\,\mathrm{cm}^{-3}$ kann das Gas somit leichter fragmentieren, woraus wir folgern, dass die ersten Sterne leichter sind als bisher angenommen.

Contents

1 Introduction

1.1 Motivation

Where does the first light in the Universe come from? This question is not only of general interest, but is also a focus of current research in astrophysics. The first stars in the Universe are so called Population III (or Pop III) stars. They emerged several hundred million years after the big bang and dramatically changed the physical conditions of their environment. Their birth marks the transition from the so called "Dark Ages" of the Universe towards the manifoldness we can observe nowadays. Since the chemical composition of the primordial gas and the physical properties of star forming regions in the early Universe are fundamentally different from the present-day ones, Pop III star formation is an independent field of current research. The importance of this topic is based on several aspects. On the one hand, the properties of Pop III stars have a fundamental influence on many subsequent physical processes:

- Synthesis of heavy elements and enrichment of the interstellar medium (Umeda & Nomoto 2003; Whalen et al. 2008b; Stacy et al. 2013; Hirano et al. 2013; Stacy & Bromm 2013).
- Formation of the next generation of stars (Glover 2013; Hirano et al. 2013).
- Reionisation of the Universe (Schaerer 2002; Schleicher et al. 2008a; Whalen et al. 2008a; Stacy et al. 2013; Hirano et al. 2013; Stacy & Bromm 2013).
- Assembly of the first galaxies (Whalen et al. 2008b; Glover 2013).
- Influences the polarization (Bromm 2013) and the power spectrum (Schleicher et al. 2008b) of the cosmic microwave background.
- Super massive black hole formation (Schleicher et al. 2013; Latif et al. 2013a; Hirano et al. 2013; Latif et al. 2013b).

On the other hand, we hardly understand many crucial processes characterising Pop III star formation (see Glover et al. (2008) for a compilation of these open questions). Already Sobolev (1960) pointed out that "one of the chief needs of theoretical astrophysics at the present time is, in my opinion, the development of the theory of radiative equilibrium for a moving medium". Although progress has been made regarding this problem, it is not yet completely solved. Especially the influence of optically thick H_2 cooling in primordial star formation is an open

question according to Glover (2013) and will be addressed in this Master Thesis.
A main outcome of a consistent theory of Pop III star formation is the primordial initial mass function, which assigns the number of expected stars to each mass bin. Especially in a primordial environment without any metals, the mass of a Pop III star is the crucial parameter which defines its luminosity, temperature, spectrum, radius, lifetime and its final fate. An overview of the individual mass ranges, proposed by different authors, can be seen in Figure 1.1. The significant variations and uncertainties in the mass ranges reveal the lack of understanding of the primordial gas' fragmentation behaviour. Fragmentation as an open question in Pop III star formation was already mentioned by Abel et al. (2000); Ripamonti & Abel (2004); Omukai et al. (2005); Glover et al. (2008); Clark et al. (2011a); Smith et al. (2011); Greif et al. (2012, 2013); Machida & Doi (2013) and will be addressed in this Master Thesis.

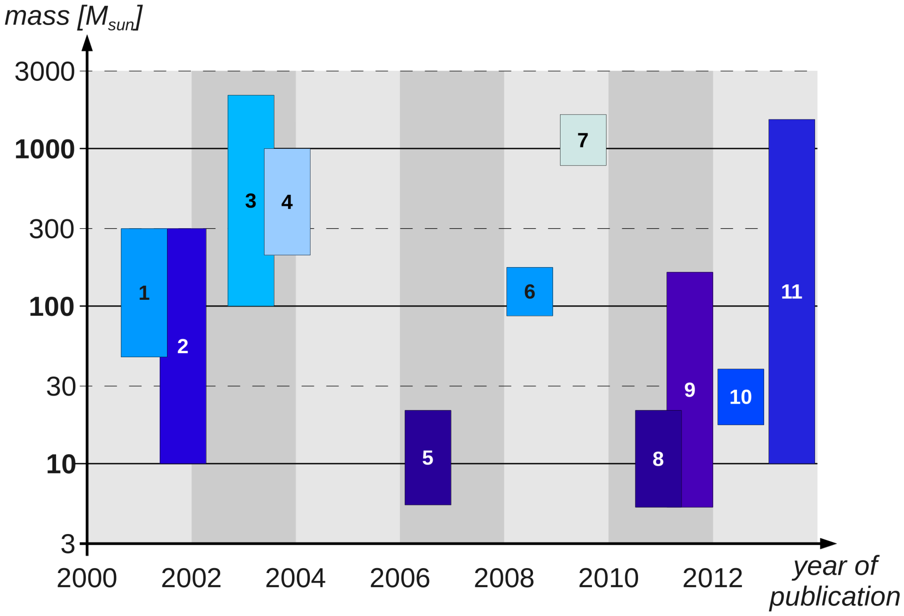

Figure 1.1: Expected mass range of primordial star formation as a function of publication year. The indicated mass ranges are only rough estimates and sometimes rely on different assumptions. The idea of this plot is based on a slide by Naoki Yoshida, complemented with data by Bromm et al. (2001) [1], Omukai & Palla (2001) [2], Omukai & Palla (2003) [3], Omukai & Yoshii (2003) [4], Johnson & Bromm (2006) [5], McKee & Tan (2008) [6], Ohkubo et al. (2009) [7], Clark et al. (2011a) [8], Greif et al. (2008) [9], Hosokawa et al. (2012) [10], Hirano et al. (2013) [11].

1.2 Cosmological Structure Formation

Early in the Universe, matter was almost homogeneously distributed. Recently, the Planck satellite analysed temperature fluctuations of the cosmic microwave background (CMB) as a footprint of the tiny but crucial inhomogeneities (Figure 1.2). According to the standard model of cosmology, structure has formed hierarchically from those small density fluctuations. The subsequent merging of successively larger structures formed the Universe as we know it today. In order to understand the theoretical framework, the thermal evolution and non-linear structure formation, we want to introduce the basic principles in cosmology (mainly based on Bartelmann 2007, 2009; Clark & Glover 2013; Glover 2013).

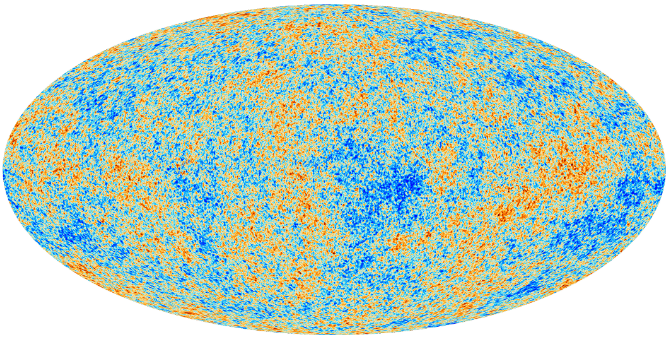

Figure 1.2: Map of temperature fluctuations of the CMB spectrum, showing tiny inhomogeneities about 378000 years after the big bang. The fluctuations are of the order of $\Delta T/T \simeq 10^{-5}$ (ESA and the Planck Collaboration 2013).

1.2.1 Cosmological Framework

The standard model of cosmology is based on two assumptions:

1. On sufficiently large scales, the Universe is isotropic.
2. The position from where we observe the Universe is by no means preferred to any other position (Copernican principle).

These two fundamental assumptions are commonly summarised by claiming that the Universe is “homogeneous and isotropic” (cosmological principle). The only relevant force on cosmological scales is gravity. Due to the cosmological principle, gravity can be described by a Robertson-Walker metric

$$g = -c^2 \mathrm{d}t^2 + a(t)^2 \left[\mathrm{d}w^2 + f_k(w)^2 \left(\mathrm{d}\theta^2 \sin^2\theta \mathrm{d}\phi^2\right)\right] , \tag{1.1}$$

where $a(t)$ is the scale factor and $f_k(w)$ is a function, which depends on the radial coordinate w and the curvature of space-time. Since the Universe expands (or might shrink), the scale factor describes its relative size ($a_{\text{today}} = 1$). The whole dynamics of the Universe is reduced to the dynamics of the scale factor $a(t)$, which can be described by the Friedmann equations

$$\frac{\dot{a}(t)^2}{a(t)^2} = \frac{8\pi G}{3}\rho(t) - \frac{kc^2}{a(t)^2} + \frac{\Lambda}{3}, \tag{1.2}$$

$$\frac{\ddot{a}(t)}{a(t)} = -\frac{4\pi G}{3}\left(\rho(t) + \frac{3p(t)}{c^2}\right) + \frac{\Lambda}{3}, \tag{1.3}$$

where G is the gravitational constant, $\rho(t)$ is the matter density, k parametrises the curvature of space-time, Λ is the cosmological constant and $p(t)$ the pressure. The Friedmann equations can be combined to the adiabatic equation

$$\frac{\mathrm{d}}{\mathrm{d}t}\left(a(t)^3\rho(t)c^2\right) + p(t)\frac{\mathrm{d}}{\mathrm{d}t}\left(a(t)^3\right) = 0, \tag{1.4}$$

which can be interpreted by means of energy conservation. For non-relativistic matter the adiabatic equation yields the time-dependent matter density $\rho_m(t) = \rho_{m,0}a^{-3}$, whereas for relativistic matter it yields $\rho_r(t) = \rho_{r,0}a^{-4}$ with the current matter density $\rho_{m,0}$ and current energy density of radiation $\rho_{r,0}$. Since the individual energy contributions scale with different powers of a, we can distinguish different epochs in cosmic history and derive their expansion behaviour. The early Universe ($t \lesssim 522$yr) is dominated by the radiation energy density and the time evolution of the scale factor in this epoch is given by $a \propto t^{1/2}$, whereas the epoch thereafter is dominated by matter and the scale factor evolves as $a \propto t^{2/3}$ (Einstein-de Sitter limit). The spectrum of distant galaxies is redshifted because, due to the expansion of the Universe, they are moving away from us (the faster, the farer away they are). This redshift z is related to the scale factor of the Universe at emission of the photons by

$$1 + z = \frac{1}{a} \tag{1.5}$$

and therefore represents a commonly used measurement for the age of the Universe.

1.2.2 Thermal and Chemical Evolution

A fundamental parameter for the description of the thermal and chemical evolution of the Universe is obviously the temperature. According to the Stefan-Boltzmann law, the energy density of radiation scales as $\rho_r \propto T^4$, whereas we have seen above that it also relates to the scale factor by $\rho_r \propto a^{-4}$. Combining these two relations and using Equation 1.5 we derive

$$T_r \propto 1 + z, \tag{1.6}$$

which states that the Universe was hotter in the past. For a non-relativistic gas with adiabatic index $\gamma = 5/3$ the relation

$$T_m \propto (1+z)^2 \tag{1.7}$$

describes the temperature evolution. The Universe has to evolve adiabatically on large scales, because any heat flow might violate the cosmological principle.

The Universe starts in a very hot, dense state and cools by expanding afterwards. Hence, different particle species freeze out at different times, because the temperature drops and they are no longer in thermal equilibrium. Once the temperature drops below $Tk_B \simeq 800\mathrm{keV}$ the equilibrium between protons and neutrons can no longer be maintained. At the moment of "freeze-out", the neutron-to-proton number density is given by

$$\frac{n_n}{n_p} = e^{-\Delta mc^2/k_BT} \simeq \frac{1}{6}, \tag{1.8}$$

where $\Delta mc^2 \simeq 1.4\mathrm{MeV}$ is the mass difference between neutrons and protons. Since nuclear fusion becomes efficient at a temperature of $Tk_B \simeq 80\mathrm{keV}$ (about three minutes after the big bang), some free neutrons have time to decay and the final neutron-to-proton ratio is

$$\frac{n_n}{n_p} \simeq \frac{1}{7}. \tag{1.9}$$

At this point, nucleosynthesis fuses the existing particles to isotopes and heavier elements, which can be seen in Figure 1.3. Hence, the primordial gas consists of roughly 76% hydrogen atoms, 24% helium atoms and tiny traces of other isotopes

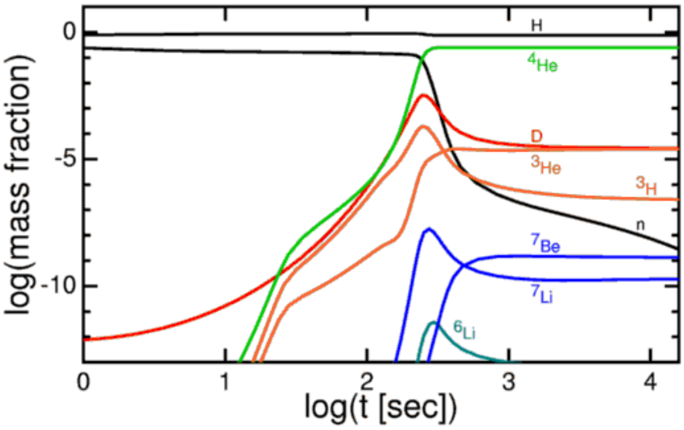

Figure 1.3: Fractional abundance of different primordial species as a function of time for the standard cosmological model. Adopted by Wright (2012).

and elements. The gas is still ionised until the reaction

$$\mathrm{H}^+ + \mathrm{e}^- \leftrightarrow \mathrm{H} + \gamma \tag{1.10}$$

freezes out and the gas recombines. This recombination process can be described by the Saha equation and is delayed due to the very large photon-to-baryon ratio. Recombination occurs at $z = 1100 \pm 80$, which corresponds to 378000 years after the big bang. Beyond this point, the gas is mainly neutral, until the first stars will reionise it again.

1.2.3 Jeans Analysis

Obviously (and luckily), the Universe is not completely homogeneous. Even on astronomical scales we observe inhomogeneous, filamentary structures as you can see in Figure 1.4. In order to understand structure formation, we first have to review the governing physics. The main set of equations are the equation of state and the equations of hydrodynamics, which are discussed in section 3.1.1. In a first, linear approximation we derive the evolution of small perturbations in density

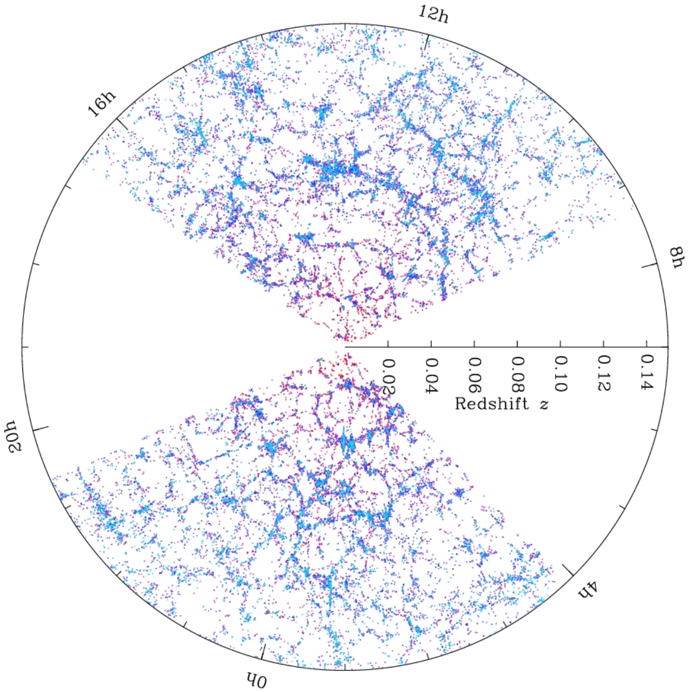

Figure 1.4: Large scale structure in the northern equatorial slice of the SDSS main galaxy redshift sample. The slice is 2.5 ° thick and galaxies are colour-coded by luminosity. Adopted by SDSS (2008).

$$\rho(\vec{x}, t) = \rho_0(t) + \Delta\rho(\vec{x}, t) \tag{1.11}$$

and expansion velocity

$$\vec{v}(\vec{x},t) = \vec{v_0}(t) + \Delta\vec{v}(\vec{x},t). \tag{1.12}$$

By defining the density contrast

$$\delta = \frac{\Delta\rho}{\rho_0}, \tag{1.13}$$

using the isothermal equation of state $p = \rho_0 c_s^2$ with the sound speed c_s and neglecting all quadratic terms in the perturbations, we derive the second-order differential equation

$$\ddot{\delta} + 2H\dot{\delta} = \left(4\pi G\rho_0 + \frac{c_s^2\nabla^2\delta}{a^2}\right), \tag{1.14}$$

where $H = \dot{a}/a$ is the Hubble function. On large scales in an Einstein-de Sitter Universe, $\delta(z) = \delta_0(1+z)^{-1}$ solves this equation, which indicates the growth of density perturbations with time. Decomposing Equation 1.14 into a set of plane waves

$$\delta(\vec{x},t) = \int \frac{\mathrm{d}\vec{k}}{(2\pi)^3}\hat{\delta}(\vec{k},t)e^{-i\vec{k}\vec{x}}, \tag{1.15}$$

yields

$$\ddot{\hat{\delta}} + 2H\dot{\hat{\delta}} = \left(4\pi G\rho_0 - \frac{c_s^2 k^2\hat{\delta}}{a^2}\right). \tag{1.16}$$

Identifying the right hand side of this equation as the source term of a damped harmonic oscillator equation, the criterion of growing density perturbations is

$$k < k_J = \frac{2\sqrt{\pi G\rho_0}}{c_s}. \tag{1.17}$$

Alternatively, we can define the Jeans length according to

$$\lambda_J = \frac{2\pi}{k_J} = c_s\sqrt{\frac{\pi}{G\rho_0}}. \tag{1.18}$$

Perturbations smaller than the Jeans length oscillate, whereas perturbations larger than the Jeans length collapse. In a similar fashion we define the Jeans mass

$$M_J = \frac{4\pi}{3}\rho_0\left(\frac{\lambda_J}{2}\right)^3 = \frac{\pi^{5/2}}{6G^{3/2}}c_s^3\rho_0^{-1/2} \tag{1.19}$$

that describes the minimum mass that a density perturbation must have in order to collapse under its own gravity. At high redshift $z \gg 100$ the Jeans mass is given by (Barkana & Loeb 2001)

$$M_J = 1.35 \times 10^5 \left(\frac{\Omega_m h^2}{0.15}\right)^{-1/2} M_\odot, \tag{1.20}$$

where Ω_m is the dimensionless cosmological matter density parameter, and h is the value of the Hubble constant in units of $100 \mathrm{kms}^{-1}\mathrm{Mpc}^{-1}$. In the low redshift limit ($z < 100$), the Jeans mass is given instead by (Glover 2013)

$$M_J = 5.18 \times 10^3 \left(\frac{\Omega_m h^2}{0.15}\right)^{-1/2} \left(\frac{\Omega_b h^2}{0.026}\right)^{-3/5} \left(\frac{1+z}{10}\right)^{3/2} M_\odot, \tag{1.21}$$

where Ω_b is the dimensionless cosmological baryon density parameter. The evolution of the Jeans mass with redshift can be seen in Figure 1.5.

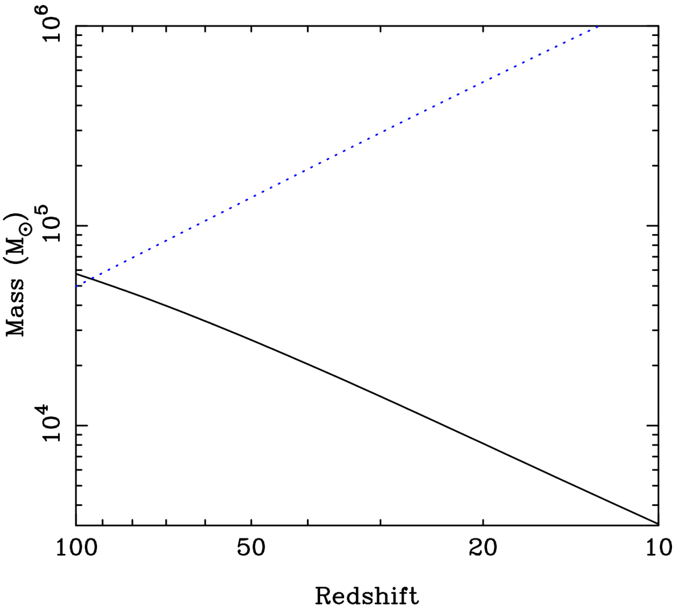

Figure 1.5: Jeans mass (solid line) and critical minihalo mass (see Equation 1.41), required for efficient H_2 cooling (dotted line) as a function of redshift. Adopted by Glover (2013).

1.2.4 Non-Linear Structure Formation

In order to derive Equation 1.14 we had to assume $|\delta| \ll 1$. Since δ can become arbitrarily large, we have to find a different description for structure formation in the non-linear regime. One common approach is the spherical collapse model. The main question is, under which conditions an overdense cloud decouples from the cosmic expansion and collapses to a bound object. At the time of decoupling, the cloud has an overdensity of $\zeta \simeq 5.55$ with respect to the cosmological background density at the same time. At the point, when we expect the halo to be collapsed in our spherical collapse model, its linear density contrast might be

$$\delta_c \simeq 1.69. \tag{1.22}$$

This means that a halo can be considered to be collapsed when its density contrast expected from linear theory reaches a value of δ_c. Assuming the cloud to be in virial equilibrium, the resulting density contrast with respect to the background density is

$$\Delta = 32\zeta \simeq 178. \tag{1.23}$$

The spherical collapse model answers the question whether an overdensity collapses and what we actually mean by "collapsed".
Beyond this, it might be helpful to quantify the expected number of halos with a certain mass in a given cosmological volume. Press & Schechter (1974) addressed this question by deriving the halo mass function. Their original derivation was wrong by a factor of one half (they argued that it should be there due to normalization), which was fixed few years later by Bond et al. (1991). The comoving halo number density is then given by

$$N(M,z)\mathrm{d}M = \sqrt{\frac{2}{\pi}}\frac{\rho_0\delta_c}{\sigma_R}\frac{\mathrm{d}\ln\sigma_R}{\mathrm{d}M}\exp\left(-\frac{\delta_c^2}{2\sigma_R^2}\right)\frac{\mathrm{d}M}{M}, \tag{1.24}$$

where σ_R^2 is the smoothed density variance within a sphere of radius R. On small scales the mass function scales as

$$N(M,z)\mathrm{d}M \propto M^{-2}\mathrm{d}M, \tag{1.25}$$

which implies that there are many more low-mass objects than high-mass objects. These findings illustrate the hierarchical structure formation, because massive objects form over time by successively merging low-mass objects. This process is shown in Figure 1.6, where we can see the halo mass function for different redshifts. At high redshifts, the possibility of finding a high-mass object was significantly smaller and even at redshifts which are of interest for primordial star formation ($z = 20 - 30$), the distribution of halo masses is different than today.

1.3 Star Formation in the Early Universe

In the last section, we discussed the cosmological framework, which defines the initial conditions for star formation in the early Universe. In this section we want to derive characteristics of Pop III star formation, like the primordial IMF. So far,

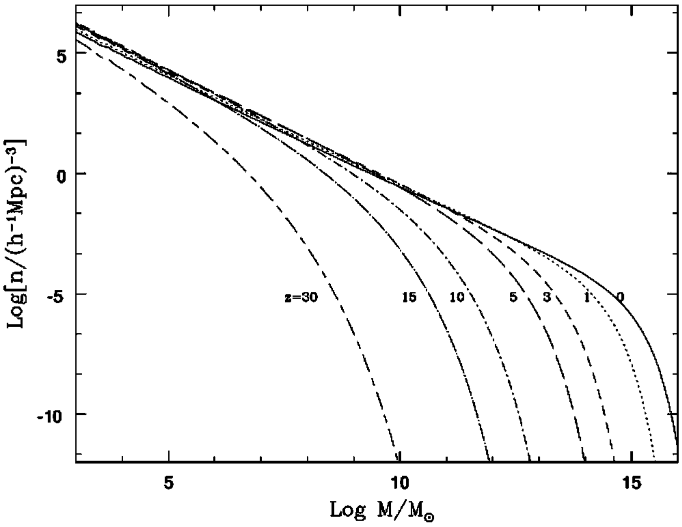

Figure 1.6: Evolution of the comoving number density of collapsed halos (Press-Schechter mass function). Note that the "cut-off" mass grows with time. Most of the mass fraction in collapsed halos at a given epoch is contained in halos with masses around the "cut-off" mass. Adopted by Avila-Reese (2006).

all the steps and processes in between are a black box to us, which we want to enlighten. Since star formation is a highly complex process with a lot of connections and dependencies between individual processes and quantities, we will illustrate this network at the end of each following subsections. Our current "understanding" of Pop III star formation is illustrated in Figure 1.7.

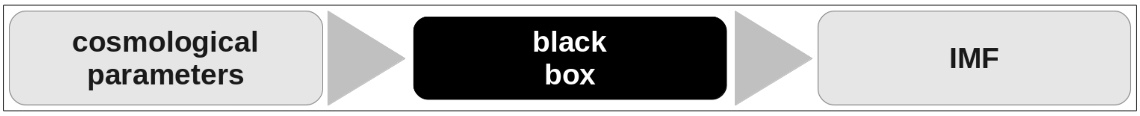

Figure 1.7: Diagram of primordial star formation. In the following illustrations, only the direct dependencies are displayed.

A consistent model of primordial star formation evolved over the last decades (the following brief historical overview is based on Greif et al. 2013). In the 1960's H_2 was considered to be an important coolant in low-metallicity gas, which might provide the necessary release of thermal energy for primordial gas clouds to collapse and create protostars (Saslaw & Zipoy 1967; Peebles & Dicke 1968; Hirasawa 1969; Matsuda et al. 1969; Takeda et al. 1969). Subsequent studies modelled Pop III star formation with the help of one-zone models, which were able to follow the dynamics with a simplified treatment of radiative cooling (Yoneyama 1972; Hutchins 1976; Silk 1977; Carlberg 1981; Palla et al. 1983; Silk 1983; Kashlinsky & Rees 1983; Carr et al. 1984; Couchman & Rees 1986; Uehara et al. 1996; Tegmark et al. 1997). With increasing computing capacity, three-dimensional simulations of primordial star formation were able to include more physical processes and follow the collapse with a higher spatial resolution (Abel et al. 1998; Bromm et al. 1999; Abel et al. 2000; Bromm et al. 2002; Abel et al. 2002). As already mentioned in section 1.1, Pop III star formation is fundamentally different from present-day star formation: the CMB temperature is higher, there are no metals which provide efficient cooling channels and there is no radiation field by nearby stars. According to Bromm (2013), the characteristics of the dark matter minihalo which hosts the star-forming cloud is one of the main ingredients of Pop III star formation. The Press-Schechter formalism yields an estimate of the number of dark matter halos as a function of redshift and the Jeans analysis determines whether these halos are gravitationally stable. Even if those halos are gravitationally unstable, the question still is, whether they can cool in a sufficiently short time (for a detailed discussion about cooling see section 1.3.2). The virial theorem contributes to this questions, by providing a rough estimate for the mass and temperature that a minihalo should at least have in order to provide efficient cooling:

$$M_{\mathrm{vir}} = 2 \times 10^7 h^{-1} \left(\frac{\mu}{0.6}\right)^{2/3} \Omega_m^{-1/2} \left(\frac{1+z}{20}\right)^{-3/2} M_\odot \tag{1.26}$$

$$T_{\mathrm{vir}} = 2 \times 10^3 \left(\frac{M}{10^6 M_\odot}\right)^{2/3} \left(\frac{1+z}{30}\right) \mathrm{K} \tag{1.27}$$

Since the virial mass is significantly above the estimated Jeans mass, we expect minihalos with masses around M_J and temperatures of roughly $T_{\mathrm{vir}} \simeq 500\mathrm{K}$ to be the first objects which provide the required conditions for star formation. A further analysis of the underlying physics yields masses for the minihalo of $10^5 - 10^6 M_\odot$ at virialisation redshifts around $z = 20 - 30$ (Bromm & Larson 2004; Glover 2005; Yoshida et al. 2006; O'Shea & Norman 2007; Greif et al. 2008; McKee & Tan 2008; Yoshida et al. 2008; Glover et al. 2008; Bromm et al. 2009; Turk et al. 2009; Peters et al. 2010; Turk et al. 2011; Clark et al. 2011a; Greif et al. 2012; Stacy et al. 2013; Hirano et al. 2013; Stacy & Bromm 2013; Greif et al. 2013; Bromm 2013). A helpful overview of these criteria is illustrated in Figure 1.8. Since this figure shows the time at which the central gas density reaches $\sim 10^6\,\mathrm{cm}^{-3}$ (which is quite high for minihalos), the peak of virialisation is shifted to smaller redshifts compared to the referred values above. However, we should keep in mind that not the total baryonic mass of the minihalo is transformed into stars. Rather a small fraction of the baryons within a virialised object can participate in Pop III star formation, which yields star formation rates of $0.1\% - 1\%$ (Abel et al. 2000; Klessen 2011; Stacy et al. 2013).

1.3.1 Primordial Chemistry

The second important ingredient in order to understand Pop III star formation is the chemical composition of the primordial gas cloud. Although the number of involved species is much lower than in the present-day Universe, the chemical network is still complex. We only present the most important reactions, whereas

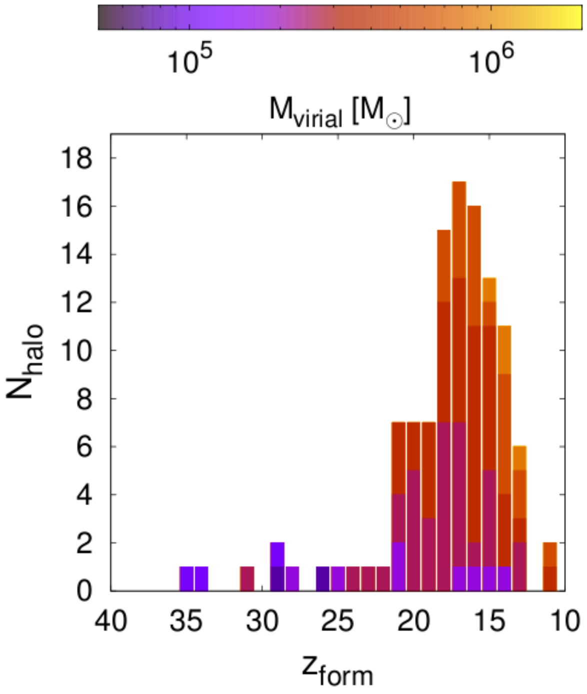

Figure 1.8: The number of dark matter minihalos that host star-forming gas clouds as a function of redshift. The histogram shows the distribution of redshifts when the central gas density reaches $\sim 10^6\,\mathrm{cm}^{-3}$. Adopted by Hirano et al. (2013).

Glover & Savin (2009) model this primordial network containing 30 species and 392 reactions. A detailed list of all important chemical reactions and the corresponding rate coefficients can be found in Yoshida et al. (2006).

Formation Channels and Rates

The most essential molecule in primordial star formation is molecular hydrogen. Therefore, we want to focus on its different formation and destruction channels. The chemistry of H_2 in primordial gas has been reviewed in several studies (Abel et al. 1997; Galli & Palla 1998; Stancil et al. 1998; Glover & Abel 2008), while the following overview is mainly based on Clark & Glover (2013) and Glover (2013). Due to the non-existing dipole moment, H_2 cannot form directly via the radiative association reaction

$$\mathrm{H} + \mathrm{H} \rightarrow \mathrm{H}_2 + \gamma. \tag{1.28}$$

Whereas in the local Universe most H_2 forms via surface reactions on dust grains, this mechanism is not possible in primordial gas. Hence, most H_2 in the early Universe is created via the pathway

$$\mathrm{H} + \mathrm{e} \rightarrow \mathrm{H}^- + \gamma \tag{1.29}$$
$$\mathrm{H}^- + \mathrm{H} \rightarrow \mathrm{H}_2 + \mathrm{e}^- \tag{1.30}$$

and about 10% via the pathway

$$\mathrm{H} + \mathrm{H}^+ \rightarrow \mathrm{H}_2^+ + \gamma \tag{1.31}$$
$$\mathrm{H}_2^+ + \mathrm{H} \rightarrow \mathrm{H}_2 + \mathrm{H}^+. \tag{1.32}$$

The rate limiting step of these reactions is the rate at which H^- ions form (Turk et al. 2011). However, since the creation and destruction rates of H^- are uncertain by up to an order of magnitude, this also leads to an uncertainty in the creation rate of H_2. Additionally, H_2 can form via the 3-body processes

$$\mathrm{H} + \mathrm{H} + \mathrm{H} \rightarrow \mathrm{H}_2 + \mathrm{H}, \tag{1.33}$$
$$\mathrm{H} + \mathrm{H} + \mathrm{H}_2 \rightarrow \mathrm{H}_2 + \mathrm{H}_2, \tag{1.34}$$
$$\mathrm{H} + \mathrm{H} + \mathrm{He} \rightarrow \mathrm{H}_2 + \mathrm{He}. \tag{1.35}$$

Since the possibility of these reactions scale with n^3, formation via the 3-body processes becomes only important at densities above $n \gtrsim 10^8\,\mathrm{cm}^{-3}$ (Omukai et al. 2005; Glover et al. 2008; Stacy et al. 2013). The onset of 3-body H_2 formation marks an important point in Pop III star formation, because subsequently most hydrogen is transformed into H_2 and the gas is almost fully molecular at a density of around $n \simeq 10^{12}\,\mathrm{cm}^{-3}$. However, the rate coefficient for this reaction is uncertain by nearly an order of magnitude and the choice of its value might influence accretion, long-term stability of the disc, and fragmentation (Turk et al. 2011; Clark et al. 2011b). In order to destroy H_2, its binding energy of 4.48eV has to be overcome, which is far above the mean kinetic energy of the CMB photons at the corresponding redshift. Also the collisional dissociation

$$\mathrm{H}_2 + \mathrm{H} \rightarrow \mathrm{H} + \mathrm{H} + \mathrm{H}, \tag{1.36}$$
$$\mathrm{H}_2 + \mathrm{H}_2 \rightarrow \mathrm{H} + \mathrm{H} + \mathrm{H}_2 \tag{1.37}$$

or charge transfer with H^+

$$\mathrm{H}_2 + \mathrm{H}^+ \rightarrow \mathrm{H}_2^+ + \mathrm{H} \tag{1.38}$$

are ineffective at low temperatures. Hence, the primordial gas remains molecular, until a strong, ionising radiation field (e.g. by massive stars or black holes) dissociates most H_2.

It is mainly dissociated by photons with energies in the range 11.15 to 13.6eV (so called Lyman-Werner photons), since these photons are not strongly absorbed by neutral hydrogen. Although this process might not be relevant for the initial

H_2 abundance in the first minihalos, photodissociation via the so-called Solomon process (Solomon 1965; Stecher & Williams 1967; Abel et al. 1997; Wolcott-Green et al. 2011; Latif et al. 2013a)

$$H_2 + \gamma \rightarrow H_2^* \rightarrow H + H \qquad (1.39)$$

is very important for the accretion and evolution of primordial protostars. However, since Lyman-Werner lines have a spectral width of $\Delta\nu/\nu \simeq 10^{-5}$, only 15% of the absorptions are followed by photodissociation of H_2 .

Primordial Abundances

According to Equation 1.9, the mass ratio of helium to hydrogen is about 1/4, which yields a fractional helium abundance of 8.3%. The abundance of molecular hydrogen in the post-recombination Universe is between $10^{-4} \lesssim x_{H_2} \lesssim 10^{-3}$ (Omukai et al. 2005; Yoshida et al. 2008; Turk et al. 2011; Clark et al. 2011a; Clark & Glover 2013; Bromm 2013). Following Clark et al. (2011a) and Greif et al. (2008), further primordial abundances are roughly $x_{H^+} \simeq 10^{-7}$, $x_{HD} \simeq 3\times10^{-7}$ and $x_{D^+} \simeq 3\times10^{-12}$. These and other abundances are illustrated in Figure 1.3 as a function of time. Hence, the mean molecular weight of primordial gas is roughly $\mu \simeq 1.33$.

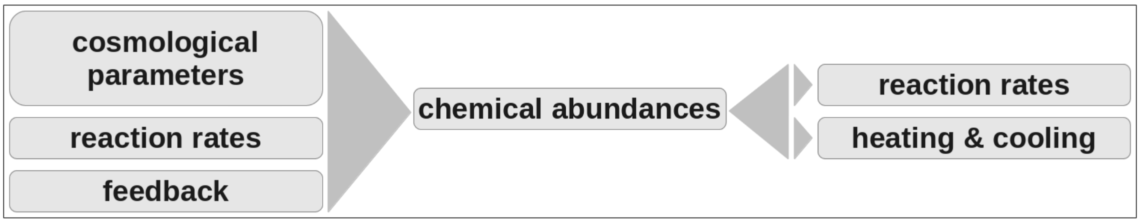

1.3.2 Heating and Cooling

By the terms “heating” and “cooling” we generally describe all processes that might inject or release thermal energy from the cloud. During the gravitational collapse, the gas temperature rises due to compressive heating. Consequently, in the absence of any cooling process, the gas might not be able to contract to stellar densities. Generally, cooling is based on the creation of photons that might escape the cloud and therefore transport thermal energy outwards. Until the cloud becomes optically thick at densities of $n \simeq 10^{16}\,\mathrm{cm}^{-3}$ (Glover et al. 2008; Clark et al. 2011a), molecular hydrogen is the most important coolant (Saslaw & Zipoy 1967; Haiman et al. 1996;

Anninos et al. 1997; Abel et al. 2000; Glover & Brand 2003; Glover 2005; Glover & Jappsen 2007; Glover et al. 2008; Clark et al. 2011b; Hirano et al. 2013). In this section we focus on the most relevant heating and cooling mechanisms that might be relevant for the further understanding of this thesis. A list of all heating and cooling processes in primordial gas can be found e.g. in Glover & Brand (2003).

H_2 Line Cooling

H_2 line cooling is relevant in the density regime $10^8\,\mathrm{cm}^{-3} \lesssim n \lesssim 10^{14}\,\mathrm{cm}^{-3}$ and is based on the rovibrational transitions of molecular hydrogen. A detailed discussion of this cooling process is given in section 1.4.

CIE Cooling

A single, isolated H_2 molecule has no dipole moment. However, when two H_2 molecules collide, they briefly induce a charge displacement, which leads to a non-zero dipole moment for a very short period of time. During this collision, they can absorb or emit radiation through dipole transitions, which have much higher transition probabilities. A detailed discussion of this process can be found in Frommhold (1993). Generally this process can occur at any given density, but since the possibility that two H_2 molecules collide depends on the H_2 abundance and increases quadratically with density, CIE cooling becomes merely important at densities of around $n \simeq 10^{14}\,\mathrm{cm}^{-3}$ (Ripamonti & Abel 2004; Omukai et al. 2005; Glover et al. 2008; Clark et al. 2011a; Hirano & Yoshida 2013; Glover 2013). Due to the short lifetime of the collision state, the lines are very broad and almost merge into a continuum. Hence, the high opacity in the rovibrational lines does hardly reduce the amount of energy that can be radiated away by CIE. Only when the gas density reaches a value of $n \gtrsim 10^{16}\,\mathrm{cm}^{-3}$, opacity effects become important. A corresponding correction was firstly introduced by Ripamonti & Abel (2004) and several of these correction methods are compared in Hirano & Yoshida (2013). Summing up, CIE cooling provides an efficient cooling channel, even if the opacity at high densities reduces the H_2 line cooling rate.

HD Cooling

Generally, the gas can cool by HD line emissions to a temperature of $T \simeq 100$K. However, the cooling rate is very small and hardly affects the overall evolution of the cloud for metallicities below $Z \leq -6$. This cooling process is only effective for low densities and higher electron abundances than we find in Pop III star formation (Omukai et al. 2005; Glover et al. 2008; Greif et al. 2012; Hirano & Yoshida 2013). According to Glover et al. (2008), the next relevant coolant might be H_3^+, which contributes to the overall cooling rate at the level of a few percent.

H_2 Formation Heating and Dissociation Cooling

As we have seen in section 1.3.1, molecular hydrogen is created and might be destroyed during the formation of Pop III stars. Since each H_2 molecule has a binding energy of 4.48eV, these processes also affect the thermal evolution of the cloud. Each time, an H_2 molecule is formed, the release of binding energy heats the gas. Due to the fact that the formation of H_2 goes along with a dramatic increase in the H_2 cooling rate, this energy input of the formation heating is generally overcompensated. On the other hand, H_2 dissociation cooling is a very crucial process. At densities above $n \gtrsim 10^{16}\,\mathrm{cm}^{-3}$ there are no effective radiative cooling channels. However, the dissociation of H_2 provides the necessary cooling for the core to collapse to protostellar densities of around $n \simeq 10^{20}\,\mathrm{cm}^{-3}$ (Ripamonti et al. 2002; Glover et al. 2008; Clark et al. 2011a; Glover 2013).

Overview

A compilation of the main heating and cooling mechanisms in primordial gas as a function of density is shown in Figure 1.9. This figure illustrates that compressional heating is the dominant heating mechanism and H_2 line and CIE cooling are the most relevant cooling channels. Nevertheless, one should keep in mind that the individual cooling rates are rather uncertain and the temperature evolution of the

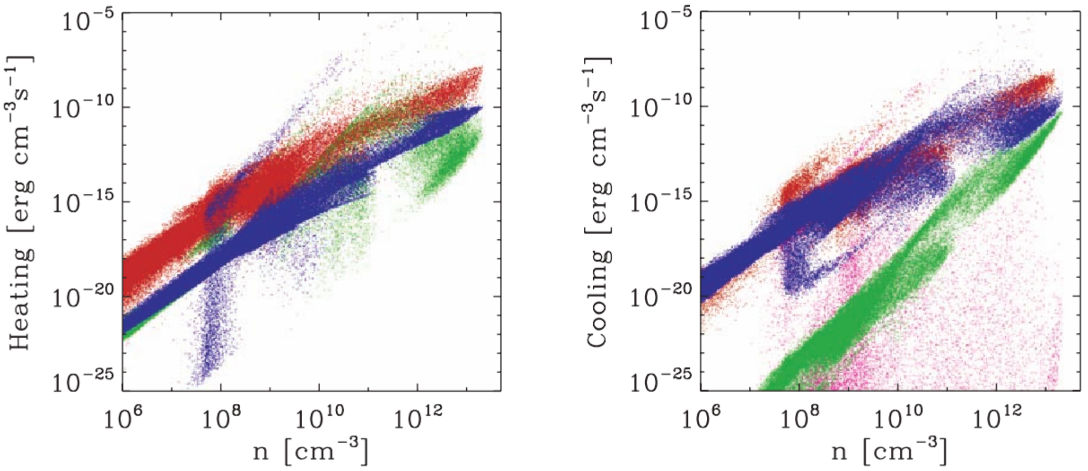

Figure 1.9: Left: gas heating rates in a typical primordial cloud. Red shows compressive heating, green shows heating due to H_2 formation and blue shows the heating due to accretion. The heating rate from accretion is of the same order as that from H_2 formation and about 2 orders of magnitude lower than that from compression during the collapse. Right: the gas cooling rates in a typical primordial cloud. Blue shows H_2 line cooling, green shows CIE cooling, red shows cooling from re-expansion of previously compressed gas and pink shows the cooling due to H_2 dissociation. Adopted from Smith et al. (2011).

gas in the density regime $10^8 \leq n \leq 10^{13}$ is unclear by about 50% (Glover et al. 2008).

Cooling Time

An important concept which is related to the previously presented cooling rates is the cooling time. If Λ denotes the net cooling rate, the cooling time is given by

$$t_{\mathrm{cool}} = \frac{1}{\gamma - 1} \frac{n k_B T}{\Lambda}, \tag{1.40}$$

where γ is the adiabatic index, n is the total number density of particles, and T is the gas temperature. Thus, this timescale is a first order approximation for the time, the cloud might need to loose its total thermal energy. If the cooling time is shorter than the dynamical time of the cloud, cooling is efficient enough and the cloud undergoes runaway collapse. According to Glover (2013) this criterion is related to a critical minihalo mass

$$M_{\mathrm{crit}} \simeq 6 \times 10^5 h^{-1} \left(\frac{\mu}{1.2}\right)^{-3/2} \Omega_m^{-1/2} \left(\frac{1+z}{10}\right)^{-3/2} M_{\odot}. \tag{1.41}$$

This mass corresponds to the minimum mass which a halo should have in order to provide efficient cooling and is illustrated in Figure 1.5.

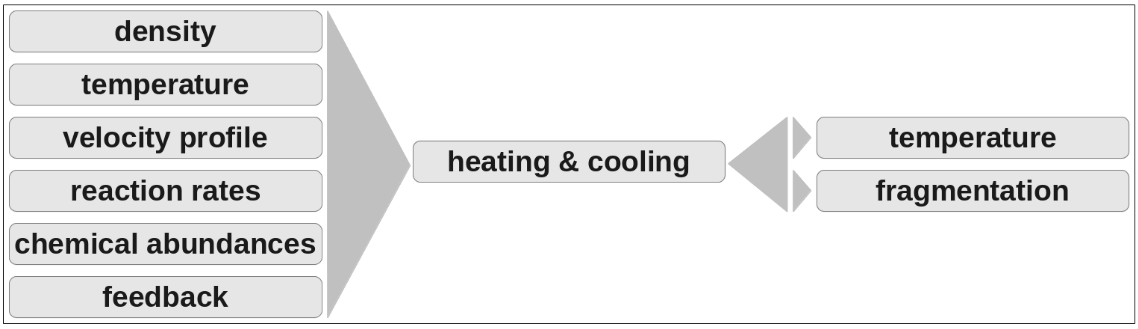

1.3.3 Collapse of a Primordial Cloud

A characteristic timescale for the collapse of a gas cloud is the free-fall time

$$t_{ff} = \sqrt{\frac{3\pi}{32 G \rho}}, \tag{1.42}$$

where ρ is the mean density (Klessen 2011). A homogeneous, pressureless gas cloud, which is initially at rest might collapse within this time. Although these criteria are not fulfilled, the free-fall time yields nevertheless a useful characteristic timescale for the collapse of a cloud.

The gas does not simply undergo hierarchical fragmentation, but rather evolves in a highly complex and non-linear fashion. Hence, we have to study the different phases and the corresponding physical processes. A state of hydrodynamic and thermodynamic equilibrium is reached at a density of $n \simeq 10^4\,\mathrm{cm}^{-3}$ and a temperature of $T \simeq 200\mathrm{K}$ (Glover et al. 2008; Clark et al. 2011a). Following Bromm (2013), the subsequent collapse can be divided into three phases:

1. Atomic phase: for densities $n \leq 10^8\,\mathrm{cm}^{-3}$ the gas is mostly atomic, except a tiny amount of molecular hydrogen.

2. Molecular phase: 3-body H_2 formation sets in and provides an efficient cooling channel until the lines of molecular hydrogen become optically thick at around $n \simeq 10^{14}\,\mathrm{cm}^{-3}$.

3. Approaching protostellar conditions: CIE and H_2 dissociation cooling can provide a release of thermal energy up to densities of $n \simeq 10^{17}\,\mathrm{cm}^{-3}$. Above this value, pressure and temperature decrease steeply and a protostar is formed.

Although the density decreases by ten orders of magnitude within the first two phases, the temperature remains almost constant. This is why the collapse of a primordial gas cloud is generally considered to be isothermal with an effective adiabatic index of $\gamma \simeq 1.1$ (Glover et al. 2008; Hirano et al. 2013; Stacy & Bromm 2013; Glover 2013). Only once the H_2 content of the collapsing gas is exhausted, the collapse becomes adiabatic at densities of around $n \simeq 10^{20}\,\mathrm{cm}^{-3}$ (Clark et al. 2011b; Glover et al. 2008).

Larson (1969) and Penston (1969) derived a set of self-similar solutions for the collapse of gas clouds. Accordingly, the first two phases of the collapse of a primordial cloud can be described by the radial density slope

$$n \propto r^{-2.2} \tag{1.43}$$

(Ripamonti et al. 2002; Machida & Doi 2013; Glover 2013; Bromm 2013). This typical radial density slope is observed in many other simulations of primordial star formation (Clark et al. 2008, 2011b; Greif et al. 2012; Clark & Glover 2013; Greif et al. 2013; Hirano et al. 2013). Another important ingredient of star formation is turbulence (Klessen 2011). Primordial star formation is mainly dominated by transonic turbulence (Clark et al. 2008; Greif et al. 2013; Stacy et al. 2013; Bromm 2013) and the assembly of the first galaxies marks the onset of supersonic turbulence (Bromm 2013),

1.3.4 Fragmentation

Under certain conditions, the cloud does not simply collapse and form one central star, but rather fragment into several clumps. The possibility of fragmentation in primordial clouds is considered by Sabano & Yoshii (1977); Clark et al. (2008); Turk et al. (2009); Clark et al. (2011a); Greif et al. (2011); Clark et al. (2011b); Greif et al. (2012); Machida & Doi (2013); Glover (2013); Bromm (2013). Generally, one can distinguish between two different types of fragmentation. In the case of the "chemo-thermal" instability a sudden increase in the net cooling rate enables local contraction, while the disc fragmentation relies on instabilities of the accretion disc. Fragmentation is a very chaotic, non-deterministic process and the actual outcome depends sensitively on the initial conditions. Turk et al. (2009) and Greif et al. (2013) simulate different primordial clouds and find them to fragment in one out of five and in two out of nine realisations, respectively. This shows that one can not definitively predict the outcome of fragmentation. Nevertheless, there are three analytical expressions in order to quantify the possibility of a gas cloud to fragment:

- In order to locally contract instead of globally collapse, a necessary criterion for fragmentation is (Turk et al. 2009)

  $$\frac{t_{\rm cool}}{t_{ff}} < 1. \tag{1.44}$$

- Toomre (1964) analyses the stability of rotating gas discs and derives the instability criteria

  $$Q = \frac{c_s \kappa}{\pi G \Sigma} < 1, \tag{1.45}$$

  where κ is the epicyclic frequency and Σ is the surface density of the disc. For Keplerian discs one can replace κ by the orbital frequency ω. Formally, this criterion is only valid for thin discs and Goldreich & Lynden-Bell (1965) extended the criterion by requiring $Q < 0.676$ for a finite-thickness isothermal disc to fragment.

- Gammie (2001) investigates the nonlinear outcome of a stability analysis of a Keplerian accretion disc. Based on numerical experiments he derives the instability criterion

  $$\frac{3t_{\rm cool}}{\omega} < 1, \tag{1.46}$$

  where ω is the orbital frequency. The Gammie criterion expresses the possibility that pieces of the disc cool and collapse before they have the opportunity to collide with one another in order to reheat the disc.

In their study on the formation and evolution of primordial protostellar systems, Greif et al. (2012) find the Toomre criterion insufficient for the quantification of gravitational instability and additionally use the Gammie criterion. Non of these criteria guarantees fragmentation (Yoshida et al. 2006), but a combination of them might yield a reliable quantification of instabilities in the gas cloud.
A lot of recent studies detect the formation of a rotationally supported disc around

Pop III protostars, which might become gravitationally unstable and leads to fragmentation (Clark et al. 2011b; Hosokawa et al. 2011; Greif et al. 2012, 2013; Glover 2013; Latif et al. 2013a). This disc extends out to 400 – 1000AU and has a characteristic temperature of 1500 – 2000K (Clark et al. 2011b; Hosokawa et al. 2011; Glover 2013). While the chemo-thermal instability occurs in company with the onset of 3-body H_2 formation, disc fragmentation generally occurs at higher densities ($10^{13} - 10^{14}\,\mathrm{cm}^{-3}$) very close ($r = 1 - 20$AU) to the centre of the cloud (Ripamonti & Abel 2004; Omukai et al. 2005; Clark et al. 2011a,b; Greif et al. 2012; Machida & Doi 2013). Fragmentation in the central part of the cloud is stopped, when the last cooling mechanism is eliminated by the dissociation of H_2 and the thermal evolution becomes adiabatic.

Another important ingredient for fragmentation (and a topic on its own) is the presence of turbulence, which might provide support on global scales, but triggers fragmentation on small scales. A detailed discussion on the role of turbulence in (primordial) star formation can be found in Klessen (2011); Clark et al. (2011a) and references therein.

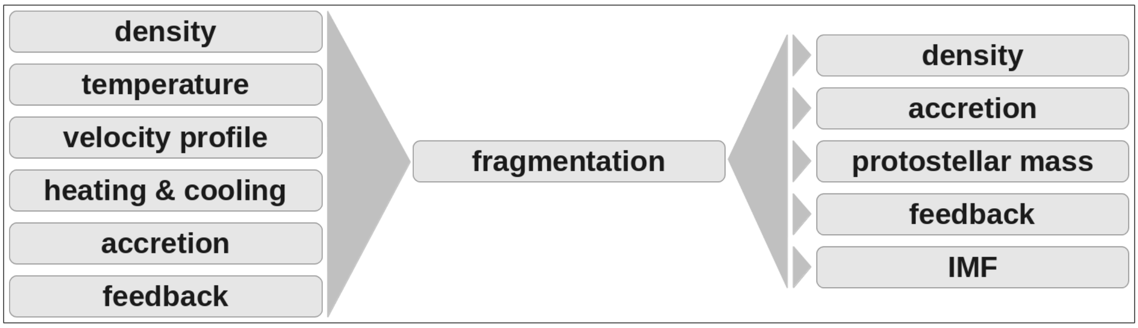

1.3.5 Evolution of Protostars

In order to determine the mass accretion rate, feedback and other processes that might influence the protostellar environment, we have to understand the basic principles of primordial protostellar evolution. Except for some quantitative disagreements (see e.g. Turk et al. 2011), there is broad agreement on the qualitative evolution of a Pop III protostar. Although this evolution is a complex interplay of many processes, it can be summarised by a few characteristic steps. Since we are only interested in the effects which might affect the protostellar environment, we present a brief summary and reference to other studies for the details of protostellar evolution, e.g. Stahler et al. (1986); Omukai & Palla (2001).

1. At densities above $n \gtrsim 10^{19}\,\mathrm{cm}^{-3}$ most of the molecular hydrogen is dissociated, the adiabatic index rises from $\gamma \simeq 1.1$ to $\gamma \simeq 5/3$ and the self-similar solution breaks down (Omukai & Palla 2001; Haardt et al. 2002; Omukai et al. 2005; Yoshida et al. 2006; McKee & Tan 2008; Greif et al. 2012).

2. A quasi-hydrostatic core with a mass of $M_* \simeq 0.01 M_\odot$ forms and a shock front develops at the protostellar surface (Omukai & Nishi 1998; Haardt et al. 2002; Greif et al. 2012; Hirano et al. 2013).

3. In the early phase, luminosity and thermal energy are mostly produced by contraction (Omukai & Palla 2001; Krumholz & McKee 2008). Consequently, temperature rises slowly and at a mass of around $M_* \simeq 5 M_\odot$ the outer layers expand (due to the negative heat capacity of stars).

4. At masses around $M_* \simeq 35 M_\odot$ the pp-chain becomes efficient (Hosokawa et al. 2011).

5. Hydrogen fusion halts the contraction at higher masses and the star reaches the zero age main sequence (ZAMS) after approximately 10^6yr of protostellar evolution (Yoshida et al. 2006; Glover 2013).

The evolution of the protostar in the Hertzsprung-Russle diagram is illustrated in Figure 1.10.

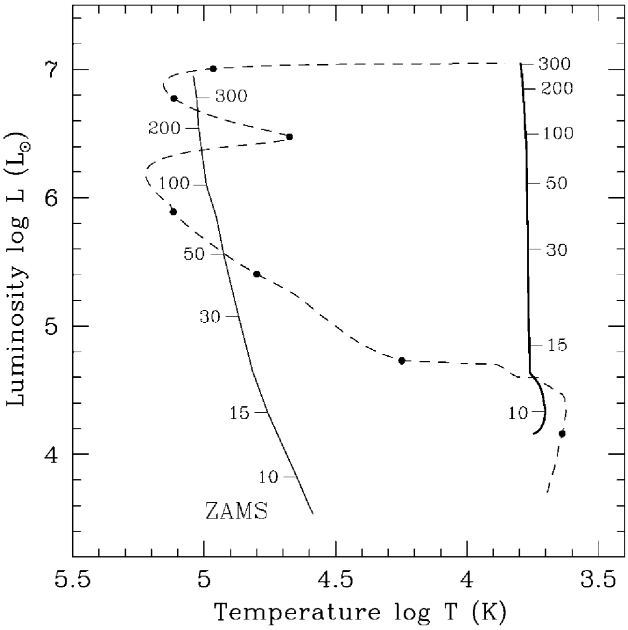

Figure 1.10: H-R diagram for primordial protostars. The evolution of the photosphere and core surface is shown by the thick solid line and the dashed line, respectively. For comparison, we also show the locus of the metal-free ZAMS stars. The numbers on both tracks label the value of the core mass (in solar units). The filled circles on the dashed line have the same meaning. Adopted from Omukai & Palla (2001).

Regarding the protostellar evolution, there are some special characteristics for the primordial case, compared to the present-day one. These characteristics of primordial protostellar evolution are summarised in the following list:

- Deuterium burning does not play an important role (Omukai & Palla 2001; Schleicher et al. 2013; Glover 2013).
- High-mass stars reach the main sequence while they are still accreting (Peters et al. 2010; Klessen 2011).
- Massive star formation can not be spherically symmetric (Klessen 2011).
- While Pop III protostars are large, fluffy objects, the final stars are smaller than their present day counterparts (Smith et al. 2011; Clark & Glover 2013).

The previously discussed evolution of primordial protostars goes along with an interdependent network of other important processes that are discussed in the following subsections.

Accretion

Accretion is a crucial process in the determination of the final masses of Pop III stars. Hirano et al. (2013) even claims a direct analytic relation, correlating the accretion rate and the final stellar mass. Due to the chemical composition of the primordial gas and the comparatively high temperature, accretion in the early Universe differs significantly from accretion in present-day star formation. Since there are no dust grains, radiative pressure is less efficient and the accretion rates are consequently higher. A first estimate for the accretion rate can be derived from the assumption that a Jeans mass is accreted in about one free-fall time:

$$\dot{M} = \frac{M_J}{t_{ff}} \propto c_s^3 \propto T^{3/2} \tag{1.47}$$

The temperature of the star-forming gas in a primordial minihalo is of the order of $T \simeq 1000$K, far larger than the 10K temperatures of present-day star forming clouds (Omukai & Palla 2001; Bergin & Tafalla 2007; Glover 2013). Consequently, the primordial accretion rates are much higher than local accretion rates, which are of the order of $\dot{M} \simeq 10^{-5} M_\odot \mathrm{yr}^{-1}$ (Glover et al. 2008). Typical values for the accretion rate in primordial star formation range from $\dot{M} \simeq 10^{-3} M_\odot \mathrm{yr}^{-1}$ to $\dot{M} \simeq 10^{-1} M_\odot \mathrm{yr}^{-1}$ (Ripamonti et al. 2002; Hosokawa et al. 2011; Clark et al. 2011b; Hirano et al. 2013). However, these accretion rates are highly variable in time (Klessen 2011; Smith et al. 2011; Hirano et al. 2013; Stacy et al. 2013; Glover 2013). Depending on the physical conditions and the structure of the disc, there are several analytical expressions for the accretion rate at different phases of the collapse which can be seen in Figure 1.11. This figure also illustrates the previously mentioned high and strongly variable accretion rates. A main question is, when accretion is stopped and by what processes. In order to answer this question, we can distinguish two cases:

- In the case of a “smooth accretion” model, major parts of the infalling envelope might be accreted by the central object. Since protostellar radiation can not

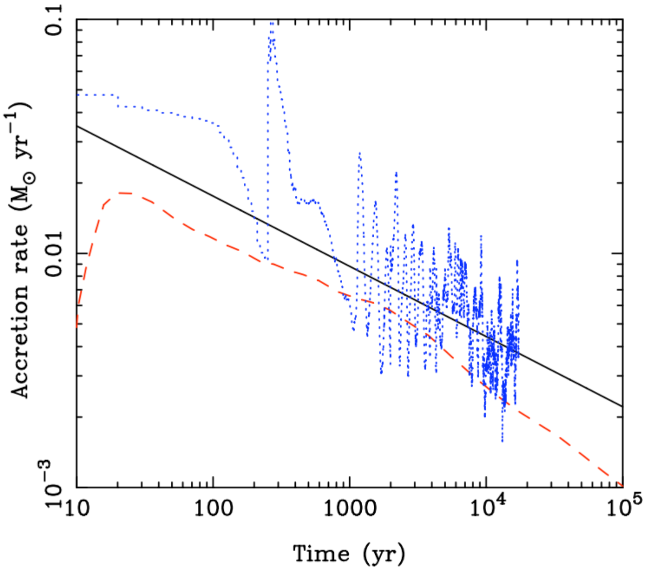

Figure 1.11: Three different estimates for the accretion rate onto a Pop III protostar, taken from Tan & McKee (2004) (solid line), Turk et al. (2011) (dashed line) and Smith et al. (2011) (dotted line). Adopted from Glover (2013).

halt this inflow, the mass accretion rate decreases rather slowly with increasing stellar mass (Machida & Doi 2013; Hirano et al. 2013).

- While in the case of "competitive accretion", the gas is accreted by several protostars. Consequently, each individual protostar has to compete for gas and the reservoir might get exhausted. This scenario (also called "fragmentation induced starvation") is discussed e.g. by Peters et al. (2010).

In reality, there is no clear distinction between these two scenarios and the accretion rate might remain high, although there are several protostars competing for infalling gas. Ultimately, accretion stops for protostellar masses between $43M_\odot$ (Clark & Glover 2013) and $100M_\odot$ (Turk et al. 2009).

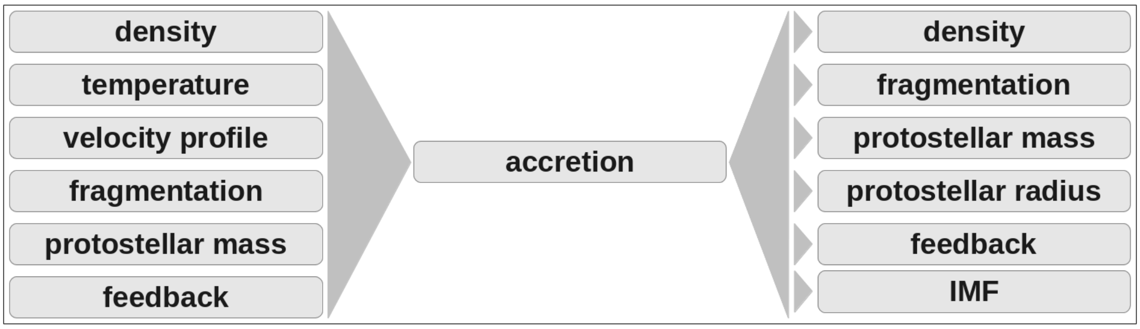

Protostellar Mass

As already seen in Figure 1.1, the uncertainties in the expected mass range are very large. Since the accretion rate is very high and primordial gas contains almost no metals, Pop III stars can become very massive (Omukai & Palla 2001; Clark et al. 2008). Though, the most interesting question is: how massive? Assuming a constant accretion rate of $\dot{M} \simeq 10^{-3} M_{\odot}\mathrm{yr}^{-1}$ over the typical Kelvin-Helmholtz timescale $t_{KH} \simeq 10^5$yr yields a rough upper limit of $100 M_{\odot}$. Even if we consider continuing accretion during the main sequence lifetime, this might merely increase the upper mass limit by the factor of a few to $\sim 600 M_{\odot}$. However in reality, protostellar feedback and competitive accretion limit the stellar masses to much smaller values. Reliable upper mass limits for Pop III stars are in the range $20 M_{\odot}$ to $140 M_{\odot}$ (Clark et al. 2008; Bromm 2013).

Protostellar Radius

The protostellar radius mainly depends on the interplay between accretion, feedback and energy production. Based on the semi-analytic model by Smith et al. (2011) the protostellar radius can be described by the broken power-law

$$R \propto \begin{cases} 26 M^{0.27} (\dot{M}/10^{-3})^{0.41} & \text{for} \quad M \leq 5 M_{\odot} \\ A_1 M^3 & \text{for} \quad 5 M_{\odot} < M \leq 7 M_{\odot} \\ A_2 M^{-2} & \text{for} \quad 7 M_{\odot} < M \quad \text{and} \quad R < R_{ms} \end{cases} \tag{1.48}$$

where A_1 and A_2 are numerical constants and R_{ms} is the main-sequence radius

$$R_{ms} = 0.28 M^{0.61} R_{\odot} \tag{1.49}$$

according to Omukai & Palla (2003). This power law is suitable for a mass accretion rate of $\dot{M} \simeq 10^{-3} M_{\odot}\mathrm{yr}^{-1}$, while for other accretion rates, the transition values between the individual slopes have to be adopted. The protostellar radius as a function of mass can be seen for different accretion rates in Figure 1.12. The radius increases, reaches a sharp peak at a protostellar mass of $10 M_{\odot}$ with a maximum value of roughly $100 R_{\odot}$ and then decreases to its main-sequence value. In any case, the protostellar radius is smaller than 1AU, which is relevant for fragmentation and possible merger events.

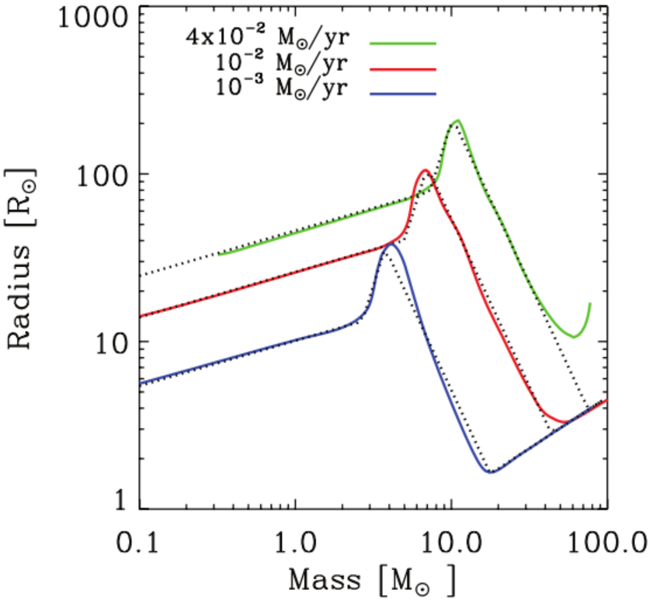

Figure 1.12: The protostellar radius as a function of mass found in the stellar evolution models of Omukai & Palla (2003) for three different accretion rates. The dotted black lines show the stellar radius given by Equation 1.48 for these accretion rates. Adopted from Smith et al. (2011).

Feedback

Generally, radiative feedback from the accreting protostar has several effects on its environment:

- The radiative pressure counteracts the gravitational force and therefore reduces accretion.
- The radiation might heat the gas and therefore stabilise it against fragmentation.
- Some photons might be energetic enough to photodissociate the H_2 .

The question, whether these processes actually occur and can significantly influence primordial star formation is not finally solved. Although the number of ionising photons is small in the early protostellar phase, their number steeply rises with mass, as it can be seen in Figure 1.13. Above a protostellar mass of $10 - 15 M_\odot$, a star can effectively photodissociate the molecular hydrogen (Glover 2000; Glover & Brand 2003; Smith et al. 2011; Klessen 2011; Hirano et al. 2013). Although accretion feedback heats the gas and even removes the dominant coolant, it is not believed to

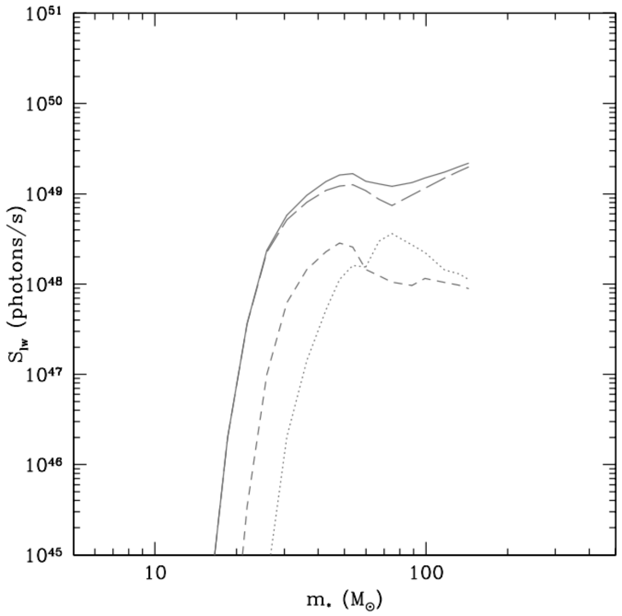

Figure 1.13: Evolution of Lyman-Werner photon luminosity for a typical primordial protostar, including effects of stellar feedback. The total (solid line) and contributions from the protostellar surface (long-dashed line), boundary layer (short-dashed line), and accretion disc from $r < 10R_\odot$ (dotted line) are shown. Adopted from McKee & Tan (2008).

suppress fragmentation on large scales (Krumholz & McKee 2008; Peters et al. 2010; Clark et al. 2011b,a; Greif et al. 2011; Glover 2013). However, Smith et al. (2011) and Machida & Doi (2013) find fragmentation to be suppressed in the inner ~ 20AU due to accretion luminosity heating. Even if fragmentation can not be suppressed by accretion feedback, it is delayed up to ~ 1000yr. Regarding the radiative pressure one can say that this effect is rather ineffective at early protostellar stages, but becomes important for protostellar masses above $\sim 50M_\odot$ and can even halt further gas accretion (Omukai & Palla 2001; Haardt et al. 2002; Hosokawa et al. 2011, 2012; Hirano et al. 2013).

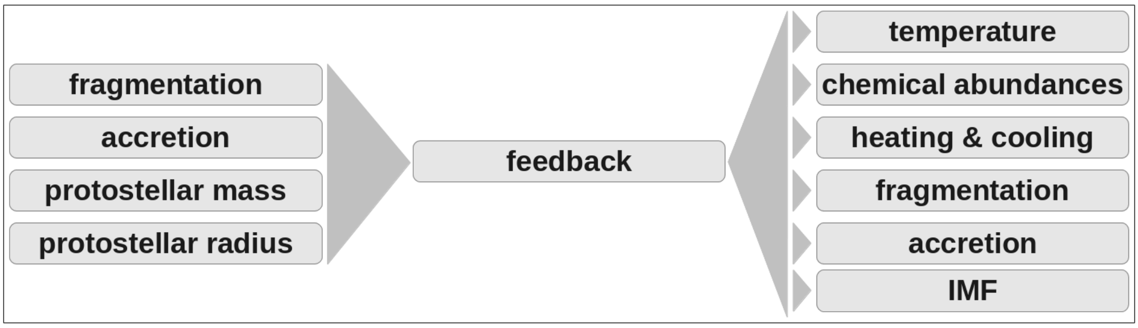

IMF

Since primordial gas contains no metals, almost all stellar properties depend on the initial mass of the star. Therefore, the primordial IMF is the key in determining the characteristics of Pop III stars and their effects on the environment. The IMF is generally expected to be top-heavy and flatter than the present-day IMF (Glover et al. 2008; Clark et al. 2008; Greif et al. 2011; Smith et al. 2011; Stacy et al. 2013; Bromm 2013). However, the exact shape of the IMF and even the mass range of Pop III stars is only poorly understood, which is for example illustrated in Figure 1.1. The best approximation of a primordial IMF with most statistical evidence is recently given by Hirano et al. (2013), who determine the evolution of 100 Pop III protostars. Their IMF can be seen in Figure 1.14. The main characteristics of primordial star formation are present in their plot. The characteristic mass is significantly above one solar mass and there is no single peak, but the distribution appears to be flat.

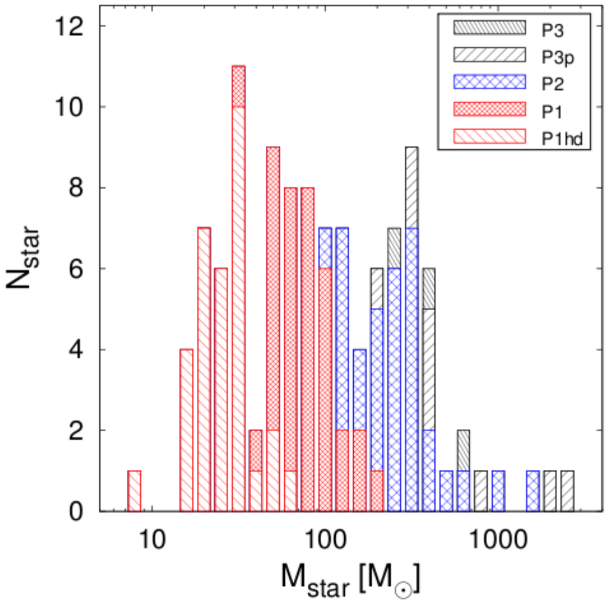

Figure 1.14: The final distribution of the calculated stellar masses for 110 first stars. The red, blue, and black histograms represent different paths of protostellar evolution (see original paper for details). Adopted from Hirano et al. (2013).

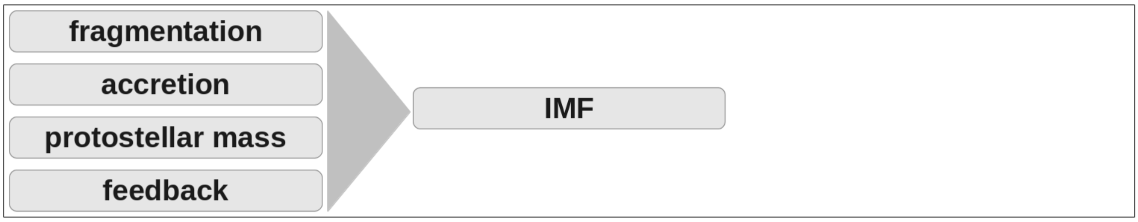

Final Stages

The final fate of a Pop III star does mainly depend on its mass and slightly on its rotation. Since these processes are only of minor relevance for the understanding of the thesis, they are only briefly summarised in Table 1.1, in order to complete the concept of primordial star formation. Since rotation supports mixing of the elements inside the star and therefore leads to a more homogeneous evolution, the minimum mass for a rotating Pop III star to end in a PISN is decreased to $\sim 65M_\odot$ (Stacy & Bromm 2013). However, the fact that the characteristic odd-even abundance patterns of PISN are not observed in early star forming regions, might reveal a further restriction to the actual mass range of Pop III stars.

Mass Range	Final Fate
$10M_\odot \leq M < 40M_\odot$	Type II Supernova
$40M_\odot \leq M < 100M_\odot$	Black Hole
$100M_\odot \leq M < 250M_\odot$	Pair Instability Supernova (PISN)
$M \geq 250M_\odot$	Black Hole

Table 1.1: Final stages of non-rotating Pop III stars as a function of their initial mass. The indicated values are mean values from Glover et al. (2008) and Stacy & Bromm (2013).

1.3.6 Open Questions

Although the previously presented scenario of primordial star formation seems to be consistent, there are a lot of uncertainties and open questions. In this section we give an overview of unsolved problems and their possible effects. A more detailed discussion on these open questions in the study of Pop III star formation can be found in Glover et al. (2008).

- Dark matter annihilation can generate luminosities up to $140L_\odot$ and might therefore influence heating, prevent fragmentation by stabilising the disc, or even hold the collapse (Glover 2013; Bromm 2013).

- Although the generation and strength of magnetic fields in primordial gas clouds is only poorly understood, they seem to stabilise the cloud and hence suppress fragmentation (Machida & Doi 2013; Bromm 2013).

- Until now, no Pop III star has ever been observed and we do not even know, how many Pop III remnants we can expect in the galactic neighbourhood. Recently, Christlieb et al. (2002); Frebel et al. (2005), and Caffau et al. (2011) discovered very promising candidates and following generations of telescopes have to check this assumption.

- When and under what conditions does the formation of Pop III stars end and transform into another star formation channel? In the preionised Universe with still primordial abundances, a second generation of stars (so called "Pop III.2" stars) might form. The higher electron abundance boosts the HD abundance and therefore provides another efficient cooling channel at low temperatures (Greif et al. 2008; Turk et al. 2009; Clark et al. 2011a; Glover 2013). Consequently, the gas is more susceptible to fragmentation and hence Pop III.2 stars are thought to have lower masses on average than Pop III.1 stars (Clark et al. 2011a; Hosokawa et al. 2012; Clark & Glover 2013). The formation of Population II stars is marked by a critical metallicity of around $Z_{\mathrm{crit}} \simeq -3.5$ (Greif et al. 2008).
- Another fundamental uncertainty are the values of rate coefficients for certain reactions in the primordial gas (see section 1.3.1).

However, Glover et al. (2008) doubt at the end of their discussion that any of these processes might change the overall picture of Pop III star formation considerably.

1.4 Theory of Optically Thick H_2 Line Cooling

Since molecular hydrogen is the dominant coolant in primordial gas, we want to focus on its cooling properties in the optically thin and thick regime and on the underlying equations of line transfer.

1.4.1 Optically Thin H_2 Line Cooling

H_2 cooling relies on rovibrational transitions of the H_2 molecule. Hence, we have to understand the concept of radiative transfer and the level populations for these rovibrational states (the first part of this section is mainly based on Dullemond 2013). The radiative transitions between level populations is described by the radiative transfer equation

$$\frac{\mathrm{d}I_\nu}{\mathrm{d}s} = j_\nu - \alpha_\nu I_\nu, \tag{1.50}$$

where the index ν indicates the dependence on frequency. For a spontaneous radiative decay from level i to level j ($E_i > E_j$) with the line profile function $\phi_{ij}(\nu)$ (see Equation 2.1), the emissivity is given by

$$j_{ij,\nu} = \frac{h\nu_{ij}}{4\pi} N_i A_{ij} \phi_{ij}(\nu), \tag{1.51}$$

where N_i is the occupation number density of state i, $h\nu_{ij} = E_j - E_i = E_{ij}$ is the energy separation of the levels and A_{ij} is the Einstein A-coefficient. Similarly we determine the extinction coefficient by

$$\alpha_{ij,\nu} = \frac{h\nu_{ij}}{4\pi}(N_j B_{ji} - N_i B_{ij})\phi_{ij}(\nu) \tag{1.52}$$

with the Einstein B-coefficients B_{ij} and B_{ji}. The Einstein relations

$$A_{ij} = \frac{2h\nu_{ij}^3}{c^2} B_{ij} \tag{1.53}$$

$$B_{ij} = \frac{g_j}{g_i} B_{ji} \tag{1.54}$$

relate the Einstein coefficients to one-another, where g_i and g_j are the statistical weights of the individual levels. In local thermodynamic equilibrium (LTE) the levels are populated thermally ($N_i/N_j = g_i/g_j \exp[-(E_i - E_j)/k_B T]$) and the radiative transfer equation can be solved straightforwardly (knowing the relevant molecular lines, levels and rates). If the populations are not in LTE, different regions of the gas might have different level populations. Hence, we have to solve the equation of statistical equilibrium

$$\sum_{j>i} n_j A_{ji} - \sum_{j<i} n_i A_{ij} + \sum_j [n_j C_{ji} - n_i C_{ij}] = 0, \tag{1.55}$$

where n_i and n_j are the fractional occupation numbers and C_{ij} and C_{ji} are the collision rates between the levels. Since the collision rates generally depend on the local temperature, density and chemical composition of the gas, different regions of the cloud are no longer radiatively coupled and the problem of line transfer becomes non-trivial. Before we explain commonly used approximations to this problem, we briefly highlight the special properties of molecular hydrogen as the dominant coolant in primordial gas:

- It is a symmetric molecule. Hence, it has no permanent dipole moment and can only produce quadrupole radiation, which generally has a much smaller A_{ij}.
- It therefore has only rovibrational transitions (Le Bourlot et al. 1999).
- Its lowest energy level is at $T = 512$K. Hence, H_2 is a poor coolant at low temperatures (Clark & Glover 2013; Glover 2013).
- It has to obey the selection criterion of $\Delta J = \pm 2$ due to the missing dipole moment.
- For a given perturber density, rotational excitation is dominated by collisions with He and H_2, whereas rovibrational excitation is dominated by collisions with H (Le Bourlot et al. 1999).

- Its cooling rate drops exponentially for decreasing T and it can only cool the gas to $T \simeq 100\mathrm{K}$ (Clark & Glover 2013).
- Its cooling is due to a number of lines without a single dominant line (Haardt et al. 2002).

As we have seen before, radiative cooling is fundamentally different in LTE (at high densities) than in non-LTE (at low densities). A commonly used approximation to model the cooling rates is the one proposed by Galli & Palla (1998), which is based on the idea by Hollenbach & McKee (1979) to interpolate the LTE and non-LTE case according to

$$\Lambda_{\mathrm{H}_2}[n_{\mathrm{H}}, T_g] = \frac{\Lambda(\mathrm{LTE})}{1 + [n_{\mathrm{cr}}/n_{\mathrm{H}}]}, \tag{1.56}$$

where $\Lambda(\mathrm{LTE})$ is the LTE cooling function, n_{cr} is the critical density defined as

$$\frac{n_{\mathrm{cr}}}{n_{\mathrm{H}}} = \frac{\Lambda_{\mathrm{H}_2}(\mathrm{LTE})}{\Lambda_{\mathrm{H}_2}[n_{\mathrm{H}} \to 0]}, \tag{1.57}$$

and $\Lambda_{\mathrm{H}_2}[n_{\mathrm{H}} \to 0]$ is the low-density limit of the cooling function, which is independent of the hydrogen number density n_{H}. The latter depends only on the collisional and radiative deexcitation coefficients, which are introduced above. The temperature dependent approximation of this function yields

$$\begin{aligned} \log(\Lambda_{\mathrm{H}_2}[n_{\mathrm{H}} \to 0]) = &- 103.0 + 97.59 \log(T_g) - 48.05(\log(T_g))^2 \\ &+ 10.80 \log(T_g)^3 - 0.9032(\log(T_g))^4 \end{aligned} \tag{1.58}$$

in the range $10\mathrm{K} \leq T_g \leq 10^4\mathrm{K}$. This approximation is widely used e.g. by Yoshida et al. (2006) who uses it in the low density limit and apply a fit by Hollenbach & McKee (1979) for the LTE-case. A comparison of both cooling rates can be seen in Figure 1.15. Although their approximation yields accurate results in most relevant cases, one important caveat of their method is that they only account for collisions with atomic hydrogen. Hence, we apply the cooling function described by Glover & Abel (2008) in our simulations, who model rotational and vibrational line emission from H_2 that includes collisions of H_2 with H, He, H_2, protons, and electrons. A detailed discussion of their approach can be found in Glover & Abel (2008), whereas we briefly summarise their results graphically in Figure 1.16. Their cooling rates are generally higher than those determined by Galli & Palla (1998). The optically thin cooling rates can be applied up to densities of $n \simeq 10^9\,\mathrm{cm}^{-3}$. Above this density, most H_2 lines become optically thick and we have to use another approach.

1.4.2 Escape Probability Method

So far we assume that the photons, which are emitted in the rovibrational transitions, can escape the cloud freely (without being scattered or absorbed) and therefore

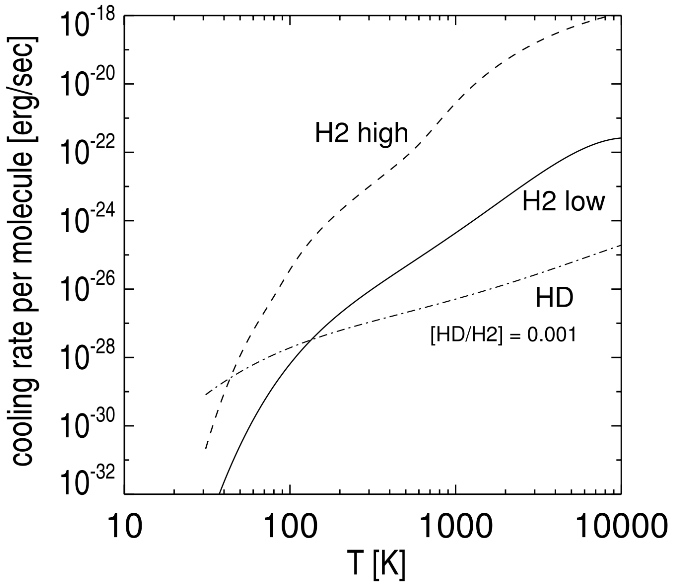

Figure 1.15: Radiative cooling rates per molecule as a function of temperature. Non-LTE (low density limit $n_H = 1\,\mathrm{cm}^{-3}$) for H_2 (solid line) and LTE (high density limit) cooling function for H_2 (dashed line). Adopted from Yoshida et al. (2006).

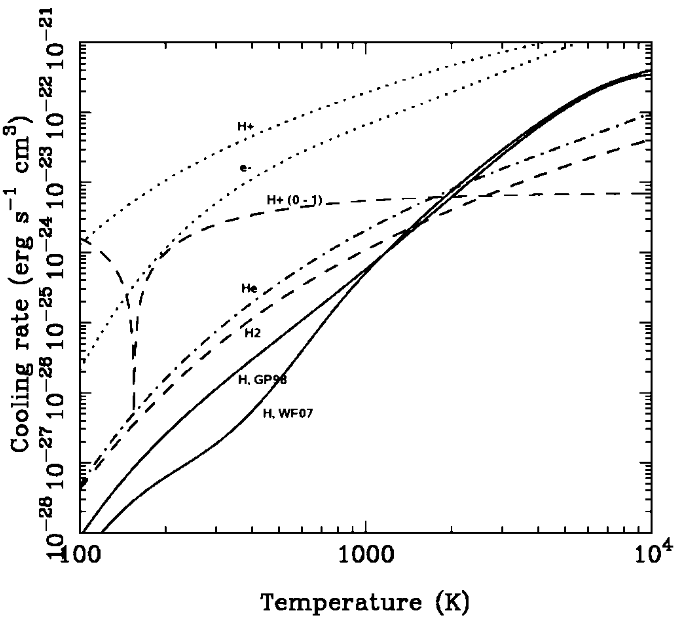

Figure 1.16: H_2 cooling rates per molecule, computed for $n = 10^{-4}\,\mathrm{cm}^{-3}$, for collisions with H (lower solid line), H_2 (lower dashed line), He (dash-dotted line), e^- (lower dotted line), and H^+ (upper dotted line). In every case an ortho-para ratio of 3:1 is assumed. H^+ actually heats the gas at $T \lesssim 150$. Also shown is the widely used Galli & Palla (1998) cooling function (upper solid line), which considers only collisions between H and H_2. Adopted from Glover & Abel (2008).

transport thermal energy outwards effectively. In the optically thick case, we have to consider scattering and absorption events that might capture the photons and hence decrease the overall cooling efficiency. These scattering, absorption, and stimulated emission events introduce a coupling between the individual level populations and the intensity of the radiation in the lines connecting them (Elitzur 1992). In order to tackle this problem one generally assumes complete redistribution of the frequency. This means that the molecule has enough time between an absorption and emission event, to redistribute its velocity (and thereby the Doppler-shifted frequencies of its spectral lines) completely. Otherwise, the current velocity has to be assigned to each molecule individually, which complicates the problem by introducing more dimensions.

The most common approach to solve the problem of optically thick cooling is the "escape probability method". Following Emerson (1996) and Kogure & Leung (2007), we determine the possibility that a single photon with frequency ν might escape the cloud to be

$$p_\nu = e^{-\tau_\nu}, \tag{1.59}$$

where τ_ν is the optical depth to the cloud's surface. For a specific line with the line profile function ϕ_ν the escape probability is given by

$$\beta_e = \int_0^\infty \phi_\nu p_\nu \mathrm{d}\nu. \tag{1.60}$$

In order to determine this escape probability, we have to understand the dynamics of the cloud. If the photon is emitted in the centre of the cloud and an envelope of gas is moving towards it with a constant velocity gradient $\mathrm{d}v/\mathrm{d}s$, then the photon observes the spectral lines of the envelope to be Doppler-shifted with respect to its rest frame. Assuming the photon's line profile to have a Doppler width $\Delta\nu_{\mathrm{th}}$ (see section 2.1.1) and a central frequency ν_0, we can determine the characteristic distance L after which the lines appear to be Doppler-shifted by one thermal line width of the photon. This characteristic distance L is related to a difference in radial velocities

$$\Delta v = \frac{\mathrm{d}v}{\mathrm{d}s} L = \frac{\Delta\nu_{\mathrm{th}}}{\nu_0} c. \tag{1.61}$$

Commonly one assumes the photon to escape freely after it has travelled this distance L, because its line profile is shifted and the possibility of reabsorption is very small beyond this point. Introducing the relative line displacement

$$x = (\nu - \nu_0)/\Delta\nu_{\mathrm{th}} \tag{1.62}$$

we can determine the optical depth by

$$\tau = \frac{\kappa'}{\Delta\nu_{\rm th}}\rho\int_0^\infty \phi_x(x - s/L)\mathrm{d}s, \tag{1.63}$$

where κ' is the absorption coefficient integrated over the whole absorption line. Applying the substitutions $x' = x - s/L$ and $\mathrm{d}s = -L\mathrm{d}x'$ we rewrite this expression as

$$\tau = \tau_s \int_{-\infty}^{x} \phi_x(x')\mathrm{d}x', \tag{1.64}$$

where

$$\tau_s = \kappa'\rho\frac{L}{\Delta\nu_{\rm th}}. \tag{1.65}$$

The escape probability at frequency shift x is then given by

$$p_\nu = \exp\left[-\tau_s\int_{-\infty}^{x}\phi_x(x')\mathrm{d}x'\right]. \tag{1.66}$$

Performing the frequency average (Equation 1.60) yields

$$\beta_e = \int_0^\infty \phi(x)\exp\left[-\tau_s\int_{-\infty}^{x}\phi_x(x')\mathrm{d}x'\right]\mathrm{d}x. \tag{1.67}$$

By introducing the integration variable

$$\eta = \int_{-\infty}^{x}\phi_x(x')\mathrm{d}x' \tag{1.68}$$

we can determine the escape probability to be

$$\beta_e = \int_0^1 e^{-\tau_s\eta}\mathrm{d}\eta = \frac{1-e^{-\tau_s}}{\tau_s}. \tag{1.69}$$

In this approximation, the optical thickness

$$\tau_s = \frac{\kappa'\rho}{\nu_0}\frac{c}{\mathrm{d}v/\mathrm{d}s} \tag{1.70}$$

corresponds to the optical thickness of the characteristic length L. Although the problem seems to be solved, the escape probability still has to be averaged over all possible directions

$$\langle\beta_e\rangle = \frac{1}{4\pi}\int\beta_e\mathrm{d}\Omega, \tag{1.71}$$

with generally angle dependent velocity gradient and density, which complicates the problem and requires further assumptions and approximations. Nonetheless, the escape probability method decouples the level populations from the line transfer problem (Lockett & Elitzur 1989) and therefore simplifies optically thick cooling. Historically, the "escape probability" idea is quite old and has been developed over the years. During its development, both a lot of improvements and false assumptions have been made. Since we will refer to these papers, approximations and assumptions afterwards and we have to understand the basic concepts, variations and shortcomings, it is worth to briefly review the historical development:

- Ambartsumian (1933) studied motionless nebula, where the photon can escape from any optical depth, if it is emitted in the wings of a line.

- Assuming a monotonic velocity field and a parallel slab of gas, Zanstra (1934) was the first who derived an escape probability. For simplification, he assumed the absorption coefficient to be non-zero only in the interval $[\nu_0 - \Delta\nu_{\mathrm{th}}, \nu_0 + \Delta\nu_{\mathrm{th}}]$, although there might be absorption and emission events in the wings of the line profile.

- Sobolev (1947) derived the escape probability for constant velocity gradients in his study of expanding envelope. Based on Zanstra (1934) he assumed the absorption coefficient to be zero outside the interval $[\nu_0 - \Delta\nu_{\mathrm{th}}, \nu_0 + \Delta\nu_{\mathrm{th}}]$. This simplification leads to an underestimation of the effective cooling rate as we see in section 5.1.1. Commonly, people refer to the English translation (Sobolev 1960) of Sobolev's original work from 1947 (which was written in Russian).

- A few years later, Sobolev (1957) reinvestigated this problem and assumed a three-dimensional medium, which consists of plane parallel layers. For very large velocity gradients, the escape probability does not depend on the specific shape of the line profile function. He already mentioned that the accuracy of this approach increases with increasing velocity gradient in the medium and derived the escape probabilities for a rectangular line profile and for a Doppler profile:

  $$\beta_{\mathrm{rect}} = \frac{1}{2u}\frac{\mathrm{d}v}{\mathrm{d}\tau}, \qquad \beta_{\mathrm{dopp}} = \frac{1}{\sqrt{\pi}u}\frac{\mathrm{d}v}{\mathrm{d}\tau}, \tag{1.72}$$

  where u is the characteristic width of the profiles.

- Weymann & Williams (1969) numerically analysed the escape probabilities by determining the optical depths for Doppler profiles. For this purpose, they considered the absorption coefficients to be non-zero within the frequency interval $[\nu_0 - 6\Delta\nu_{\mathrm{th}}, \nu_0 + 6\Delta\nu_{\mathrm{th}}]$.

- Castor (1970) was the first who derived an expression for the escape probability in a spherical symmetric case.

- Lucy (1971) explicitly assumed the narrow line limit (line profile is only affected within one thermal line width) for his study of expanding atmospheres with spherical symmetry.
- Hummer & Rybicki (1982) analysed the escape probability for different line profile functions in static and moving media. They found out that extremely large optical depths are required to match the $\beta_{\rm dopp}$ case, if the profile is actually dominated by the natural line width (described by a Lorentzian profile). Moreover, they concluded that photons in optically thick medium remain comparatively localised until they escape the medium in one long flight.
- Gnedin et al. (2008) used the escape probability method to determine the escape fraction of ionising radiation from high-redshift galaxies and found an average angular value of $\beta = 1 - 3\%$, whereas the escape fraction varies by more than one order of magnitude along different lines of sight.

Most important for our further discussion is the application of the escape probability method by Yoshida et al. (2006) to the case of optically thick cooling in primordial gas. The cooling rate in an optically thick medium is then given by

$$\Lambda_{\rm H_2\,,thick} = \sum_{l,u} E_{lu} A_{lu} \beta_{{\rm esc},lu} n_u, \tag{1.73}$$

where n_u is the population density of hydrogen molecules in the upper level, E_{lu} is the energy separation between the lower and upper level, and $\beta_{{\rm esc},lu}$ is the probability for an emitted line photon to escape without absorption. Based on our derivation, the escape probability is given by

$$\beta_{{\rm esc},lu} = \frac{1 - e^{-\tau_{lu}}}{\tau_{lu}}, \tag{1.74}$$

where τ_{lu} is the opacity at the line centre. Since the absorption coefficient for a transition from the lower to the upper level is given by

$$\alpha_{lu} = \frac{E_{lu}}{4\pi} n_l B_{lu} \left[1 - \exp\left(\frac{-E_{lu}}{k_B T}\right)\right] \phi(\nu), \tag{1.75}$$

we can express the opacity as

$$\tau_{lu} = \alpha_{lu} L_{\rm char}, \tag{1.76}$$

where $L_{\rm char}$ is a characteristic length scale (Castor 1970; Goldreich & Kwan 1974; de Jong et al. 1975; Stahler & Palla 2005). According to Equation 1.75 the expression $\alpha_{lu}/n_{\rm H_2}$ is a function only on temperature. Following Clark et al. (2011a) we express the optical depth by

$$\tau_{lu} = \left(\frac{\alpha_{lu}}{n_{\mathrm{H_2}}} \right) n_{\mathrm{H_2}} L_{\mathrm{char}}, \tag{1.77}$$

where

$$n_{\mathrm{H_2}} L_{\mathrm{char}} = N_{\mathrm{H_2},\mathrm{eff}} \tag{1.78}$$

defines an effective column density. Hence, the last task for the determination of optically thick cooling is the determination of the effective column density and the characteristic length. Knowing these quantities, we can generally determine the angular dependent escape probability and afterwards average it over the total sphere and all relevant rovibrational lines. A common assumption is spherical symmetry, such that

$$\langle \beta_{\mathrm{esc}} \rangle = \beta, \tag{1.79}$$

whereas Yoshida et al. (2006) proposed an average over three orthogonal directions

$$\beta = \frac{\beta_x + \beta_y + \beta_z}{3}. \tag{1.80}$$

In section 5.1.3 we confirm the necessity of a proper angular average in order to capture the dynamics of the collapse. The averaged escape probability relates the optically thin and optically thick cooling rate by

$$\Lambda_{\mathrm{H_2},\mathrm{thick}} = \beta \cdot \Lambda_{\mathrm{H_2},\mathrm{thin}} \tag{1.81}$$

and is therefore also know as “opacity correction”. Since we mostly use binned, mass averaged representations of the opacity correction, one should still keep in mind that there is actually a scatter as illustrated in Figure 1.17. For a given density, there is a possible range of opacity corrections. This is due to the dependence on the velocity profile and temperature.

1.4.3 Sobolev Approximation

A widely used method for the determination of the effective column density is the “Sobolev approximation” (Sobolev 1947, 1957). This approximation has been used in many simulations of primordial star formation (Yoshida et al. 2006, 2008; Turk et al. 2011; Clark et al. 2011a,b; Greif et al. 2011; Wolcott-Green et al. 2011; Greif et al. 2012; Hirano & Yoshida 2013; Stacy et al. 2013; Hirano et al. 2013; Stacy & Bromm 2013; Greif et al. 2013). The main idea is based on the Doppler-shift of spectral lines due to the velocity gradient (Equation 1.61). According to Sobolev, a photon is not absorbed and can escape freely, if the spectral lines of a possibly absorbing H_2 molecule are shifted by more than one thermal line width. In terms of

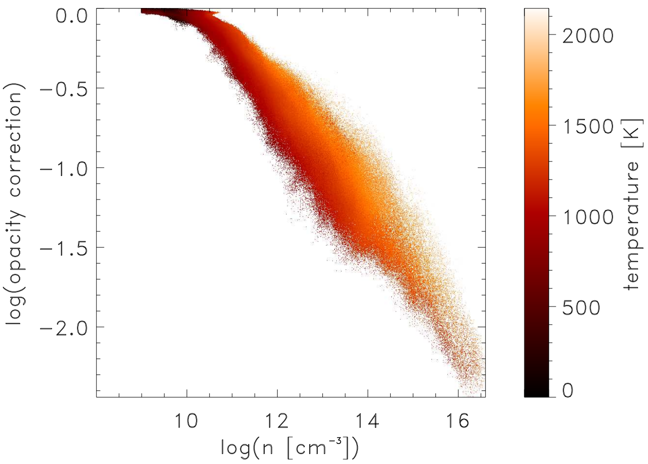

Figure 1.17: Opacity correction as a function of density for a representative snapshot. For a given density, the opacity correction might scatter within a certain range, depending on the local cloud properties.

the (constant) velocity gradient, this criterion can be expressed as a typical length scale after which a photon might not be reabsorbed. This length scale is known as the Sobolev length

$$L_{\rm sob} = \frac{\Delta v_{\rm th}}{|{\rm d}v_r/{\rm d}r|}. \tag{1.82}$$

Phrased differently, all relevant matter that might reabsorb a photon is within its Sobolev length. Therefore, the effective column density (Equation 1.78) can be determined by

$$N_{\rm H_2,eff} = n_{\rm H_2} L_{\rm sob}. \tag{1.83}$$

Since the velocity divergence captures the three-dimensional dynamics of the collapse, one normally uses

$$L_{\rm sob} = \frac{\Delta v_{\rm th}}{|\vec{\nabla}\cdot\vec{v}|} \tag{1.84}$$

for the determination of the Sobolev length (Neufeld & Kaufman 1993). A fundamental problem of the Sobolev approximation was already mentioned by several authors: both, the velocity gradient and the number density have to be constant within one Sobolev length (Lucy 1971; Bujarrabal et al. 1980; Hummer & Rybicki 1992; Neufeld & Kaufman 1993; Wolcott-Green et al. 2011), because otherwise the integrals can not be simplified in the applied manner. The validity of this assumption is analysed in section 5.1.2.

2 Cooling Approaches

Radiative cooling is a crucial process in primordial star formation. In this section we present several cooling approaches, which will be compared in the following chapters of the Master Thesis.

2.1 Sobolev Correction

The Sobolev method is the most commonly used approximation for optically thick H_2 cooling. However, the original formula, proposed by Sobolev (1947) need revision, which is discussed in the following sections.

2.1.1 Line Profiles

Generally, there are different effects that shape the line profile function $\phi(\nu)$. First of all, the thermal motion of the gas particles causes a Doppler-broadening of spectral lines. This effect can be expressed as a Gaussian profile

$$\phi(\nu) = \frac{1}{\Delta\nu_{\mathrm{th}}\sqrt{\pi}} \exp\left(-\frac{(\nu-\nu_0)^2}{{\Delta\nu_{\mathrm{th}}}^2}\right) \tag{2.1}$$

with the central frequency of the line ν_0 and the thermal line width for molecular hydrogen

$$\Delta\nu_{\mathrm{th}} = \nu_0 \frac{v_{\mathrm{th}}}{c} = \frac{\nu_0}{c}\sqrt{\frac{kT}{m_{\mathrm{H}}}}. \tag{2.2}$$

Furthermore, collisional broadening and the natural line width, which can both be described by Lorentz profiles, should take into account (Dullemond 2013). For molecular clouds however the dominant broadening mechanism is the thermal broadening due to the Doppler effect and we can properly approximate the line profile by a Gauss function and neglect all deviations from this shape.

2.1.2 Line Overlap

According to the Sobolev approximation a photon can escape freely from the optically thick gas after one Sobolev length L_S. This length scale is directly related to a shift of spectral lines in velocity space: after one Sobolev length, the spectral line of the escaping photon is Doppler-shifted by one thermal line width $\Delta\nu_{\mathrm{th}}$ with respect to the spectral line of the possibly absorbing H_2 molecule. For simplicity Sobolev (1947) assumed the absorption coefficient to be zero outside the interval $[\nu_0 - \Delta\nu_{\mathrm{th}}, \nu_0 + \Delta\nu_{\mathrm{th}}]$ and therefore ignored all possible absorption events beyond this point. This frequency range and the relative overlap of line profiles after one Sobolev length are shown in Figure 2.1. From there we can determine the line overlap after one Sobolev length to be 62% (see Equation 2.3). Since the overlap of spectral lines indicates the absorption probability, we can conclude that we have a non-negligible absorption possibility beyond one Sobolev length and therefore we need a correction in order to cover the additional matter beyond one Sobolev length. The overlap is linearly proportional to the absorption probability and hence the next step is the quantification of the relative overlap as a function of the line displacement. In terms of the relative line displacement (Equation 1.62) we are interested in the overlap $o(x)$. According to the right plot in Figure 2.1 this problem is symmetric with respect to the intersection point of the blue and red profile. Therefore, we can determine the overlap by

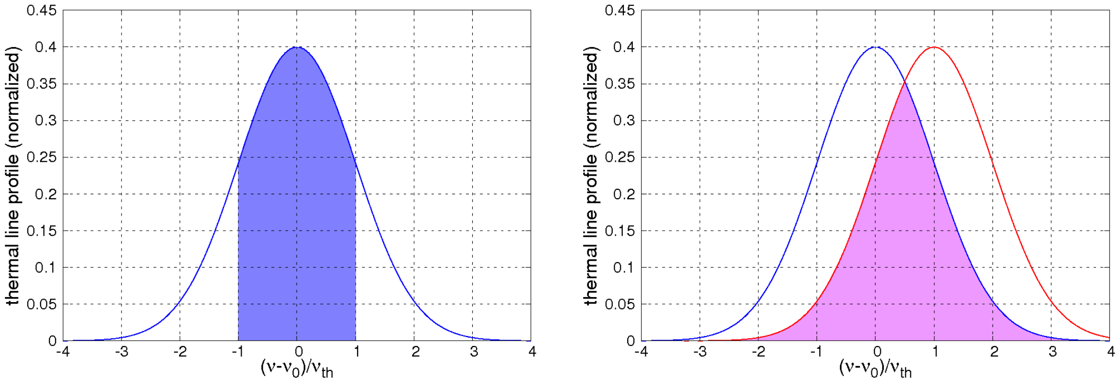

Figure 2.1: Normalised thermal line profiles of H_2 lines as a function of frequency in units of the thermal line width $\Delta\nu_{\mathrm{th}}$. Left: the blue area indicates the frequency range in which Sobolev assumed a non-zero absorption coefficient. Right: the red profile is shifted by one thermal line width with respect to the blue profile. The overlapping area is marked in magenta and shows a relative overlap of 62%.

$$o(x) = 2\int_{-\infty}^{x/2} \frac{1}{\sqrt{2\pi}} \left[\exp\left(-\frac{1}{2}\nu^2\right) - \exp\left(-\frac{1}{2}(\nu - x)^2\right)\right] \mathrm{d}\nu. \tag{2.3}$$

This function is illustrated in Figure 2.2 up to a line displacement of $x = 10$. From this figure we see once more that we have to take care of the line overlap beyond one Sobolev length because the relative line overlap after three Sobolev lengths is for example still 13%.

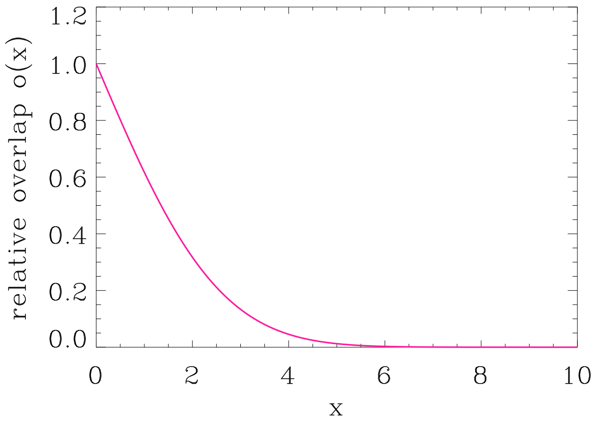

Figure 2.2: Relative line overlap $o(x)$ as a function of the line displacement x. There is still a non-negligible overlap of spectral lines beyond one Sobolev length ($x = 1$).

2.1.3 Effective Column Density

In order to find a proper correction for this overlap, we have to step back a little bit and consider the basic definition of the column density

$$N = \int_0^\infty n_{\mathrm{H}_2}\,\mathrm{d}r, \tag{2.4}$$

where r is the radial coordinate and n_{H_2} is the number density of molecular hydrogen. The column density thus represents the amount of H_2 integrated along one line of sight. However, we are not interested in the total column density but rather in the effective column density which includes only the gas that could be relevant for the reabsorption of escaping H_2 line photons. The Sobolev approximation gives a very simple answer to the question which gas we have to include in the effective column density, namely all gas within one Sobolev length. Expressed in terms of line overlap we write this as

$$N_{\mathrm{sob}} = \underbrace{\int_0^{L_{\mathrm{sob}}} 1 \cdot n_{\mathrm{H}_2}\,\mathrm{d}r}_{100\%\ \text{overlap}} + \underbrace{\int_{L_{\mathrm{sob}}}^\infty 0 \cdot n_{\mathrm{H}_2}\,\mathrm{d}r}_{0\%\ \text{overlap}} = n_{\mathrm{H}_2}\,L_{\mathrm{sob}}. \tag{2.5}$$

In the last step a constant number density of molecular hydrogen is assumed. This is a great simplification whose validity is checked in section 5.1.2. Thus, Sobolev overestimated the overlap and therefore the matter contributions within one Sobolev length but neglected all matter contributions beyond one Sobolev length. Since we want to account for the true overlap of spectral lines, we introduce the relative line overlap $o(x)$ as a weighting function into this determination of the effective column density:

$$N_{\mathrm{eff}} = \int_0^\infty o(x) n_{\mathrm{H}_2} \, \mathrm{d}r \tag{2.6}$$

The remaining problem is to relate the line displacement x to the distance r along the line of sight. Assuming a constant velocity gradient along the line of sight, we can rewrite Equation (1.82) into

$$\mathrm{d}r = \frac{L_{\mathrm{sob}}}{v_{\mathrm{th}}} \mathrm{d}v_{\mathrm{r}} \tag{2.7}$$

and transform the radial integration into an integration in velocity space

$$N_{\mathrm{eff}} = \int_0^\infty o(x) n_{\mathrm{H}_2} \frac{L_{\mathrm{sob}}}{v_{\mathrm{th}}} \mathrm{d}v_{\mathrm{r}}. \tag{2.8}$$

Assuming the number density to be constant, we rewrite this as

$$N_{\mathrm{eff}} = n_{\mathrm{H}_2} \, L_{\mathrm{sob}} \int_0^\infty o(x) \frac{\mathrm{d}v_{\mathrm{r}}}{v_{\mathrm{th}}} \tag{2.9}$$

and replace the integration over the radial velocity by an integration over the relative line displacement

$$N_{\mathrm{eff}} = n_{\mathrm{H}_2} \, L_{\mathrm{sob}} \int_0^\infty o(x) \mathrm{d}x. \tag{2.10}$$

The numerical solution of this integral is

$$\int_0^\infty o(x) \mathrm{d}x = 1.694, \tag{2.11}$$

which hence is the correction factor for the Sobolev approximation:

$$N_{\mathrm{eff}} = 1.694 \cdot N_{\mathrm{sob}} \tag{2.12}$$

In other words, the relevant column density for the determination of the escape probability of line photons is about 1.7 times higher than originally assumed by Sobolev. A simplified illustration of the Sobolev approximation and its corrected version can be seen in Figure 2.3. Although we correct for the line overlap, we should still keep in mind that this derivation implies some assumptions (e.g. constant velocity gradient or constant density) whose validity is checked in section 5.1.2.

2.1.4 Overlap with Other Lines

Molecular hydrogen has more than two hundred spectral lines in the range $1.0\mu\mathrm{m} \leq \lambda \leq 32\mu\mathrm{m}$ which could be relevant for cooling in primordial gas (Ripamonti et al.

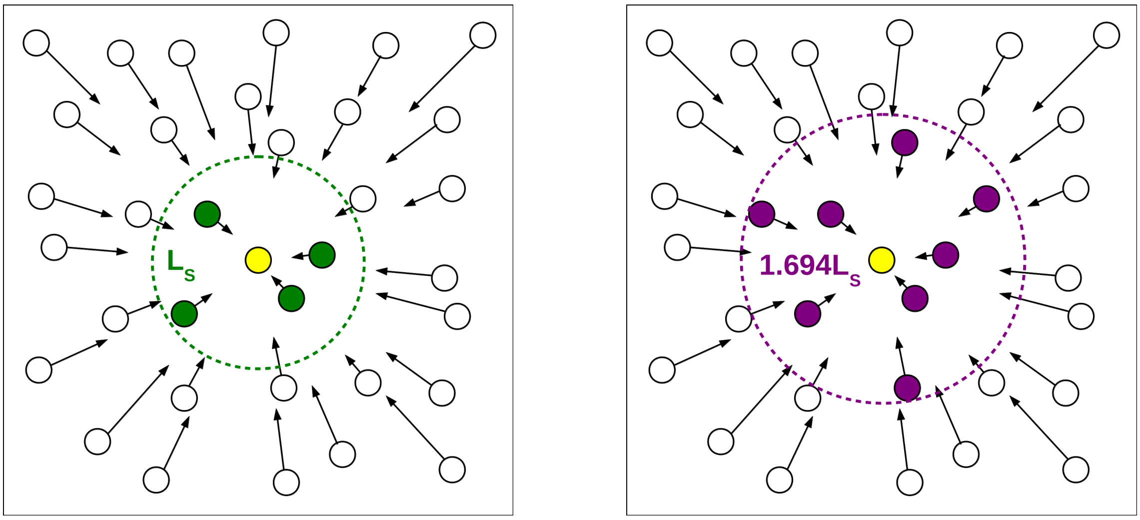

Figure 2.3: Illustration of the Sobolev approximation (left) and the corrected Sobolev approximation (right). The black arrows indicate the relative velocities (which are irrelevant for these approximations). In both cases we want to determine the column densities for the central yellow particle and therefore determine the corresponding Sobolev lengths. For the commonly used Sobolev approximation we include all mass within one Sobolev length, whereas for the corrected approximation we include all mass within 1.694 Sobolev lengths.

2002). An illustration of these lines at different temperatures is given in Figure 2.4. Since these lines appear to be very close to each other, we should check the possibility that a photon is emitted in one line with a certain frequency and absorbed by another line which is Doppler-shifted into the emitting frequency. An illustration of this phenomena is given in Figure 2.5. In order to do so, we should not just check the overlap between one and the same line but also between different lines in the spectrum of molecular hydrogen. Ripamonti et al. (2002) provide a table with all relevant lines and the line total luminosities. We model the spectrum of molecular hydrogen according to this information, using Gaussian profiles for the individual lines. When there is no velocity gradient and therefore no Doppler-shift of spectral lines towards each other, the relative overlap of different lines is of the order of 10^{-6}. Whereas, if we assume a velocity gradient and determine the relative overlap of different spectral lines up to a line displacement of $x = 10$, we find out that the maximum relative overlap is of the order of 10^{-5} which is still much less than the average overlaps between one and the same line. Therefore, we can conclude that this effect is negligible for our calculations.

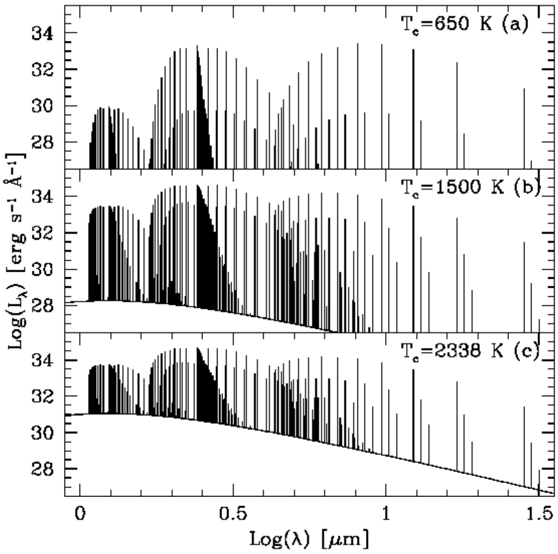

Figure 2.4: Emitted spectra when the central temperature is (a) 650K, (b) 1500K, and (c) 2338K. Line widths are actually smaller than the lines in this plot, so that overlaps are only apparent. Adopted from Ripamonti et al. (2002).

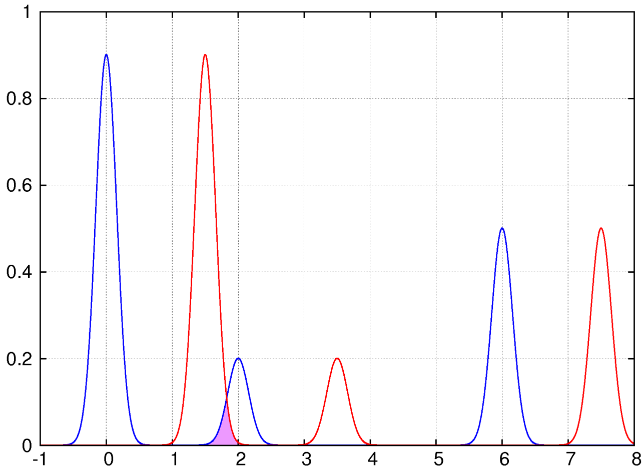

Figure 2.5: Exemplary spectrum of molecular hydrogen. Illustration of different spectral lines that might be Doppler-shifted into each other. The overlap of different lines is marked in magenta.

2.2 TreeCol

The main problem of the Sobolev approximation is that we have to stick to local quantities and therefore neglect all information about density gradients, velocity profile and the actual shape of the cloud like deviations from spherical symmetry. Generally, the most exact way to determine effective column densities in SPH might be to sum up all relevant mass along all possible lines of sight for each particle individually for every timestep. In order to avoid this extremely high computational effort, Clark et al. (2012) invented the TreeCol algorithm which determines column densities using the tree structure, which is already present in many gravitational N-body solvers.

2.2.1 General Idea

The general idea of TreeCol is to create a spherical map of column densities around each particle. In contrast to direct summation of all particle contributions, TreeCol makes use of the particle grouping in the tree, which is illustrated in Figure 2.6. Generally, the shape and positions of the pixels on the sphere are arbitrary but since we want to determine the effective column densities and related photon escape probabilities for each pixel and average them over the entire sphere, the pixels should have equal areas. For this purpose TreeCol uses a spherical pixelation based on HEALPix (Górski et al. 2005). Originally designed for harmonic decomposition and the determination of the CMB power spectrum, HEALPix matches a lot of our requirements: it creates a spherical map of equal area pixels, which are distributed along iso-latitude circles as it can be seen in Figure 2.7. During the walk of the tree for the determination of the gravitational force, all relevant data for the column

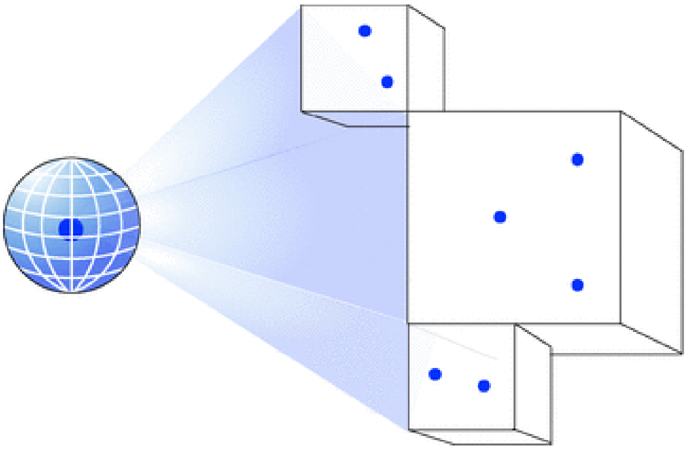

Figure 2.6: Schematic illustration of the TreeCol algorithm. The particles are already clustered into tree nodes (boxes). TreeCol creates a spherical map around each particle by projecting the mass contributions of the tree nodes onto the spherical grid. Adopted from Clark et al. (2012).

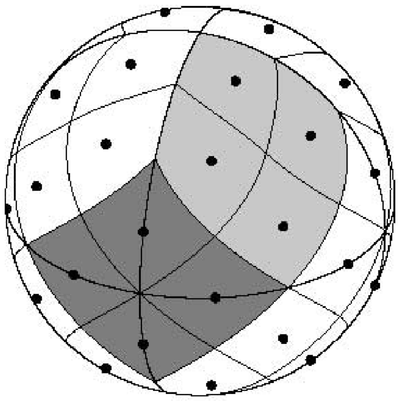

Figure 2.7: Distribution of diamond shaped pixels on the sphere following the HEALPix algorithm. We use a discretisation with 48 pixels which are distributed along iso-latitude circles. Adopted from Górski et al. (2005).

density map are collected and projected onto the spherical grid. The tree nodes are assumed to appear squarish in the sky. The code now has to check which pixels are affected by this particular node, which requires a common coordinate system for the tree node and the spherical map. Since we want to describe the spatial overlap of a pixel and the tree node by two angles $d\theta$ and $d\phi$ we have to avoid that the node is located at one of the poles of our spherical coordinate system. Therefore, we rotate the coordinate system into a new one where the node's position vector defines the new x-axis. Consequently, we determine the overlap between node and pixel unambiguously and hence the node's contribution to the ith pixel is given by

$$\Sigma_{\mathrm{cont},i} = \frac{d\theta d\phi}{p^2}\Sigma_n, \tag{2.13}$$

where p is the size of a pixel and Σ_n is the nth node's column density contribution (its mass divided by its area). Since the particle data are already stored in a tree, TreeCol can use this information and therefore reproduces the $N \log N$-scaling. However, in our simulations the usage of TreeCol slows down the simulation by a factor of about five with respect to a run without TreeCol. This slowdown is mainly related to the evaluation of several inverse trigonometric functions for each particle and pixel. Nevertheless, TreeCol provides a very exact way of determining column densities with an accuracy of better than 10%.

2.2.2 Using TreeCol to Determine Effective Column Densities

We use TreeCol to overcome several shortcomings of the Sobolev approximation. First of all, we do not have to assume a constant density because we directly sum up the individual contributions of the SPH particles. Furthermore we can use the velocity information of the tree nodes and do not have to assume a constant velocity gradient. Additionally, we account for the actual spatial matter distribution and do not have to stick to a crude one dimensional approximation. While the original TreeCol scheme includes all tree nodes (respectively particles), along the line of sight, we have to take into account the Doppler shifts and find a criterion for the determination of the tree nodes that we want to include and those which are irrelevant for the effective column density. In order to do so, we use the information about the relative velocities between the particle for which the column density map is created and the individual tree nodes, which are projected onto the spherical grid. We implement three different approaches to solve this problem.

Sobolev-like

Following the Sobolev approximation, all relevant mass for the column density is located within one Sobolev length. Translated into velocities, we should only include particles or tree nodes whose relative velocity is smaller than the thermal velocity. Thus, we modify TreeCol in order to include only mass contributions of nodes that fulfil this criterion. A schematic illustration of this approach is given in Figure 2.8. From there we already see that the relevant volume around a particle does not necessarily have to be spherically symmetric but can rather capture the dynamic shape of the cloud. Since we just switch on TreeCol for this approach but do not care about any overlap or corrections, this method will be labelled as "on".

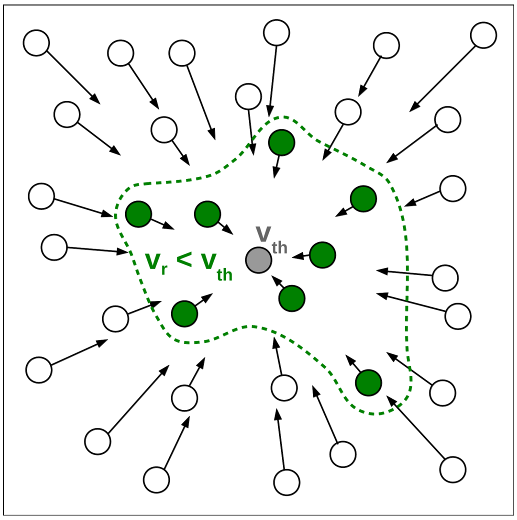

Figure 2.8: Illustration of the Sobolev-like criterion implemented in TreeCol. The black arrows indicate the relative velocities v_r. In order to affect the effective column densities of the grey target particle, the relative velocities of the tree nodes have to be smaller than the thermal velocity v_{th} of the target particle. Note that the relative velocities do not necessarily have to point towards this particle but can also be distributed more chaotically. In any case the absolute value of the relative velocity is relevant for the criterion. In this simple illustration the tree nodes are distributed randomly rather than being merged or split according to the true opening criterion.

Corrected Sobolev

Regarding the correction factor of 1.694 (Equation 2.12) for the effective column densities, the next possible approach might be to include all tree nodes whose relative velocities fulfil the criterion $|v_r| < 1.694 v_{th}$. Using this criterion, we take into account the non-negligible overlap beyond one Sobolev length. A schematic illustration of this approach is given in Figure 2.9. Again we see that this approach captures the dynamic shape of the cloud instead of using just a one-dimensional length scale. Since we assume a mean overlap of spectral lines for all particles in the relevant regime, we will label this method as “mean”.

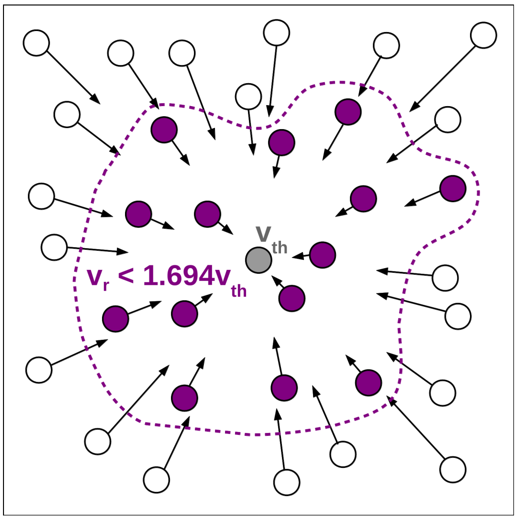

Figure 2.9: Illustration of the corrected Sobolev criterion implemented in TreeCol. The black arrows indicate the relative velocities v_r. In order to affect the effective column densities of the grey target particle, the relative velocities of the tree nodes have to fulfil $|v_r| < 1.694 v_{th}$. Note that the relative velocities do not necessarily have to point towards the target particle but can also be distributed more chaotically. In this simple illustration the tree nodes are distributed randomly rather than being merged or split according to the true opening criterion.

Lookup

There is still one shortcoming regarding the previously presented methods: although the Doppler-shifting of spectral lines is a smooth process, we so far define a clear cut off between particles that are included for the column density estimation and particles that are excluded. The overlap of spectral lines and therefore the relevance for the effective column density depends only on the relative velocity. Since we know this information for the individual tree nodes, we can weight their contributions to the column density map with their relative spectral line overlap. In order to do so, we have to determine the relative velocities, assign the associated overlap to the tree node and weight its column density contribution by this weighting factor. A schematic illustration of this approach is given in Figure 2.10. This approach will clearly yield the most accurate results because we do not rely on any assumptions (like a constant velocity gradient or number density), but capture the complete three dimensional collapse of the cloud and take care of the true line overlaps. Since we store the weighting factors for this approach in a lookup table, we will label this method as “lookup”.

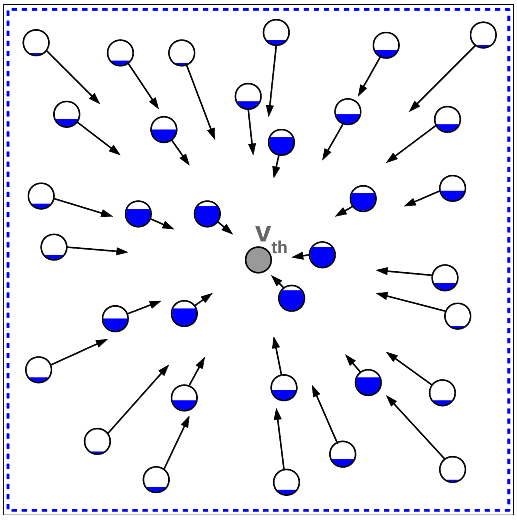

Figure 2.10: Illustration of the lookup method implemented in TreeCol. The black arrows indicate the relative velocities v_r. The contribution to the column density of each tree node is weighted by the relative overlap of spectral lines which in turn depends on the relative velocities between the tree node and the grey target particle. The weighting is illustrated by the partial filling of the nodes. Note that the relative velocities do not necessarily have to point towards the target particle but can also be more chaotic. In this simple illustration the tree nodes are distributed randomly rather than being merged or split according to the true opening criterion.

2.3 Further Approaches

Besides the commonly used Sobolev approximation and our new TreeCol-based methods, there are several other approaches. Two analytical fit formulas directly relate a given density to the opacity correction, whereas other one-dimensional methods use the local information of the cloud to determine the effective column density and hence the opacity correction. These methods are briefly presented in the following sections.

2.3.1 Gnedin

Gnedin et al. (2009) modelled molecular hydrogen and star formation in cosmological simulations. They determine H_2 column densities for the self-shielding of H_2 against

Lyman-Werner photons by using a "Sobolev-like" approximation. Therefore, they define a characteristic length scale

$$L_{\mathrm{Gnedin}} = \frac{n_{\mathrm{H}_2}}{|\vec{\nabla} n_{\mathrm{H}_2}|} \tag{2.14}$$

based on the number density and its gradient. The column density then is simply given by

$$N_{\mathrm{Gnedin}} = n_{\mathrm{H}_2} L_{\mathrm{Gnedin}}. \tag{2.15}$$

In one dimension the length scale L_{Gnedin} is the distance after which the number density has dropped to zero in a linear approximation. In three dimensions this can be seen as a first order approximation to Equation 2.4. In any case, this approach accounts for the density gradient, which is naturally present in molecular clouds. The accuracy of this method can be seen in Figure 2.11. They claim that this approximation provides a very good estimation for the column density in the range $3 \times 10^{20}\mathrm{cm}^{-2} < N_{\mathrm{HI}} + 2N_{\mathrm{H}_2} < 3 \times 10^{23}\mathrm{cm}^{-2}$. Although we are dealing with star formation on much smaller scales than they did, their method seems to be

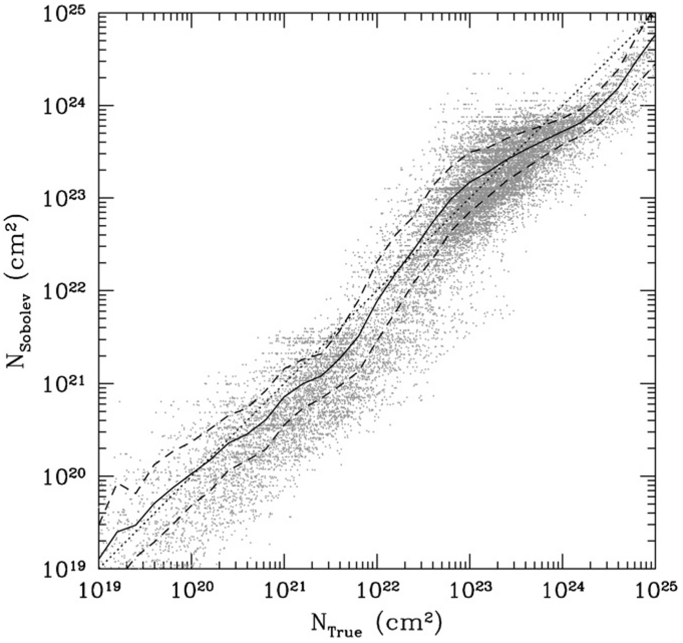

Figure 2.11: Comparison of the total hydrogen column density from the Sobolev-like approximation (which we label N_{Gnedin}) and the true column density as integrated along random lines of sight through the simulation box. Grey points show individual lines of sight; black solid lines show the average N_{Sobolev} for a given N_{True}, while black dashed lines give the rms scatter. The thin black dotted line is a diagonal of the plot. The units on the axis should actually be cm^{-2}. Adopted from Gnedin et al. (2009).

a reasonable, scale-invariant approach for the determination of column densities. Furthermore, this method depends only on local quantities and therefore is easy to implement in different codes. Nevertheless, we should keep in mind that this method includes no information about the velocity profile of the cloud and therefore neglects the enhanced photon escape probability due to the Doppler-shifting of lines.

2.3.2 Jeans

Since the Jeans length (Equation 1.18) is a typical length scale for gravitationally collapsing clouds, it might also be a good approximation for the column density. We determine the H_2 column density based on the Jeans length by

$$N_{\mathrm{Jeans}} = n_{\mathrm{H}_2}\,\lambda_J. \tag{2.16}$$

2.3.3 Gadget

In regions with a very small velocity divergence, the Sobolev length and therefore the column density might become artificially large. In order to avoid this problem, we can determine the column density by

$$N_{\mathrm{Gadget}} = \min[N_{\mathrm{Sobolev}}, N_{\mathrm{Jeans}}]. \tag{2.17}$$

When we use the (corrected) Sobolev approximation in our simulations, we actually use this slightly modified version in order to avoid artificially small photon escape probabilities. Since this method is originally implemented in Gadget2, we will label it as “Gadget”.

2.3.4 Reciprocal

One main goal of this Master Thesis is to find a method for the determination of column densities which is accurate, easy to implement and does not slow down the code. The TreeCol-based methods fulfil only the first criterion whereas the other presented methods fulfil only the last two criteria as we see in section 4.2. Therefore, we should find a method that only depends on local quantities of the collapse, is easy to implement but nevertheless captures the dynamics of the cloud and reproduces the TreeCol-based results.

The corrected Sobolev approximation (N_{Sobolev}) takes the line overlap into account but neglects the decreasing density and hence generally overestimates column densities. On the other hand, the Gnedin approximation (N_{Gnedin}) takes the decreasing number density into account but neglects the Doppler-shifting of lines. Since each method on its own generally overestimates column densities (as we see in section 4.2), the general idea behind this new approach is to combine these two methods in order to overcome their individual shortcomings. Mathematically there are several ways of combining these two characteristic length scales, but the most simple one providing the right limits is

$$\frac{1}{L_{\mathrm{rec}}} = \frac{1}{L_{\mathrm{Gnedin}}} + \frac{1}{L_{\mathrm{Sobolev}}}. \tag{2.18}$$

There is no derivation or proof for this formula, but it is physically motivated by fulfilling the required criteria in the two limiting cases:

- If both lengths are of the same order ($L_1 \simeq L_2$), the result should be smaller than both lengths ($L_{\mathrm{rec}} < L_1 \simeq L_2$), since each length individually overestimates the column density.
- If one length is significantly smaller than the other length $L_1 \ll L_2$, the result should be equal to the smaller one ($L_{\mathrm{rec}} \simeq L_1$), because after this smaller length the photon can escape freely anyway.

Following this methods, the number density is simply given by

$$N_{\mathrm{rec}} = n_{\mathrm{H}_2} L_{\mathrm{rec}}. \tag{2.19}$$

2.3.5 Analytical Fits

We are interested in the column densities in order to determine the opacity corrections (Equation 1.81) for the H_2 line cooling. Besides the previously presented methods, there are two analytical fit functions that directly relate a given number density of the gas to the opacity correction. The first fitting function

$$\beta = \min\left[1, (n/n_0)^{-0.45}\right] \tag{2.20}$$

with $n_0 = 8 \times 10^9\,\mathrm{cm}^{-3}$ was proposed by Ripamonti & Abel (2004). They analyse the role of CIE cooling in primordial star formation analytically and use this simple approximation as a correction for the optically thick H_2 line cooling. They compare the analytic fit formula to results of previous simulations by Ripamonti et al. (2002) and find out that it reproduces the results up to densities of $n \simeq 8 \times 10^{16}\,\mathrm{cm}^{-3}$ remarkably precise if the cloud remains approximately spherical during the collapse. Their method has been applied in a lot of (mainly grid-based) simulations like O'Shea & Norman (2006); Turk et al. (2011) or Hirano & Yoshida (2013).

A second method was proposed by Greif et al. (2013) who study chemo-thermal instability in primordial star-forming clouds. The idea follows the approach by Ripamonti & Abel (2004) but with a smooth transition and therefore a continuous derivative towards the optically thin regime. The formula is given by

$$\beta = \begin{cases} \frac{1.45x}{x^{1.45}+0.45} & \text{for } x \geq 1 \\ 1 & \text{for } x < 1 \end{cases} \tag{2.21}$$

where $x = n/n_0$ and $n_0 = 4 \times 10^9\,\mathrm{cm}^{-3}$. A comparison between both fits can be seen in Figure 2.12. These fits are the easiest and most direct way to determine

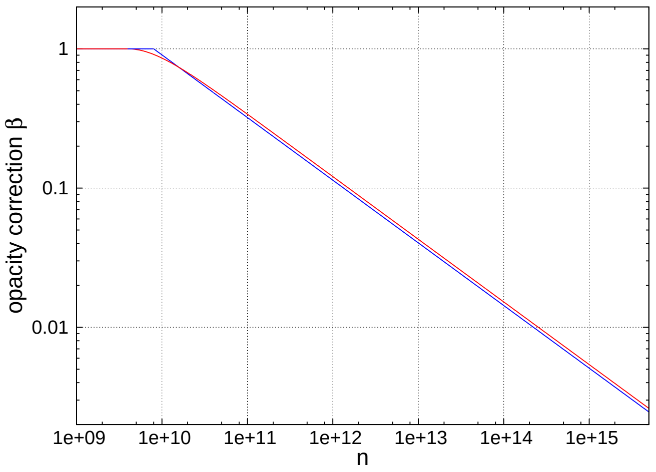

Figure 2.12: Comparison of the two fitting formulas for the opacity correction. Equation 2.20 following Ripamonti & Abel (2004) in blue and Equation 2.21 with a continuous derivative according to Greif et al. (2013) in red.

the opacity correction but their use does not account for any information about the temperature, velocity or density profiles.

3 Simulations

We study the collapse of primordial gas clouds with numerical simulations. Since we want to cover more than twelve orders of magnitude in density and time, we have to apply various numerical methods in order to tackle this problem. In this chapter we want to explain the basic concept of SPH, the code we are using, our choice of initial conditions and the different cooling approaches we want to compare.

3.1 Numerical Methods

In order to understand the basic numerical concepts and methods, we briefly present the underlying physics and the numerical implementation in the following sections.

3.1.1 Smoothed Particle Hydrodynamics (SPH)

We want to simulate the gravitational collapse of a gas cloud without following the time evolution of every single atom. Comparing it to a blob of gas, you do not have to know the complete 6N-dimensional probability distribution function to characterise it, because you can describe the gas by its temperature, pressure, and density. Hence, we can also simplify our problem by means of an approximation. In order to do so, there are generally two different approaches: the introduction of a spatial grid discretises space. Density, temperature or acceleration are then assigned to the grid cells (Eulerian point of view). Alternatively, we can discretise mass by introducing individual particles which carry information about mass, velocity and other hydrodynamic quantities (Lagrangian point of view). This second approach is the basic principle of smoothed particle hydrodynamics (SPH) which is used for the following simulations. In this section (mainly based on Landau & Lifshits 1987; Klessen 2002) we want to understand the underlying theory and the main principles and features of SPH in order to understand the simulations, results and caveats.
The time evolution of the gas is given by the four equations of hydrodynamics:

- The conservation of mass is formulated by the continuity equation

  $$\frac{\mathrm{d}\rho}{\mathrm{dt}} = \frac{\partial \rho}{\partial t} + \vec{v}(\vec{\nabla}\rho) = -\rho(\vec{\nabla}\vec{v}), \tag{3.1}$$

  where ρ is the density and $\vec{v}$ is the velocity.

- The conservation of momentum is formulated by the Navier-Stokes equation

$$\frac{\mathrm{d}\tilde{\mathrm{v}}}{\mathrm{dt}} = \frac{\partial\vec{v}}{\partial t} + (\vec{v}\vec{\nabla})\vec{v} = -\frac{\vec{\nabla}p}{\rho} - \vec{\nabla}\phi + \eta\vec{\nabla}^2\vec{v} + \left(\zeta + \frac{\eta}{3}\right)\vec{\nabla}(\vec{\nabla}\vec{v}) \tag{3.2}$$

  with the pressure p, the gravitational potential ϕ and the viscosity coefficients η and ζ.

- The energy equation formulates the conservation of energy

$$\frac{\mathrm{d}\epsilon}{\mathrm{dt}} = \frac{\partial\epsilon}{\partial t} + \vec{v}(\vec{\nabla}\epsilon) = T\frac{\mathrm{ds}}{\mathrm{dt}} - \frac{p}{\rho}(\vec{\nabla}\vec{v}), \tag{3.3}$$

  where ϵ is the energy density, T is the temperature and s is the entropy.

- The Poissons equation

$$\vec{\nabla}^2\phi = 4\pi G\rho \tag{3.4}$$

  relates the gravitational potential ϕ to the matter density.

In order to solve the hierarchically nested Maxwell-Boltzmann transport equations, we need a closure equation, where one normally uses the equation of state

$$p = K\rho^\gamma \tag{3.5}$$

with the adiabatic index γ. These five equations are the theoretical framework of hydrodynamics and further heating and cooling processes can be coupled via the ds-term in the energy equation.

In principle, we can use these equations to simulate the collapsing cloud, but since we want to use a particle representation, we have to solve one more problem. In a real gas close encounters between gas particles can be neglected with respect to the overall dynamics of the gas. However, SPH particles are more massive and close encounters might completely control the dynamics which is obviously non-physical. Therefore, one generally introduces the soothing function $W(\vec{r}, h)$ (also called "smoothing kernel"), which smears out the mass of an individual particle in a region defined by the smoothing length h. This approach was at first implemented individually by Lucy (1977) and Gingold & Monaghan (1977). The local average of a quantity is then given by

$$\langle f(\vec{r})\rangle = \int f(\vec{r}')W(\vec{r} - \vec{r}', h)\mathrm{d}^3\mathrm{r}' \tag{3.6}$$

which imposes several conditions to the smoothing function (normalization and convergence for $h \rightarrow 0$). Our simulation code uses the spherical spline kernel

$$W(r,h) = \frac{8}{\pi h^3} \begin{cases} 1 - 6\left(\frac{r}{h}\right)^2 + 6\left(\frac{r}{h}\right)^3 & \text{for} \quad 0 \leq \frac{r}{h} \leq \frac{1}{2} \\ 2\left(1 - \frac{r}{h}\right)^3 & \text{for} \quad \frac{1}{2} \leq \frac{r}{h} \leq 1 \\ 0 & \text{for} \quad \frac{r}{h} > 1 \end{cases} \tag{3.7}$$

by Monaghan & Lattanzio (1985). Clark et al. (2011b) state that this choice of the smoothing kernel tends to suppress fragmentation in unresolved regions rather than promote it, which is of interest for the later discussion. The smoothing length h is adaptively chosen in order to guarantee a constant number of 57 ± 1 neighbouring particles within one smoothing length.

3.1.2 Gadget2

We use a modified version of the cosmological simulation code Gadget2. The original code was written by Springel (2005) in order to simulate structure formation by means of smoothed particle hydrodynamics. The SPH implementation in Gadget2 conserves energy and entropy, apart from shocks where energy is injected by an artificial viscosity term.

The main challenge of gravitational N-body codes is the calculation of the gravitational force which classically scales as N^2. Gadget2 solves this problem by clustering the particles into so called "tree nodes" (see Figure 3.1) which reduces the computational effort to a $N \log N$-scaling. The general idea of the tree is to cluster all

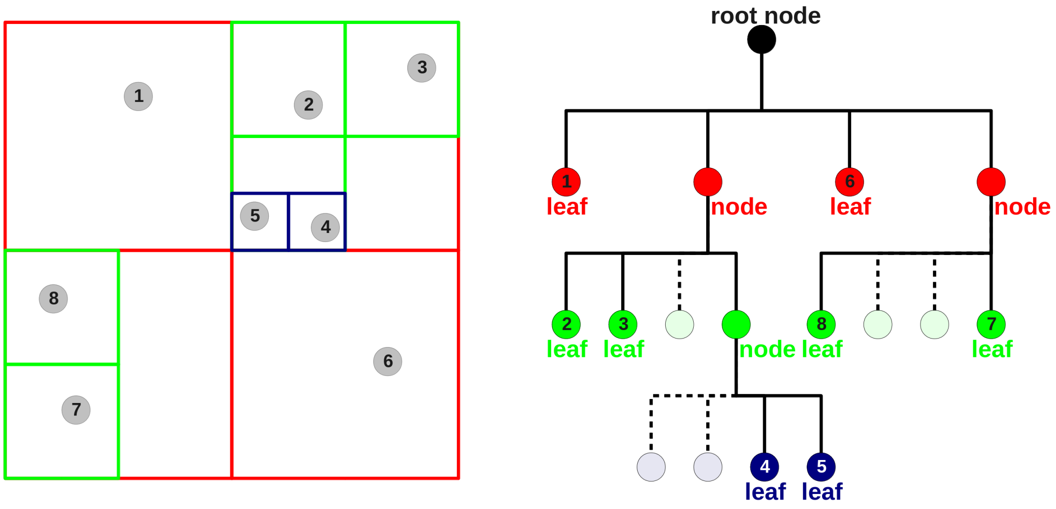

Figure 3.1: Illustration of the tree concept. The simulation volume is decomposed (left) and the particles are clustered into tree nodes (right).

particles that lie within a certain region into one tree node. Hence, we can determine the gravitational potential of the nodes rather than the individual particles. The question whether e.g. particle 4 and 5 appear close enough to be clustered or should be treated individually is obviously different for particle 2 than for particle 7. In order to quantify this clustering criterion, one can either define an opening angle (Barnes & Hut 1989) or alternatively use the condition

$$\frac{GM}{r^2}\left(\frac{l}{r}\right)^2 \leq \alpha|\vec{a}|, \tag{3.8}$$

which is implemented in Gadget2 where M is the mass of the node, l is its extension, r is its distance to the particle, $\vec{a}$ is the total acceleration acting on this particle and $\alpha \lesssim 0.01$ is a tolerance parameter. This criterion guarantees that the relative error of the gravitational force is below 1%. The domain decomposition is implemented by successively dividing each volume segment into 8 subvolumes until each volume segment contains only one particle (compare left side of Figure 3.1). The gravitational potential is then determined by "walking" the tree and summing up the contributions of the nodes or open them if the criterion (Equation 3.8) is violated.

Another important feature are adaptive timesteps. As already mentioned, we have to cover several orders of magnitude in space and time. However, there are particles in very dense, highly dynamic regions and other particles with small accelerations in slowly evolving environments. Hence, it might be extremely ineffective to use only one timestep for all particles, because this timestep has to be very small in order to capture also the highly dynamic processes. Using a small timestep for all particles results in a lot of time iterations and therefore in very long computational times. In order to minimise the number of time integrations and hence the computational effort, Gadget2 uses adaptive timesteps following the criterion

$$\Delta t \propto \frac{1}{\sqrt{|\vec{a}|}}, \tag{3.9}$$

where $\vec{a}$ is the acceleration of the last timestep. Moreover, the timesteps are a power of two subdivision of a global timestep. This restriction ensures the synchronization of particles after each global timestep in order to output data, exchange particles between processors or call the chemical network. The time evolution is calculated with a KDK-leapfrog integrator ("kick" and "drift" operators see Quinn et al. 1997) which is most stable against non-Hamiltonian perturbations.

Additionally, the timestep has to fulfil the Courant criterion (Courant et al. 1928) which guarantees that the hydrodynamical timesteps are always below any other occurring timescale. This ensures that the discretised motion of SPH particles does not suffer from rapidly propagating pressure or potential gradients.

We want to start our simulations from spherical gas clouds which are cut out from the densest regions of collapsing minihalos. However, since Gadget2 only allows vacuum or periodic boundary conditions we have to implement an additional external pressure term (Benz 1990; Clark et al. 2011a) in order to compensate for the missing gas contribution from the surrounding minihalo. Therefore, we modify the gas pressure contribution

$$\sum_j m_j \left[f_i \frac{P_i}{\rho_i^2} \vec{\nabla}_i W_{ij}(h_i) + f_j \frac{P_j}{\rho_j^2} \vec{\nabla}_i W_{ij}(h_i) \right] \tag{3.10}$$

of the momentum equation by replacing P_i and P_j with $P_i - P_{\mathrm{ext}}$ and $P_j - P_{\mathrm{ext}}$, respectively. P_{ext} is the constant external pressure and the symmetry of this equation guarantees that the pressure cancels for particles that are surrounded by other particles. Whereas at the edge of the cloud, this term does not vanish and thus mimics the pressure contribution from a surrounding medium (Clark et al. 2011a). We do not want to artificially squeeze the cloud and therefore we set the external pressure to the smallest occurring pressure in the outer 10% of the clouds.

3.1.3 Chemistry, Heating and Cooling

The assumption of an isothermal collapse with constant abundances is not valid throughout the whole star formation process. We rather have to take care of the chemical and thermal evolution of the collapsing gas cloud, solve the rate equations and couple the relevant heating and cooling terms to the hydrodynamic equations. Therefore, we use a code that is originally based on Glover et al. (2003) and was substantially modified by Simon Glover in order to model the chemistry and cooling in star formation simulations. The primordial chemistry network includes H, D, He, H_2, H^+, H^-, D^+, H_2^+, HD, He^+, He^{++} and e^-. The rate equations between these species are solved self-consistently for every timestep. The following dominating heating and cooling processes are implemented in our simulation code:

- H_2 line cooling (see section 3.1.6).

- CIE cooling: we assume fully molecular gas which is generally true for the relevant densities. The optically thin cooling rate is taken from Ripamonti & Abel (2004) and to correct for the continuum absorption at high number densities, we follow the prescription by M. Turk (2010, private communication) and Clark et al. (2011a)

  $$\Lambda_{\mathrm{CIE,thick}} = \Lambda_{\mathrm{CIE,thin}} \times \min\left[\frac{1 - \exp^{-\tau_{\mathrm{CIE}}}}{\tau_{\mathrm{CIE}}}, 1 \right], \tag{3.11}$$

  where

  $$\tau_{\mathrm{CIE}} = \left(\frac{n}{1.4 \times 10^{16}\,\mathrm{cm}^{-3}} \right)^{2.8}. \tag{3.12}$$

- H_2 three-body formation heating: binding energy of 4.48eV is released for every newly formed H_2 molecule.
- Accretion heating: the protostars accrete gas with an accretion luminosity of

  $$L_{\text{acc}} = \frac{GM_*\dot{M}}{R_*}, \tag{3.13}$$

  where $\dot{M}$ is the mass accretion rate and M_* and R_* are the mass and radius of the protostars respectively sink particles (Smith et al. 2011). We use Equation 1.48 for the radius and for the accretion rate we assume a constant value of $\dot{M} = 10^{-2} M_\odot \text{yr}^{-1}$ This is consistent with Clark et al. (2011b) and Hirano et al. (2013) and valid as we see in section 4.4.1. The heating rate is then given by

  $$\Gamma_{\text{acc}} = \rho \kappa_P \left(\frac{L_{\text{acc}}}{4\pi r^2} \right), \tag{3.14}$$

  where ρ is the gas density, κ_P is the Planck mean opacity and r is the distance from the source.

Furthermore, there are a lot of other heating and cooling processes implemented in the code like electronic excitation, recombination, photodissociation, HD-cooling, Compton cooling or Bremsstrahlung (Glover & Jappsen 2007; Clark et al. 2011a) but these processes have only minor effects in our simulations. We should note that our current implementation has no transition to equilibrium chemistry. Hence, the chemical timesteps become very short if the equilibrium for a certain species is almost reached which might even cause the code to crash if the chemical timestep becomes shorter than the dynamical timestep.

3.1.4 Sink Particles

We have already seen that star formation is a highly dynamic process which covers many orders in density. Especially in the high density regime, the dynamical timesteps become very short and therefore the computational effort extremely large. Furthermore, we have not implemented all relevant physical processes which occur in the protostar. Hence, we use so called sink particles as a computational trick to overcome these computational problems.

Our sink particle implementation is based on Jappsen et al. (2005), which was already used before e.g. in Boss & Black (1982); Boss (1987, 1989) and Bate et al. (1995). Above a certain density threshold n_{crit} all SPH particles are merged into one single sink particle, which now contains all mass and momenta of the merged particles. This approach conserves mass and momentum, avoids small dynamical timesteps and we can identify the protostars by the new formed sink particles. This critical density threshold is normally chosen to be the resolution criterion $n_{\text{crit}} = n_{\text{res}}$

(3.1.5) which guarantees the validity of the SPH approach throughout the simulation. The sink particles also have an accretion radius $r_{\rm acc}$ which is normally of the same order as the local Jeans length, representing the typical length scale that can be resolved. An existing sink particle accretes any further gas particle which comes inside the accretion radius and is bound to the system.

Nevertheless, we should keep in mind that sink particles are just a computational trick which also causes problems like a discontinuity in the mass and number of particles, a lack of pressure forces at the accretion radius and the violation of the hydrodynamic equations because the accretion onto the sink particle happens instantaneously (Greif et al. 2012). In order to minimise those shortcoming of the sink particle approach and to guarantee that the formation of a sink particle actually represents the local collapse to a protostar, there are several additional criteria to check prior to the formation of a sink particle:

- The flow should converge ($\vec{\nabla}\vec{v} < 0$).
- It should be a bound structure with a negative total energy ($E_{\rm tot} < 0$).
- The region should be Jeans unstable which is equivalent to $|E_{\rm grav}| > 2E_{\rm th}$ (Federrath et al. 2010).
- The distance to the nearest other sink particle should be at least $2r_{\rm acc}$.
- The smoothing length of the particles must be smaller than the accretion radius of the sink particle.

Federrath et al. (2010) compared sink particle implementations in AMR and SPH and confirmed that the density threshold test alone is not sufficient because shocks might lead to very dense, converging flows which are nevertheless unbound. Using these additional criteria, the accretion rates onto sink particles are in excellent agreement with theoretical predictions.

Sink particles gravitationally interact with each other and the surrounding gas. This is why they also have a smoothing length which is of the same order as the sink particle's accretion radius in our simulations. However, sink particles can merge or be dynamically ejected after close encounters (Greif et al. 2012). A close encounter might lead to a remarkable decrease in accretion rate because the sink particles can not accrete very efficiently in the outer region of the cloud, whereas a merger might lead to a shift in the mass function to higher protostellar masses. Although Greif et al. (2012) found that nearly two-thirds of the secondary protostars have merged away, we have not yet implemented this feature in our code but this might be one of the next improvements.

Another crucial value is the accretion radius $r_{\rm acc}$. While Clark et al. (2011b) found that $r_{\rm acc} = 1.5$AU and $r_{\rm acc} = 3$AU yield qualitatively the same results, Greif et al. (2011) claims that the accretion radius has an influence on the fragmentation behaviour. Furthermore Machida & Doi (2013) found that fragmentation always occurs on a scale several times larger than $r_{\rm acc}$, indicating that the sink radius artificially

yields the fragmentation scale. On the other hand, Greif et al. (2012) and Machida & Doi (2013) say that fragmentation does not occur for densities above $n \simeq 10^{17}\,\mathrm{cm}^{-3}$ ($n \simeq 10^{15}\,\mathrm{cm}^{-3}$, Smith et al. 2011) because there are no more chemical heating terms that might prevent the gas from collapsing.
Phrased differently, the choice of the accretion radius might have an influence on the fragmentation behaviour but as long as the critical density is $n_{\mathrm{crit}} \gtrsim 10^{16}\,\mathrm{cm}^{-3}$, we should capture all fragmentation of the cloud. Finally, we should keep in mind that sink particles represent protostars rather than finished Pop III stars (Smith et al. 2011) and therefore the sink mass function cannot directly be related to the IMF.

3.1.5 Resolution

As already mentioned in section 3.1.1, SPH discretises mass and therefore it should be clear that we cannot resolve any structures smaller than a single SPH particle. In our SPH implementation each particle should have $N_{\mathrm{ngb}} = 57 \pm 1$ neighbours which is the best compromise between efficiency and accuracy (P. Clark 2013, private communication). Since SPH smooths the particle properties like temperature within a certain volume, several particles (in our case 57) contribute to the temperature of a single point in space. This means that we need at least 57 SPH particles to resolve all quantities properly. Actually, the resolution criterion formulated by Bate & Burkert (1997) requires $2N_{\mathrm{ngb}} \simeq 100$ particles for a proper resolution. This resolution criterion is important in the high density regime and especially for the choice of the critical density n_{crit} and the accretion radius r_{acc} of the sinks. The smallest mass we can resolve is

$$m_{\mathrm{res}} = 100 m_{\mathrm{SPH}}, \tag{3.15}$$

where m_{SPH} is the average mass of an SPH particle. Furthermore, we want to ensure that we can resolve a Jeans mass throughout the simulation which yields

$$m_{\mathrm{res}} \leq m_J. \tag{3.16}$$

Assuming the smallest possible temperature in this density regime, we can determine the critical density at which the Jeans mass is equal to the resolution mass m_{res}. The accretion radius is then given by the Jeans length at this temperature and density.

3.1.6 Implementation of Cooling Approaches

The general idea of the different cooling approaches has already been discussed in chapter 2. In this section we want to address the actual implementation of these approaches into the code, point out some approximations, give hints for the reproduction and comment on the efficiency.
The optically thin cooling rate $\Lambda_{\mathrm{H_2},\mathrm{thin}}$ is determined based on the number density, abundances and temperature of the gas (see section 1.4.1). The optically thick

cooling rate $\Lambda_{\mathrm{H_2,thick}}$ is given by Equation 1.81, where the opacity correction β can be expressed as a function of the column density divided by the thermal velocity of the $\mathrm{H_2}$ molecules (N/v_{th}) and the temperature T. The distribution of β can be seen in Figure 3.2 and its values are stored in a lookup table for $31.6\mathrm{K} \leq T \leq 31600\mathrm{K}$ and $10^{17}\mathrm{s\ cm^{-3}} \leq N/v_{\mathrm{th}} \leq 10^{27}\mathrm{s\ cm^{-3}}$.

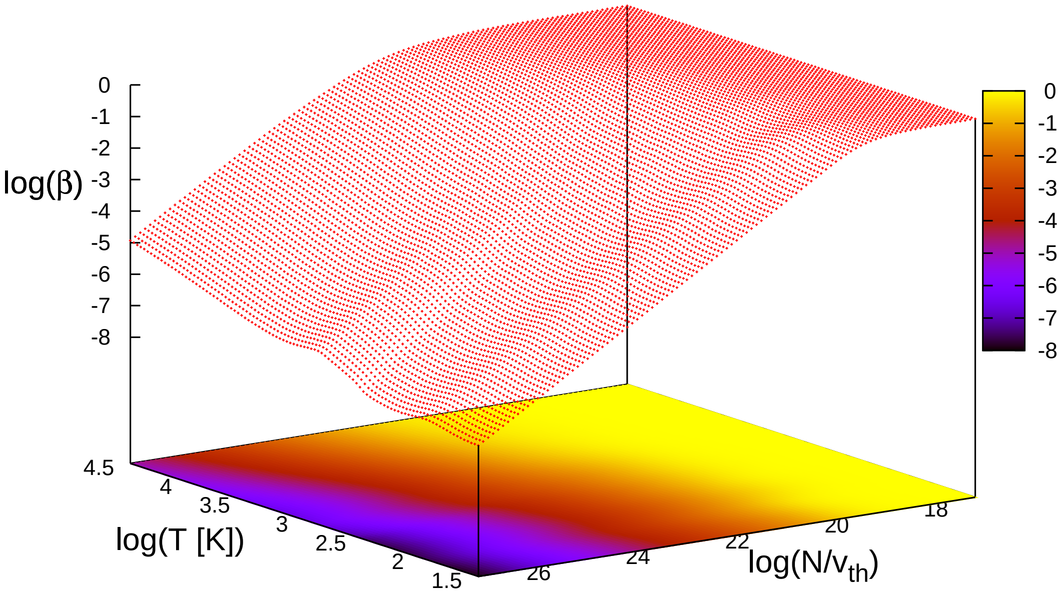

Figure 3.2: Opacity correction β as a function of temperature and column density over thermal velocity. In the code β is determined based on an interpolation of this lookup table.

For the TreeCol-based determination of the effective column densities we have to create another lookup table, which relates the relative velocities in units of the thermal velocities (v_r/v_{th}) to an overlap of spectral lines. Since the relative velocities are distributed roughly equally throughout the simulation, we created this lookup table with linear steps in velocity space. We want to avoid numerous calculations of square roots because they are computationally very expensive. Therefore, we simply look up the squared velocities because both the relative velocity $v_r = [(v_{x,i} - v_{x,j})^2 + (v_{y,i} - v_{y,j})^2 + (v_{z,i} - v_{z,j})^2]^{1/2}$ and the thermal velocity $v_{\mathrm{th}} \propto \sqrt{T}$ require the calculation of a square root which can be avoided using their squared values. For each node that might contribute to the effective column density we first check if

$$\left(\frac{v_r}{v_{\mathrm{th}}}\right)^2 \leq 43.3 \tag{3.17}$$

because otherwise the line overlap is smaller than 10^{-3} and can be neglected anyway. The computational effort of the lookup of relative overlaps is negligible small compared to the computational cost of TreeCol itself.
For the Gnedin approximation (section 2.3.1) we have to determine ∇n whose determination is not yet implemented in the code (but it should be possible following the implementation for the determination of ∇v which is already present in the code). In order to compare the results nevertheless, we approximately determine ∇n_{H_2}, L_{Gnedin} and the related opacity correction based on the density distribution in the output files. The best approximation for the density gradient of the i-th particle is

$$|\vec{\nabla} n_i| = \sum_j \frac{|n_i - n_j|}{|r_i - r_j|} W(h_{ij}), \tag{3.18}$$

where the summation is over all neighbours. Unfortunately, this approach scales as N^2 and is therefore extremely expensive because no tree structure is present in the output files. Hence, we use an approximation and assume a spherically symmetric density profile with shells of constant density that are distributed logarithmically along the radius. This approach scales as N because we just have to average the density within these spheres, determine the density gradient

$$|\vec{\nabla} n_{ij}| = \frac{|n_i - n_j|}{|r_i - r_j|} \tag{3.19}$$

between two spheres i and j and assign the corresponding density gradient to each particle. We have checked the validity of this approximation by comparing it to the more exact approach given by Equation 3.18. For typical conditions in our simulation we determine the density gradients and the associated opacity corrections with both methods and compare the results in Figure 3.3. Although the deviations between these two methods are small and therefore Equation 3.19 seems to be a valid approximation, we should keep in mind that we have to assume a spherical density profile and thus do not capture any other structures e.g. the formation of a disc. Nevertheless, we use this approximation because of the extremely high computational cost for the more exact approximation.

3.2 Initial Conditions

In our study we want to focus on the non-linear collapse of the central core rather than the linear collapse of the minihalo. Yoshida et al. (2003) examined the statistical properties of primordial star-forming clouds and compared different methods of generating cosmological initial conditions. They found out that the choice of initial conditions does not only affect the density field in the linear regime but also the properties of the non-linear collapse. Therefore, we have to create realistic initial conditions for our simulations.

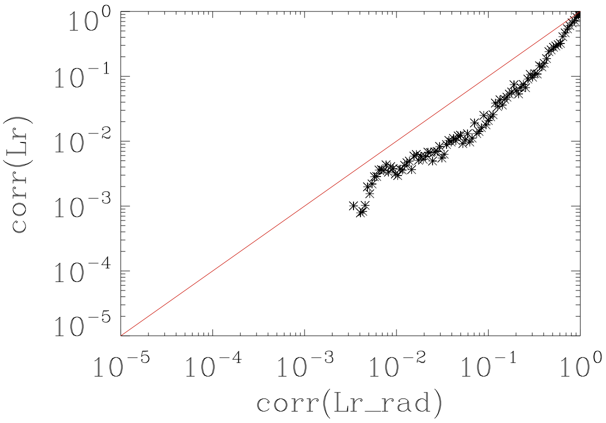

Figure 3.3: Comparison of the opacity corrections based on Equation 3.18 (Lr) and Equation 3.19 (Lr_rad). The red line indicates the desired bisectrix, on which all points should lie. Although the faster approximation overestimates the opacity correction systematically, the deviations are small.

3.2.1 Primordial Star-Forming Clouds

Due to hierarchical structure formation in the Universe, the star-forming clouds form in the centre of dark matter minihalos, decouple from it and undergo self-gravitating collapse (Yoshida et al. 2006). These decoupled gas clouds have masses between $M = 500 M_{\odot}$ (Clark et al. 2008) and $M = 1000 M_{\odot}$ (McKee & Tan 2008; Clark et al. 2011b; Hirano et al. 2013). Smaller values of around $M \simeq 200 M_{\odot}$ are also mentioned in earlier works by Abel et al. (2000); Yoshida et al. (2006) and McKee & Tan (2008). A critical number density of $n = 10^5\,\mathrm{cm}^{-3}$ is given by Abel et al. (2000) for the decoupling of the first star forming clouds. Based on these information, we desire to start our simulations from gas clouds with $M \simeq 1000 M_{\odot}$ and an average number density of $n = 10^5\,\mathrm{cm}^{-3}$.

3.2.2 Synthetic Initial Conditions

For the first test runs we create synthetic initial conditions in order to test the newly implemented cooling approaches in a reproducible but quite realistic environment. The homogeneous gas cloud should have a mass of $M = 1000 M_{\odot}$, an average number density of $n = 10^5\,\mathrm{cm}^{-3}$ and hence a radius of $R = 4.1$pc. Therefore, we randomly place $64^3 \simeq 2.6 \times 10^5$ equally massive SPH particles in a sphere and impose a turbulence field with $v_{\mathrm{rms}} = 0.4 c_s$ to mimic inhomogeneities and increase the randomness of the initial conditions. For these runs we do not include an initial solid body rotation for the homogeneous cloud. The free-fall time of this configuration is

$t_{ff} = 5 \times 10^5$yr. The initial temperature of $T = 300$K and the chemical abundances

$$x_{\mathrm{H_2}} = 10^{-3} \tag{3.20}$$
$$x_{\mathrm{H+}} = 10^{-7} \tag{3.21}$$
$$x_{\mathrm{HD}} = 3 \times 10^{-7} \tag{3.22}$$
$$x_{\mathrm{D+}} = 2.6 \times 10^{-12} \tag{3.23}$$

are chosen according to Clark et al. (2011a) (in agreement with Greif et al. 2008). The cosmological D/H ratio of 2.6×10^{-5} is adopted from Molaro (2008). The density and temperature profile of these initial conditions can be seen in Figure 3.4. Following the prescription described in section 3.1.5, the resolution mass is $m_{\mathrm{res}} = 0.38 M_\odot$ and the number density which we can resolve above $T = 300$K is $n_{\mathrm{res}} = 10^{13}\,\mathrm{cm}^{-3}$. Therefore, the critical density for the creation of sink particles is $n_{\mathrm{crit}} = 10^{13}\,\mathrm{cm}^{-3}$ with an accretion radius of $r_{\mathrm{acc}} = 22$AU.

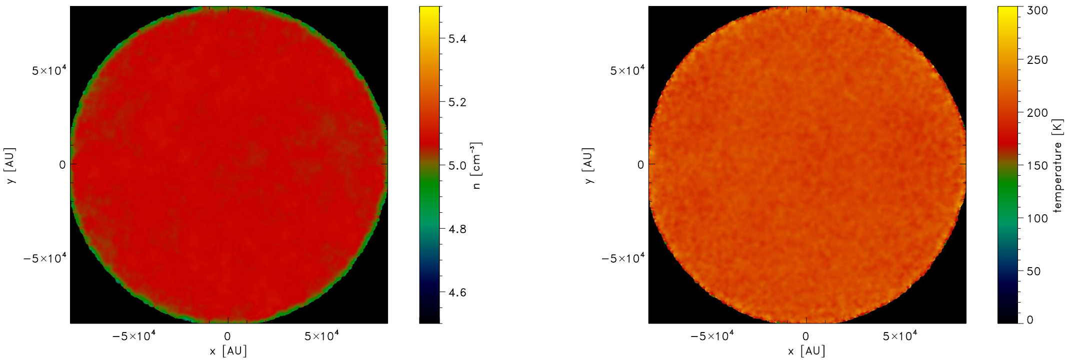

Figure 3.4: Profiles of the logarithmic number density (left) and temperature (right) for the synthetic initial cloud. Both distributions are rather homogeneous and presumably lower temperatures at the edge are artefacts due to the a posteriori applied smoothing kernel.

3.2.3 Cosmological Initial Conditions

Since we are interested in the effects of different cooling approaches in realistic star-forming regions, we create another set of initial conditions from a primordial dark matter minihalo. These data are kindly provided by Mei Sasaki who performs a cosmological structure formation simulation with the moving mesh code Arepo (Springel 2010). She uses a periodic box with 1Mpc/h side length, initialised at redshift $z = 100$. Applying several refinements of mass resolution, she follows the collapse of several density peaks into the non-linear regime. At a redshift of $z = 19.55$ she centres on the most massive minihalo and cuts out a box with a side length of 1.944pc, turns on mass refinement, which results in $N \simeq 6 \times 10^7$ SPH particles with a total mass of $M \simeq 2400 M_\odot$. In order to minimise computational effort and to reduce unintentional artefacts at the edges of the (now non-periodic) box, we cut out a sphere with radius $R = 0.5\mathrm{pc}$ centred on the centre of mass. The characteristics of this spherical star-forming cloud, which we use as initial conditions for our simulations, are as follows:

- Number of particles: $N = 1.9 \times 10^7 \simeq 268^3$
- Total mass of the cloud: $M = 1279 M_\odot$
- Radius of the cloud: $R = 0.5\mathrm{pc} \simeq 10^5\mathrm{AU}$
- Average number density: $\bar{n} \simeq 7.5 \times 10^4\,\mathrm{cm}^{-3}$
- Average temperature: $\bar{T} = 393\mathrm{K}$
- Average molecular hydrogen abundance: $x_{\mathrm{H}_2} = 1.1 \times 10^{-3}$
- Mass range of SPH particles: $1.25 \times 10^{-6} M_\odot \leq m_{\mathrm{SPH}} \leq 1.45 \times 10^{-3} M_\odot$

The actual distribution of density and temperature for these cosmological initial conditions can bee seen in Figure 3.5. In order to determine the critical density and the accretion radius of the sink particles, we should be aware of the radial mass distribution of SPH particles, which can be seen in Figure 3.6. Due to the refinement strategy, there are less massive SPH particles (and hence a better mass resolution) in the centre of the cloud. Since we expect the stars to form in the centre, we can use these central particles to define the resolution criterion and hence the critical density for sink particle formation. Therefore, we determine the resolution based on the inner 10^4AU, which contain 9.3×10^6 particles with an average mass of $\bar{m} = 1.5 \times 10^{-5} M_\odot$. The mass resolution is then given by $m_{\mathrm{res}} = 100\bar{m} = 1.5 \times 10^{-3} M_\odot$. The lowest temperature we expect in this central region is $T = 300\mathrm{K}$. We want to

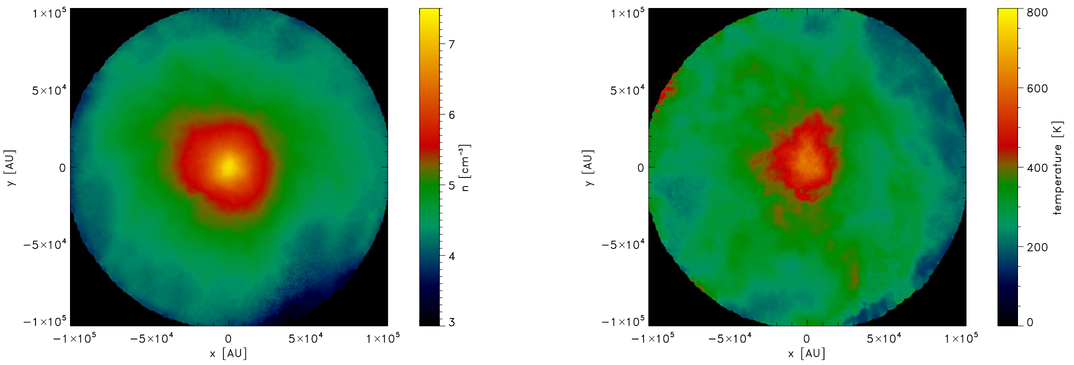

Figure 3.5: Profiles of the logarithmic number density (left) and temperature (right) for the initial cloud based on cosmological initial conditions.

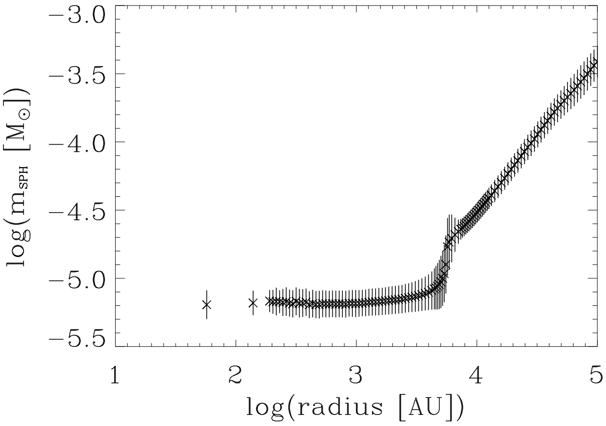

Figure 3.6: Radial profile of the SPH particles' masses with 1σ standard deviations. The data are radially binned so that each logarithmic bin contains about the same number of particles. In the inner region, the SPH particles have smaller masses and therefore we have a better resolution in the centre.

ensure $m_{\rm res} \leq m_J$ throughout the simulation. Thus, we can determine the highest number density which still satisfies this criterion to be $n_{\rm res} = 3.42 \times 10^{15}\,{\rm cm}^{-3}$. Beyond this density, we can not guarantee to resolve the local Jeans mass with at least 100 SPH particles. Therefore, the critical density for the formation of sink particles is equal to this resolution density $n_{\rm crit} = n_{\rm res} = 3.42 \times 10^{15}\,{\rm cm}^{-3}$. The resolution length scale is equal to the Jeans length which yields $\lambda_J = 0.3$AU under these conditions. Such a small accretion radius might lead to tiny dynamical timesteps in the vicinity of sink particles and hence increase the computational effort. Therefore, we set the accretion radius to $r_{\rm acc} = 3$AU, which clearly fulfils the resolution criterion.

Due to the huge amount of data, we implemented a small change in the output routine of the code which increases speed and minimises memory requirements. One normal snapshot of these runs contains all information about position, velocity, density, temperature, chemical abundances, cooling and heating rates, smoothing lengths, and the column densities for each particle. This is why a normal snapshots has a size of 40GB. A main part of this memory is used for the column densities because for every particle the values for each of the 48 HEALPix pixels for H, H_2 and CO are stored. In order to minimise this effort, we only store the effective column density of H_2 (logarithmically averaged over all HEALPix pixels) for each particle. Using this simplification, we reduce the size of one snapshot to 2GB and therefore increase the time resolution of our analysis by decreasing the output intervals.

4 Results

In this chapter we want to present the results of our simulations. First, we analyse the TreeCol-based cooling approaches and compare them to the other cooling implementations. Furthermore, we want to analyse the collapse of the cloud, its fragmentation behaviour and finally estimate the primordial IMF, based on the cosmological initial conditions.

4.1 Validity of TreeCol-Based Cooling Approaches

We presented three methods to determine the column density which are based on TreeCol (section 2.2.2). In a first check we want to verify if these methods actually work and whether they reproduce the Sobolev-like estimations for the column density or if they yield significantly different results. Therefore, we run 5 individual simulations, each with a different cooling approach (summarised in Table 4.1). In order to judge if differences between these methods are random effects and might vary from cloud to cloud or if differences are systematic trends, which might occur in all primordial clouds, we create two realizations of the synthetic initial conditions. Both realizations have the same global properties (mass, radius, temperature, chemical composition) but differ in the random initial positions of the SPH particles and in the random seed for the turbulence field generation.

	L_S	$1.694 L_\mathrm{S}$	exact overlap
local density	*off*	*off_corr*	-
TreeCol	*on*	*mean*	*lookup*

Table 4.1: Overview and nomenclature of the five cooling approaches used for the synthetic initial conditions. The Sobolev (“off”) and corrected Sobolev approach (“off_corr”) are based on local quantities (and TreeCol is switched off), whereas the TreeCol-based methods directly sum up the mass contributions for the column density.

The general structure of the collapse can be seen in Figure 4.1. All five methods reproduce the typical $n \propto r^{-2.2}$ slope for primordial clouds (compare Equation 1.43) and differ only slightly in the high density regime. The H_2 column densities as a function of density can be seen in Figure 4.2 for different times of the collapse. Generally, the Sobolev-based methods overestimate the effective column density in the optically thick regime. The systematic discrepancies between the Sobolev- and TreeCol-based methods differ by up to a factor of one hundred. For one and the

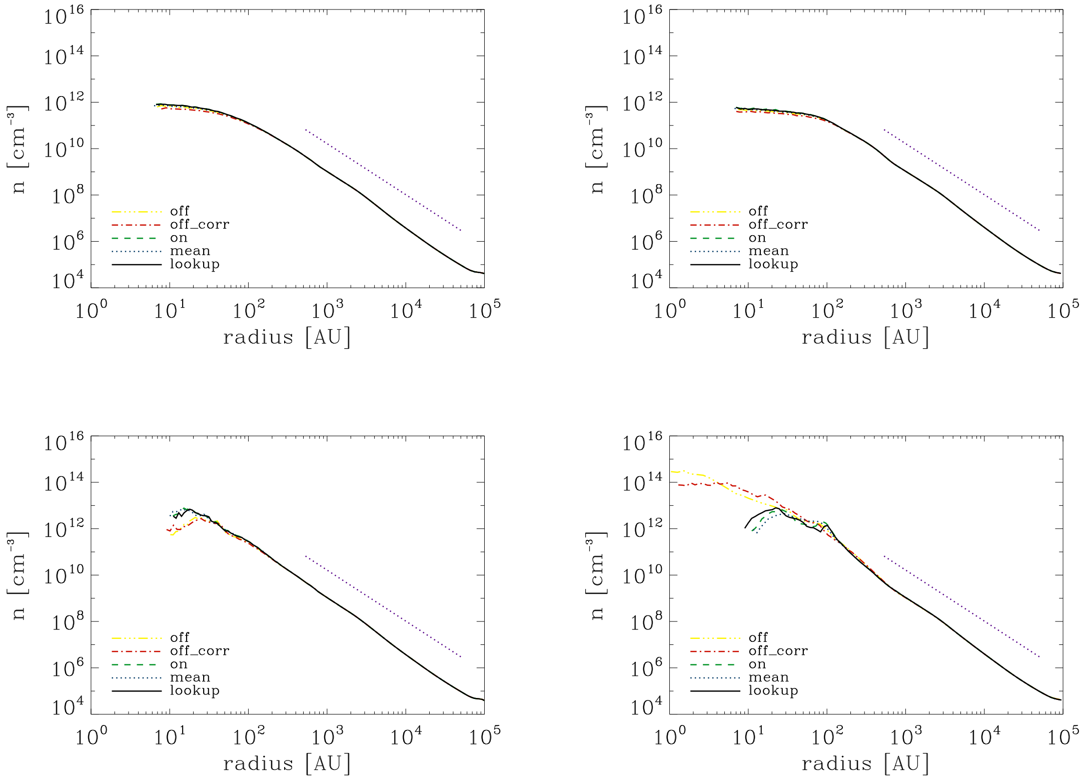

Figure 4.1: Radial density profiles of the clouds for different cooling approaches. The snapshots are taken before (top) and after (bottom) formation of the first sink particle for two different realizations (left and right) of the synthetic initial conditions. There are no significant differences or trends for the cooling approaches. The typical $n \propto r^{-2.2}$ slope (illustrated by the purple dotted line) is reproduced by all methods.

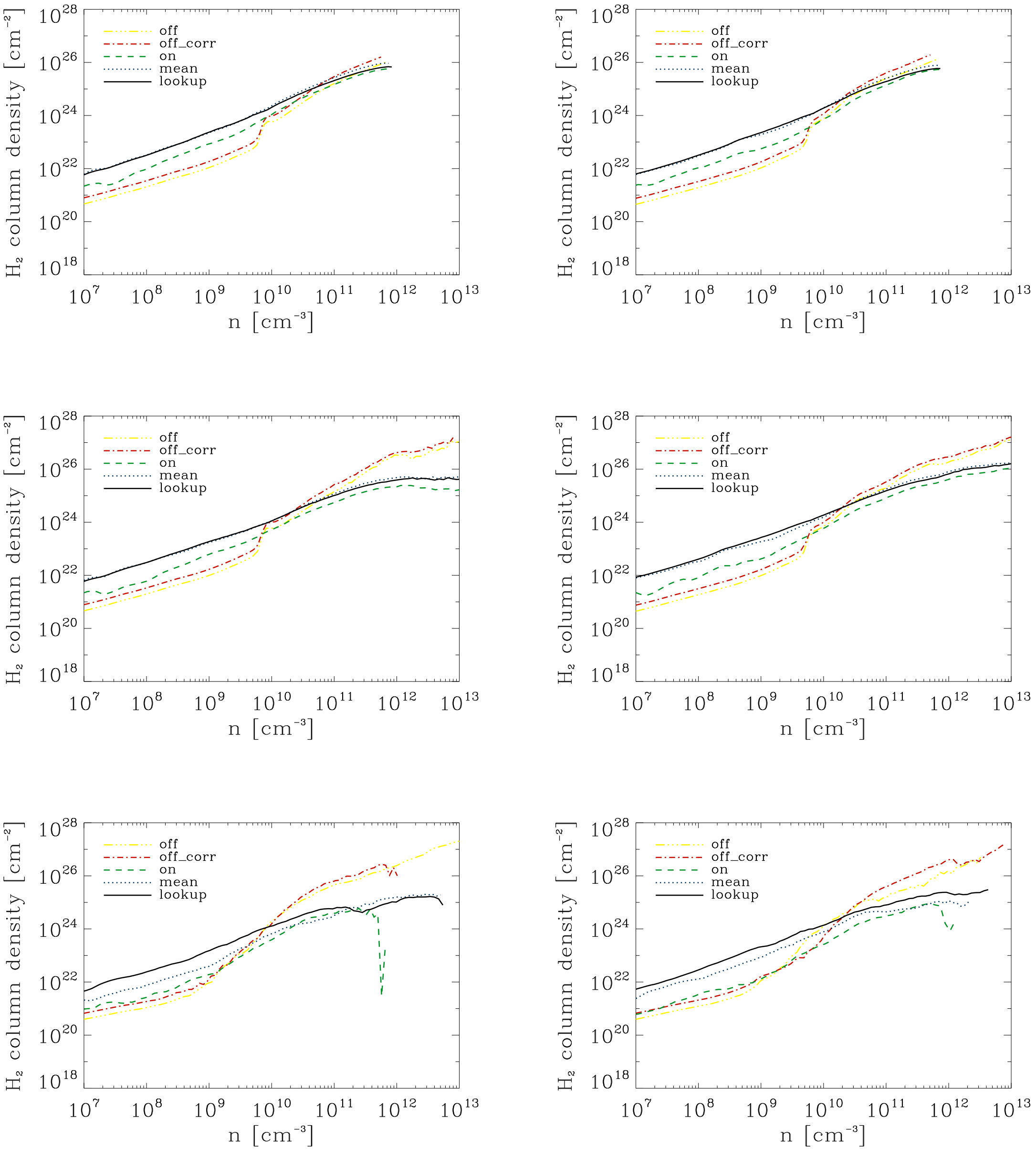

Figure 4.2: H_2 column density as a function of density for different cooling approaches. The snapshots are taken before formation of the first sink particle (top), after formation of the first sink particle (middle) and at the end of the simulation (bottom) for two different realizations (left and right) of the synthetic initial conditions. In the relevant high density regime, the Sobolev-based methods overestimate the column densities by up to two orders of magnitude. For all plots and density regimes, "mean" seems to fit lookup best, which we expect to be the most exact method.

same configuration we generally expect the corrected Sobolev method to yield higher column densities than the uncorrected version. However, since we are dealing with different dynamical properties in different simulations, this trend does not have to be present all the time.

Realizing that the Sobolev approximation already overestimates column densities, one might ask why we need this additional correction factor, which even worsens the approximation. A detailed answer to this question is given in section 5.1 but we already want to emphasise the total neglect of any density gradient. The Sobolev approximation assumes a constant density, but the density of molecular hydrogen generally decreases when moving radially outwards. Hence, this approximation is not valid, but leads to an overestimation of the column density (already for the uncorrected Sobolev method). However, we can justify the correction factor by a comparison of the TreeCol-based methods. The lookup approach explicitly accounts for the true line overlaps and therefore is the most exact method. While "mean" accounts for the correction factor and fits lookup remarkably precise in almost all cases, "on" corresponds to the uncorrected Sobolev method and generally underestimates the effective column density. Consequently, we need this correction factor to account for the exact overlaps.

The H_2 column density is directly related to the H_2 opacity correction. Its dependency on density can be seen in Figure 4.3 for the 5 different methods. Since the Sobolev-based methods overestimate the column density, they underestimate the H_2 opacity correction. Smaller values of the opacity correction mimic a higher opacity for the photons and therefore suppress efficient cooling. Moreover, we see the same trend as above, namely that "mean" fits lookup best, which demonstrates once more the need of the newly introduced correction factor. Another interesting effect is the increasing discrepancies between the methods with time. While the Sobolev-based methods suppress almost all cooling because of very high opacities at late stages of the collapse, the TreeCol-based methods yield correction factors close to one. This development of the correction factor for the TreeCol-based methods might be explained by the formation of a disc-like structure and the increased photon escape fraction perpendicular to the disc (see section 5.1.4). The discy structure can be captures by the TreeCol-based methods but is missed by the Sobolev methods which depend only on local quantities and hence cannot reflect the structure of the collapse completely.

The discrepancies in the opacity corrections yield different temperature profiles of the clouds which can be seen in Figure 4.4. As already mentioned before, the Sobolev-based methods prevent efficient cooling in the centre of the cloud and therefore the temperature is generally higher. Whereas the runs with TreeCol-based methods yield central temperatures which are lower by several hundred Kelvin. These differences in the cooling efficiency and temperature profile have effects on the fragmentation behaviour as we see in section 4.3.

Finally, we can conclude four important findings of this first analysis:

1. The TreeCol-based methods work and systematically yield smaller column

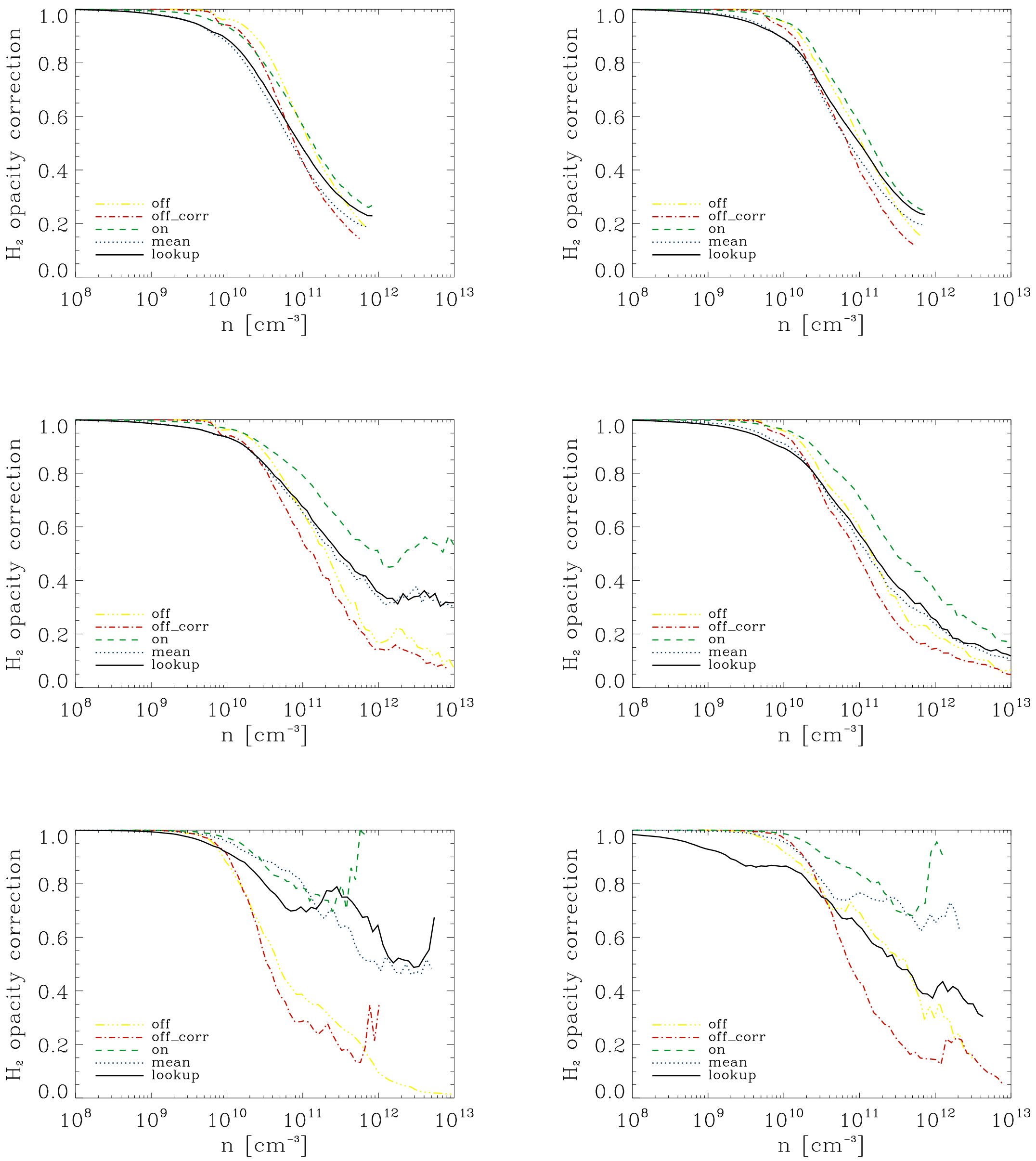

Figure 4.3: H$_2$ opacity correction as a function of density for different cooling approaches. The snapshots are taken before formation of the first sink particle (top), after formation of the first sink particle (middle) and at the end of the simulation (bottom) for two different realizations (left and right) of the synthetic initial conditions. The Sobolev-based methods clearly underestimate the opacity correction (actually they overestimate its necessity) throughout the collapse. Especially at the end of the simulation, the Sobolev-based and TreeCol-based methods differ strongly, which might be explained by the formation of a disc (see section 5.1.4). We expect the lookup approach to be the most exact one, which seems to be fitted best by the “mean” method.

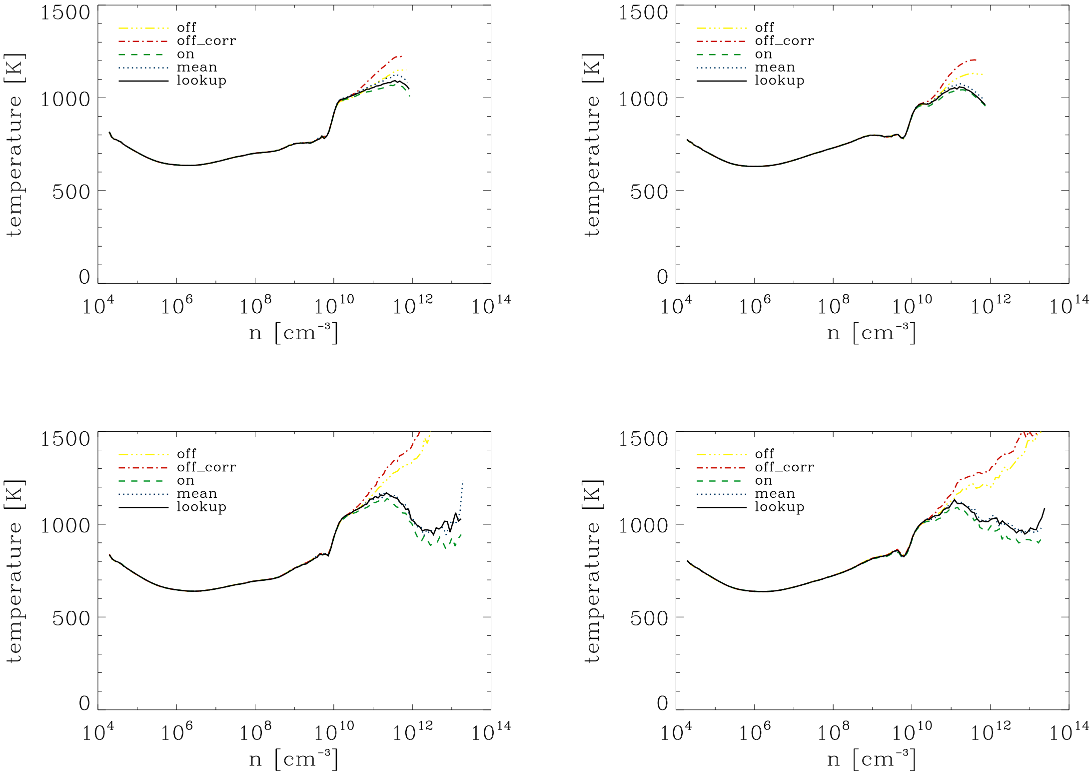

Figure 4.4: Temperature as a function of density for different cooling approaches. The snapshots are taken before (top) and after (bottom) formation of the first sink particle for two different realizations (left and right) of the synthetic initial conditions. In the high density regime, the Sobolev-based methods yield higher temperatures.

densities in the optically thick regime.

2. The correction factor is necessary although it worsens the Sobolev approximation (which can be explained by the neglected density gradient).

3. The lookup method comes with almost no additional computational effort. This is why we only use this method as a reference for further studies.

4. We expect lower temperatures in the centre of collapsing minihalos than previously expected based on the Sobolev approximation.

4.2 Comparison of Cooling Approaches

After identifying the lookup method to be the most accurate approximation for the determination of effective column densities, we can compare other approaches to this method. Therefore, we set up two simulations based on the same cosmological initial conditions (section 3.2.3). One time we apply the commonly used Sobolev approximation and one time we use the lookup approach. We run both simulations independently so that they start identically, but differ when entering the optically thick regime. Hence, we can compare the dynamical differences of the collapse and the fragmentation properties imposed by the two cooling approaches. However, in this section we compare the individual cooling approaches and are not yet interested in the fragmentation behaviour of the clouds. Therefore, we only use the lookup simulation and determine all relevant information based on its output files. By doing so, we can focus on the actual intrinsic differences of the methods (determined under the same physical conditions) rather than comparing different simulations with presumably different dynamical profiles.
Using an accretion radius of $r_{\mathrm{acc}} = 3\mathrm{AU}$ forces the simulation to crash quite early, when the most massive sink particle has a mass of $M \simeq 1.6 M_{\odot}$. In order to avoid an early crash of the code due to a small chemical timestep, we set up a second set of simulations with a larger accretion radius of $r_{\mathrm{acc}} = 20\mathrm{AU}$. Hence, we guarantee to capture the collapse and the formation of the first sink particles with a high spatial resolution, whereas the long-term behaviour of the cloud and subsequent sink formation can be studied as long as possible. We do not explicitly distinguish between the two runs in this section, because the accretion radius has no direct influence on the cooling approaches.
The first direct outcome of the different methods is obviously the column density. Since we want to find an accurate cooling approach that reproduces the lookup method best, we compare the commonly used Sobolev approximation with the approach proposed by Gnedin and our new reciprocal method, which combines Sobolev and Gnedin. The column density for these different approaches can be seen in Figure 4.5. Generally, the local methods overestimate the effective column density in the optically thick regime ($n \gtrsim 10^9\,\mathrm{cm}^{-3}$). Especially at later stages of the collapse these differences increase, because the slope of the lookup method flattens with time

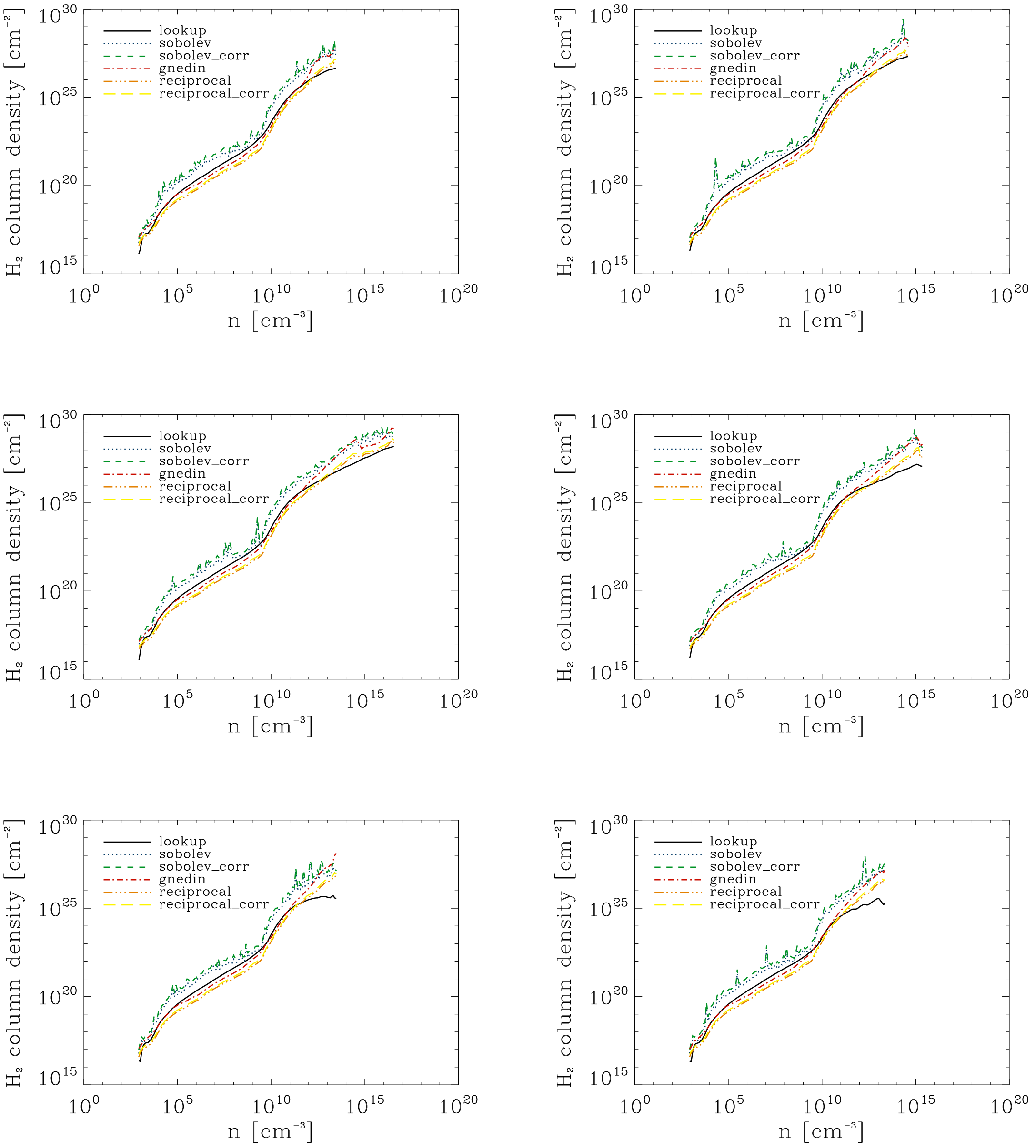

Figure 4.5: Effective column density as a function of density for different cooling approaches. The snapshots are taken at different times of the collapse (from top left to bottom right): $n_{\max} = 3 \times 10^{13}\,\mathrm{cm}^{-3}$, $n_{\max} = 3 \times 10^{14}\,\mathrm{cm}^{-3}$, $m_{\mathrm{sinks}} = 0.2 M_\odot$, $m_{\mathrm{sinks}} = 1.6 M_\odot$, $m_{\mathrm{sinks}} = 5 M_\odot$ and $m_{\mathrm{sinks}} = 10 M_\odot$. “reciprocal” represents the reciprocal sum of the Gnedin and the uncorrected Sobolev length, whereas “reciprocal_corr” uses the corrected Sobolev length. The solid black line indicates the lookup approach which should be fitted by the other methods. In the optically thick regime ($n \gtrsim 10^9\,\mathrm{cm}^{-3}$) almost all methods overestimate the column density (up to two orders of magnitude). Especially after formation of the first protostars, the lookup column density decreases with time in the optically thick regime, which is not reproduced by the local approaches.

in the optically thick regime. This noteworthy decrease of effective column density might be explained by the formation of a disc (see section 5.1.4) and the enhanced photon escape fraction perpendicular to it. The (corrected) Sobolev method overestimates the column density all the time whereas the Gnedin and reciprocal approaches overestimate the column density only for high number densities. The latter yield apparently accurate fits for the density regime $10^9\,\mathrm{cm}^{-3} \lesssim n \lesssim 10^{12}\,\mathrm{cm}^{-3}$, whereby one should keep in mind that the relative importance of H_2 line cooling decreases above $n \simeq 10^{13}\,\mathrm{cm}^{-3}$. A quantitative analysis of these results is given below.

The opacity correction as a function of density can be seen in Figure 4.6 for different methods. Although there are slight differences between the individual approaches, all methods seem to fit the lookup approach (around formation of the first sink particles) quite precise. At later stages, the lookup approach yields higher values for the opacity correction, corresponding to a smaller effective opacity of the cloud. The other methods, which depend only on local quantities, can not reproduce this behaviour and therefore underestimate the opacity correction. At the end of the simulation (total mass in sink particles of $m_{\mathrm{sinks}} = 10 M_\odot$), the cloud appears almost optically thin to the H_2 photons which can be explained by the formation of a disc-like structure so that the photons can escape perpendicularly to the disc. The relative H_2 cooling rate $(\Lambda_{H_2}/(\Lambda_{H_2} + \Lambda_{\mathrm{CIE}}))$ is shown by the purple dotted line and indicates the relevance of an accurate opacity correction.

Furthermore we compare the accuracy of the analytical fit formulas to the lookup method. Therefore, we parametrise the two fitting functions (section 2.3.5) according to

$$\beta_{\mathrm{RA}}(n) = \min\left[1, (n/n_{\mathrm{RA}})^{-b_{\mathrm{RA}}}\right] \tag{4.1}$$

and

$$\beta_{\mathrm{G}}(n) = \begin{cases} \frac{(1+b_{\mathrm{G}})x}{x^{(1+b_{\mathrm{G}})}+b_{\mathrm{G}}} & \text{for}\, x \geq 1 \\ 1 & \text{for}\, x < 1 \end{cases} \tag{4.2}$$

with $x = n/n_{\mathrm{G}}$ and the fit parameters n_{RA}, b_{RA}, n_{G} and b_{G}. In Figure 4.7 we see the original functions and the best fits to the lookup method. The newly adjusted fits minimise the weighted scatter sum

$$\sum_{i=1}^{N_{\mathrm{SPH}}} \frac{|\beta_{\mathrm{analytic}}(i) - \beta_{\mathrm{lookup}}(i)|}{\beta_{\mathrm{lookup}}(i)} \cdot \frac{\Lambda_{H_2}(i)}{\Lambda_{H_2}(i) + \Lambda_{\mathrm{CIE}}(i)}, \tag{4.3}$$

where N_{SPH} is the number of particles, $\beta_{\mathrm{analytic}}(i)$ is the analytic fit, $\beta_{\mathrm{lookup}}(i)$ is the opacity correction based on the lookup approach, $\Lambda_{H_2}(i)$ is the H_2 cooling rate and $\Lambda_{\mathrm{CIE}}(i)$ is the CIE cooling rate for the i-th particle, respectively. The weighting by the relative cooling rate accounts for the decreasing relevance of H_2 cooling at higher densities.

For each single snapshot, the exact data can be fitted remarkable exact by an an-

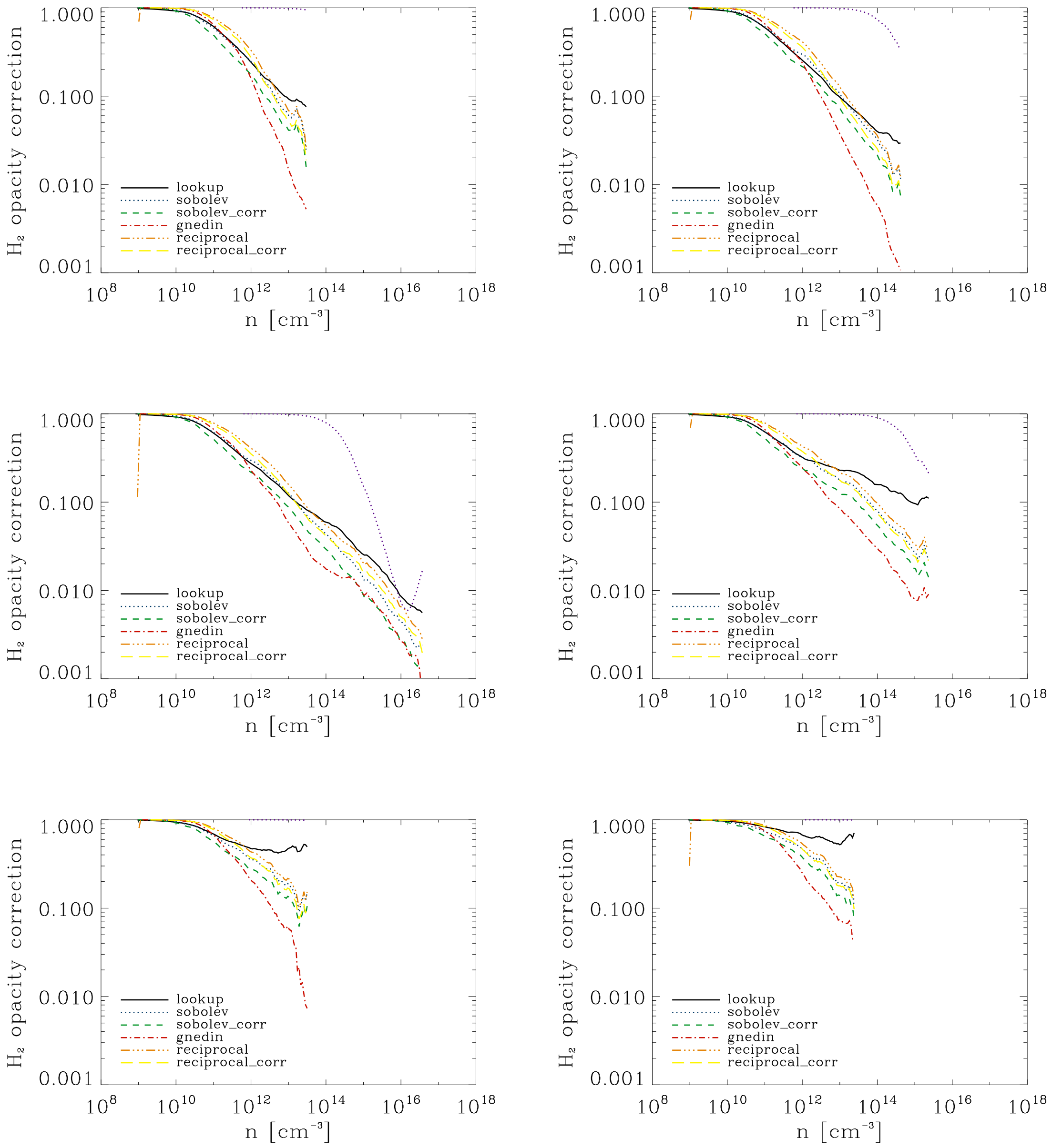

Figure 4.6: Opacity correction as a function of density for different cooling approaches. The snapshots are taken at different times of the collapse (from top left to bottom right): $n_{\text{max}} = 3 \times 10^{13}\,\text{cm}^{-3}$, $n_{\text{max}} = 3 \times 10^{14}\,\text{cm}^{-3}$, $m_{\text{sinks}} = 0.2M_\odot$, $m_{\text{sinks}} = 1.6M_\odot$, $m_{\text{sinks}} = 5M_\odot$ and $m_{\text{sinks}} = 10M_\odot$. The solid black line indicates the lookup approach which should be fitted by the other methods and the purple dotted line illustrates the relative strength of H_2 cooling. While at the beginning all methods fit the lookup data quite precise, the slope of lookup flattens for later stages and the other methods can not reproduce this feature. A quantitative analysis is given below.

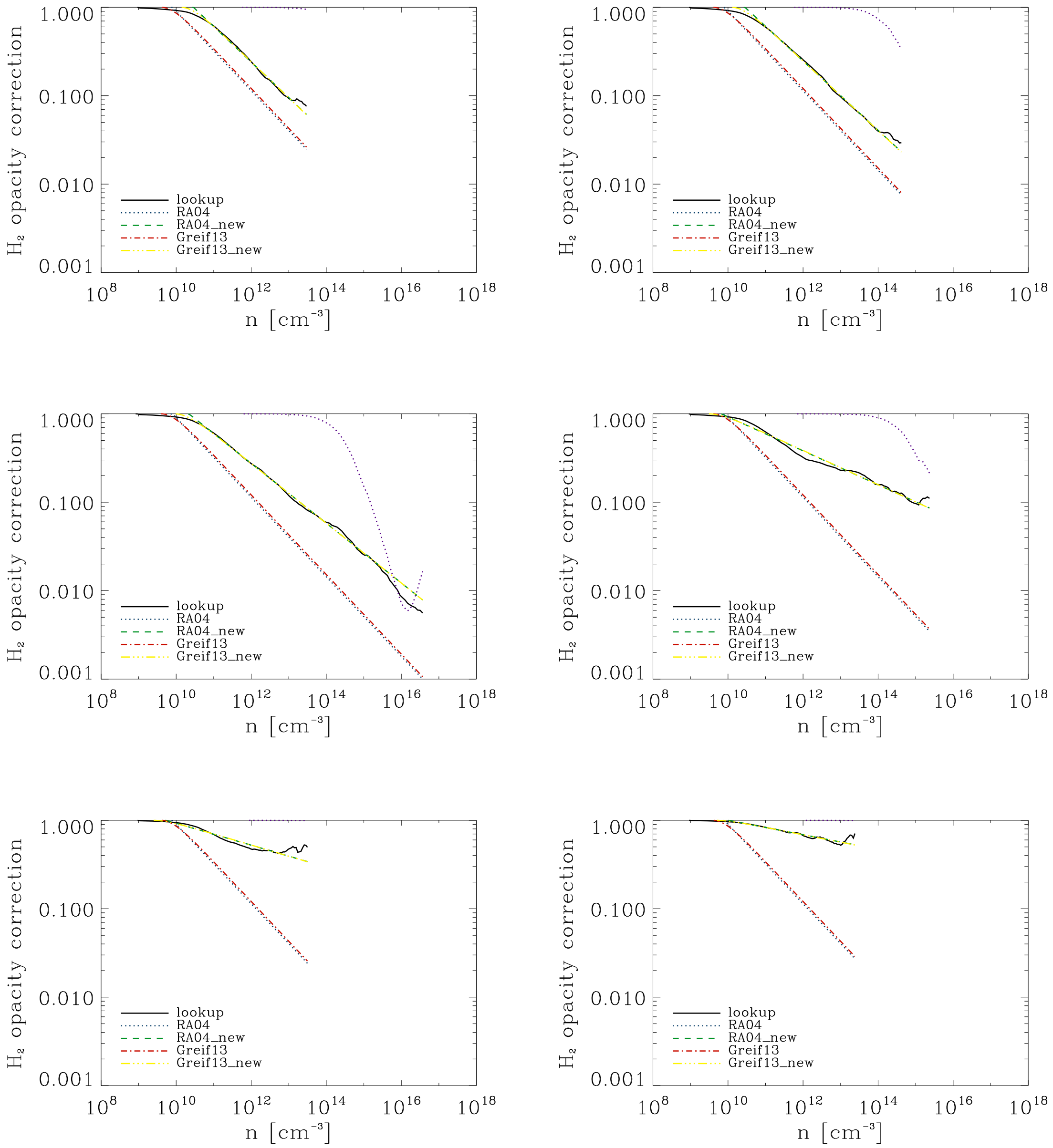

Figure 4.7: Opacity correction as a function of density for the two analytical fit formulas (the purple dotted line shows the relative strength of H$_2$ cooling). The snapshots are taken at different times of the collapse (from top left to bottom right): $n_{\mathrm{max}} = 3 \times 10^{13}\,\mathrm{cm}^{-3}$, $n_{\mathrm{max}} = 3 \times 10^{14}\,\mathrm{cm}^{-3}$, $m_{\mathrm{sinks}} = 0.2 M_{\odot}$, $m_{\mathrm{sinks}} = 1.6 M_{\odot}$, $m_{\mathrm{sinks}} = 5 M_{\odot}$ and $m_{\mathrm{sinks}} = 10 M_{\odot}$. The solid black line indicates the lookup approach which should be fitted by the analytic formulas. The blue and red line represent the original fits, whereas the yellow and green line represent the fits adjusted to the lookup method. For each time, the data can generally be fitted by an analytic function. However, the fit parameters change dramatically during the collapse.

alytic formula. However, the slope and therefore both fit parameters vary strongly during the collapse. Whereas the original fits are a satisfying approximation at the beginning of the collapse, their accuracy decreases during the collapse and they totally miss the true opacity corrections at later stages.

The time evolution of the slope might reveal an interesting insight in the structure of the collapse. In Figure 4.8 we compare the time evolution of the fit parameters b for both fit formulas. The parameter b quantifies the slope and therefore represents the dependence of the opacity on density. For large b and a steep slope, the cloud becomes opaque with increasing density very promptly, whereas for small b and a shallow slope the opacity remains low although the density increases. The blue dashed line illustrates the original slope for both fits of $b = 0.45$, but the newly fitted formulas to the lookup data reveal that the actual slope is shallower and most notably varies with time. The shallow slope for $t < 200$yr is caused by the fact that there are almost no particles in the optically thick regime, which might define the slope. Whereas the shallow slope of $b \simeq 0.1$ at later stages of the collapse might be related to a flattening of the cloud. Furthermore, a disc-like structure might increase the effective opacity correction at higher densities. Hence, it might be impossible to find one single analytical fit, which describes the dynamics of the collapse completely.

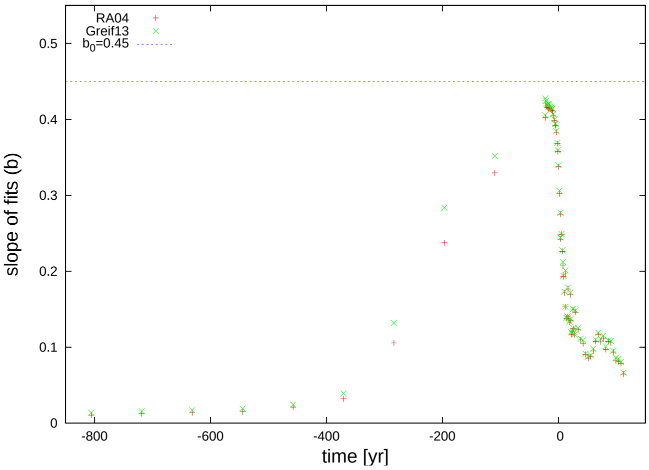

Figure 4.8: Time evolution of the fit parameters b_{RA} (Equation 4.1) and b_{G} (Equation 4.2) to the lookup data (formation of the first sink particle at $t = 0$). The blue dashed line illustrates the original slope of the fits ($b = 0.45$). This plot is intended to show the impossibility of one global fit function rather than to assign individual fitting parameters to different times of the collapse.

In order to analyse the accuracy of the different cooling approaches quantitatively, we determine the relative error of the opacity correction. Therefore, we compare the opacity corrections of all particles above a certain density threshold to the ones determined with the lookup method. The density threshold is necessary, because below $n = 10^9\,\mathrm{cm}^{-3}$, the opacity correction is very close to one anyway and hence there are no significant deviations between the methods. The relative error

$$\frac{|\beta_{\mathrm{method}} - \beta_{\mathrm{lookup}}|}{\beta_{\mathrm{lookup}}} \tag{4.4}$$

is weighted by the relative H_2 cooling rate $(\Lambda_{\mathrm{H_2}}/(\Lambda_{\mathrm{H_2}} + \Lambda_{\mathrm{CIE}}))$, so that the mean relative opacity correction error can be expressed as

$$\overline{\Delta\beta} = \frac{1}{N_{\mathrm{thresh}}} \sum_{i=1}^{N_{\mathrm{thresh}}} \frac{|\beta_{\mathrm{method}}(i) - \beta_{\mathrm{lookup}}(i)|}{\beta_{\mathrm{lookup}}(i)} \cdot \frac{\Lambda_{\mathrm{H_2}}(i)}{\Lambda_{\mathrm{H_2}}(i) + \Lambda_{\mathrm{CIE}}(i)}, \tag{4.5}$$

where N_{thresh} is the number of particles above a certain density threshold. We chose the density thresholds $10^9\,\mathrm{cm}^{-3}, 10^{10}\,\mathrm{cm}^{-3}$ and $10^{11}\,\mathrm{cm}^{-3}$, so that we can compare how accurate the methods are in a specific density regime. Below $10^9\,\mathrm{cm}^{-3}$ the opacities are still in the optically thin regime and above $\sim 10^{12}\,\mathrm{cm}^{-3}$ the number of particles is negligibly small, so that they do not contribute significantly to the overall cooling. Since we combine the available data from the simulations with the small and the large accretion radius, there are multiple data points for some times of the collapse. This might cause a small offset around formation of the first sink particle but thereby we guarantee to capture the whole collapse with the best possible time resolution. The time evolution of the mean relative opacity correction error for the threshold $10^9\,\mathrm{cm}^{-3}$ can be seen in Figure 4.9.

The relative error is very small at early times of the collapse because all opacity corrections are close to one anyway. Whereas at later times, more particles enter the optically thick regime and the relative errors rise to values between $5-30\%$. For a better clarity we split the data into two plots, one contains the most promising methods (Sobolev, corrected Sobolev, Gnedin, reciprocal and corrected reciprocal) with relatively small errors and the other plot contains the method based on the Jeans length, the method used in Gadget2 and the two analytical fit formulas with their original slopes. The Jeans approximation is the most inaccurate approach, whereas the method that is originally used in Gadget2 yields quite good results with errors between $5-15\%$. The analytical fits are comparatively inaccurate with errors around 20%, however the analytical fit function proposed by Greif et al. (2013) yield somewhat better results than the one proposed by Ripamonti & Abel (2004). The Sobolev and Gnedin approximations yield errors around 10% throughout the simulation, whereas the Gnedin approach is the best method around formation of the first sink particle. Interestingly, the corrected Sobolev approach is more accurate (compared to the uncorrected one) before formation of the first sink particle, whereas this reverses after formation of the first sink particle. The reciprocal approaches seem to be the most accurate methods for the long time evolution with errors below 5% at later stages of the collapse. The same plots for a density threshold of $n > 10^{10}\,\mathrm{cm}^{-3}$ can be seen in Figure 4.10.

Basically we observe similar results as above but the mean relative errors are higher. Whereas the analytical fits yield errors between $30-40\%$ in the relevant regime

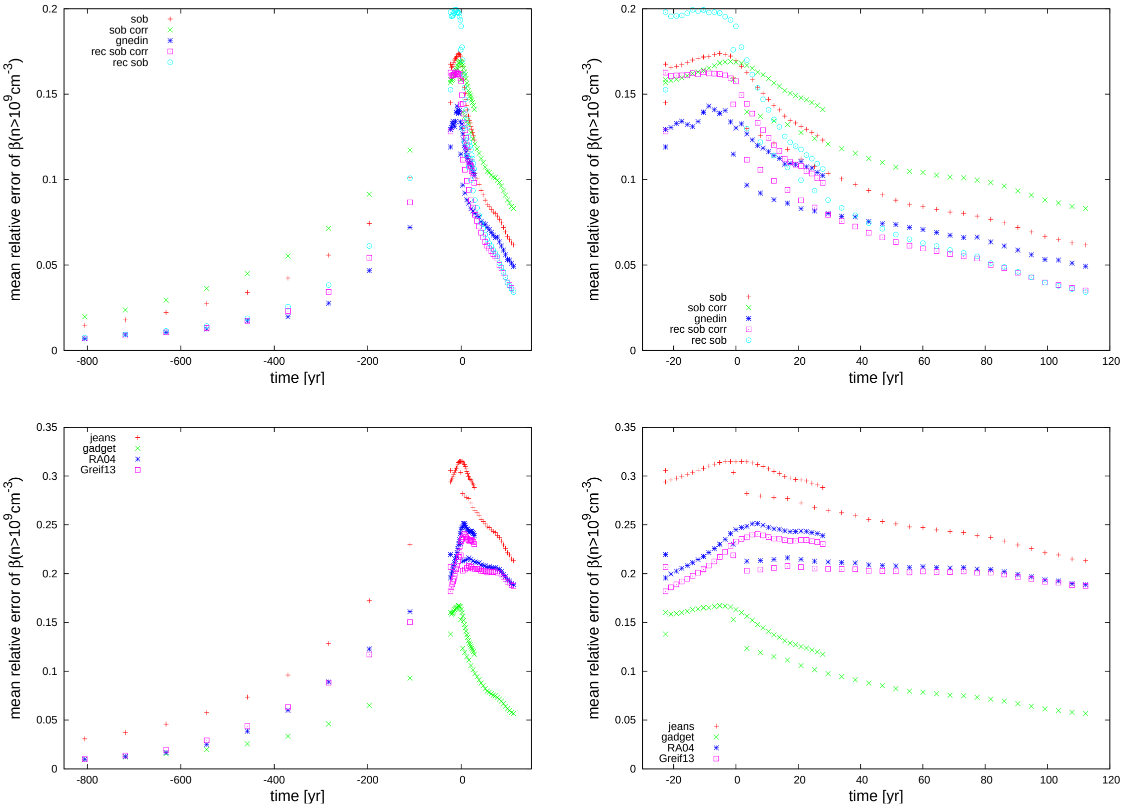

Figure 4.9: Mean relative error of the opacity correction for different methods as a function of time (at $t = 0$ the first sink particle form) for all particles above $n > 10^9\,\mathrm{cm}^{-3}$ (selection of most promising methods at the top, other methods at the bottom). At early times all opacity corrections are close to one and thus their mean error is very small. Whereas at later stages the relative error is between $5 - 30\%$ and the accuracy of the individual methods differ significantly.

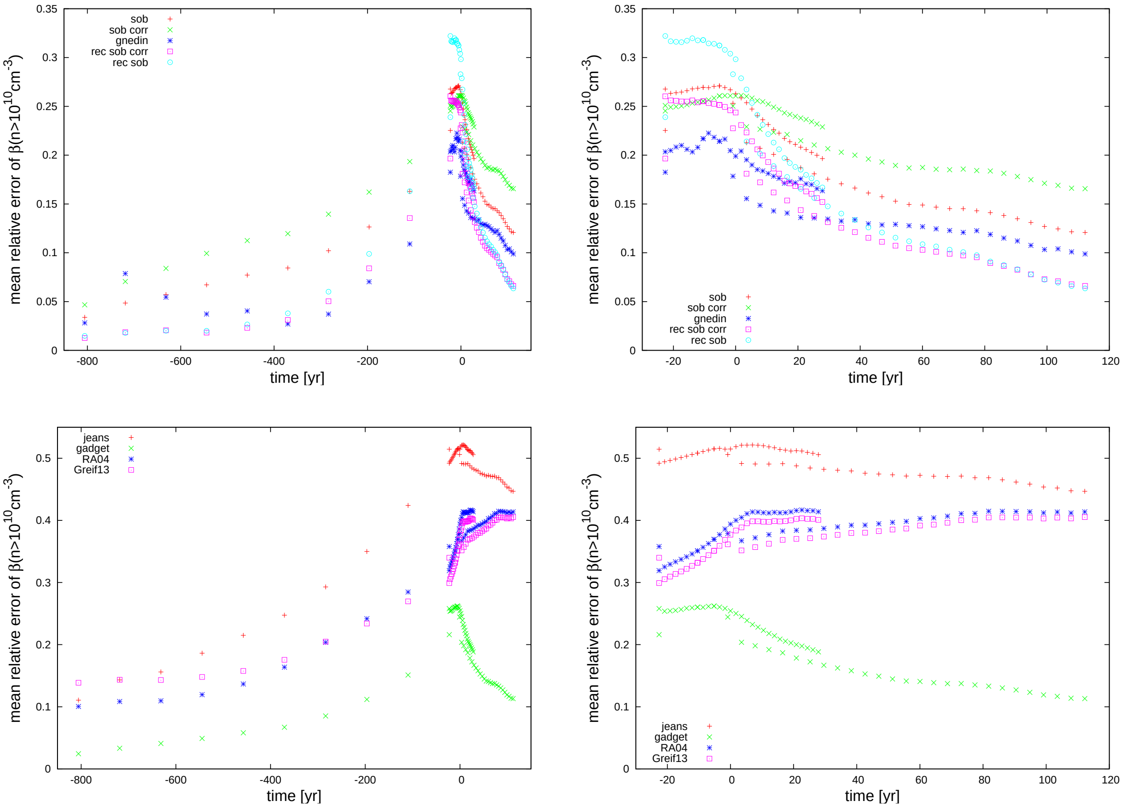

Figure 4.10: Mean relative error of the opacity correction for different methods as a function of time (at $t = 0$ the first sink particle form) for all particles above $n > 10^{10}\,\mathrm{cm}^{-3}$ (selection of most promising methods at the top, other methods at the bottom). At early times all opacity corrections are close to one and thus their mean error is very small. Whereas at later stages the relative error is between $5 - 50\%$ and the accuracy of the individual methods differ significantly.

(Greif13 slightly smaller errors than RA04), the Jeans approximation yield errors around 50%. The method used in Gadget2 as well as the Gnedin and Sobolev approximations have mean relative errors between $10 - 30\%$. Around formation of the first sink particle, the errors for the reciprocal approaches are above 20% but they become very small ($< 10\%$) for later stages of the collapse and hence yield the best approximation at this later epoch. The mean relative error of the opacity correction for all particles above $n > 10^{11}\,\mathrm{cm}^{-3}$ can be seen in Figure 4.11.

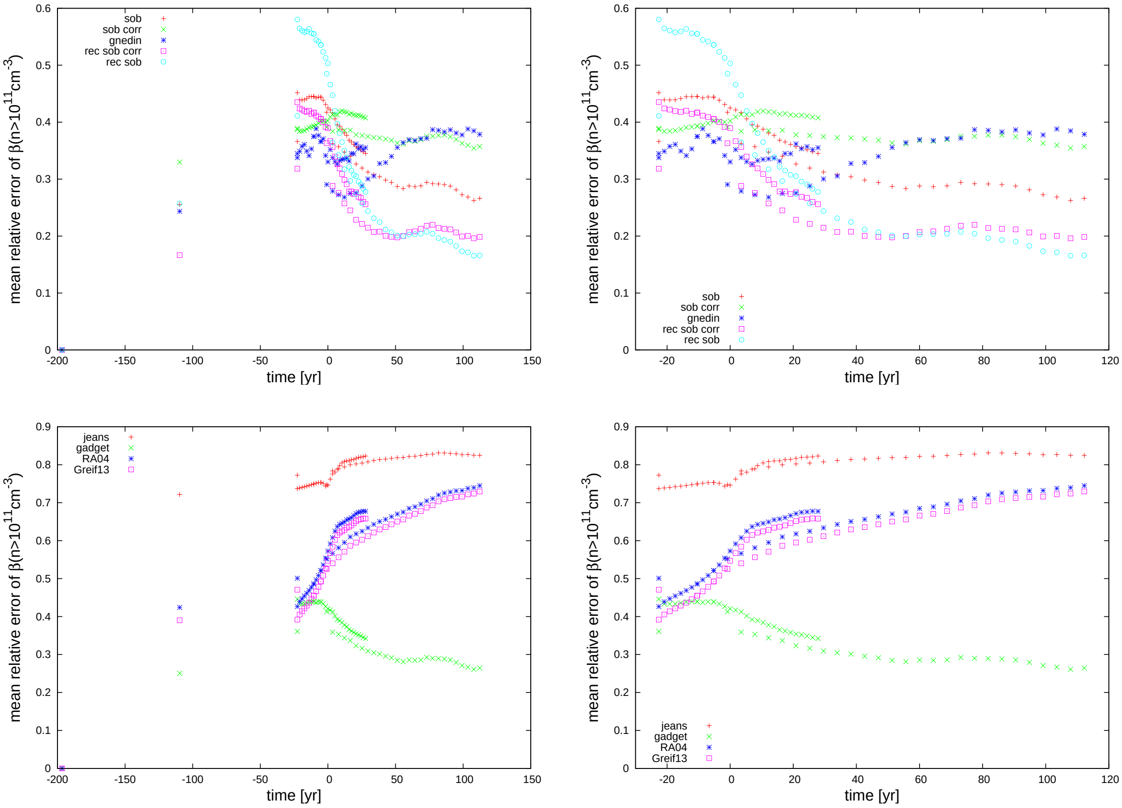

Figure 4.11: Mean relative error of the opacity correction for different methods as a function of time (at $t = 0$ the first sink particle form) for all particles above $n > 10^{11}\,\mathrm{cm}^{-3}$ (selection of most promising methods at the top, other methods at the bottom). When the first particles enter this density regime, the mean relative errors are already between $15 - 70\%$, rise to $30 - 90\%$ just before formation of the first sink particle and finally drop below 20% (at least for the reciprocal methods).

The particles enter this density regime at later times and the mean relative errors are generally higher ($20 - 90\%$). The Jeans approximation and analytical fits fail completely in this density regime with errors above 50%. Although the other local approaches yield high mean relative errors between $20 - 50\%$, the reciprocal methods seem to converge towards an error of $\sim 20\%$. A direct comparison of the two reciprocal methods shows that the one which uses the uncorrected Sobolev lengths yields small mean relative errors at late stages of the collapse but errors above 50%

around formation of the first sink particle, whereas the reciprocal method which uses the corrected Sobolev length yields smaller errors around formation of the first sink particles. We can summarise this discussion and the quantitative comparison of different methods with four important findings:

1. During the formation of subsequent sink particles (respectively protostar) the cloud might flatten, which increases the photon escape probability perpendicular to the disc-like structure. The enhanced opacity correction due to this effect can only be captured by the lookup method and is totally missed by all other approaches which depend only on local quantities.
2. Although the opacity correction can be fitted analytically for each single timestep, one global fit function fails because the slope flattens with time. However, the fitting formula by Greif et al. (2013) yields slightly better results than the one proposed by Ripamonti & Abel (2004).
3. The Gnedin or Sobolev approaches might be accurate for some time or density regimes but still yield mean relative errors of $\sim 20\%$.
4. Since we capture only the first hundred years of the total primordial star formation (actually several thousand years), we should focus on the methods with the most promising long time accuracy. Only the newly introduced reciprocal approaches yield the satisfactorily small relative errors at later stages with mean relative errors below $\sim 10\%$.

4.3 Fragmentation

We want to analyse the fragmentation behaviour of a primordial cloud in order to answer the question, whether we end up with one massive star or with a bunch of small stars. As we have seen in Figure 1.1, this is a crucial but poorly understood question. We want to answer it under the aspect of different cooling implementations. The first intuitive approach might be the analysis and comparison of the sink particles at the end of the simulation. In Figure 4.12 we see the time evolution of the number of sink particles and the number of sink particles as a function of the most massive one. Based on these plots alone, we can hardly see a trend for the different methods. However, ionising radiation photodissociates the molecular hydrogen, once the first protostar reaches a mass of $10 - 15 M_\odot$ (Smith et al. 2011). Hence, cooling might become ineffective and fragmentation is suppressed. Using this criteria (indicated in the right plot by the horizontal grey dashed lines at $15 M_\odot$) and ignoring all further sink particle creations beyond this point, there is a clear trend. While the TreeCol-based methods might yield final protostar numbers around 8 (left) and 10 (right), the final number of protostars for the Sobolev-based runs are 4 (left) and 8 (right). Since we have not yet implemented a proper protostellar feedback model into the code, nor do we account for merging events, we can only speculate about

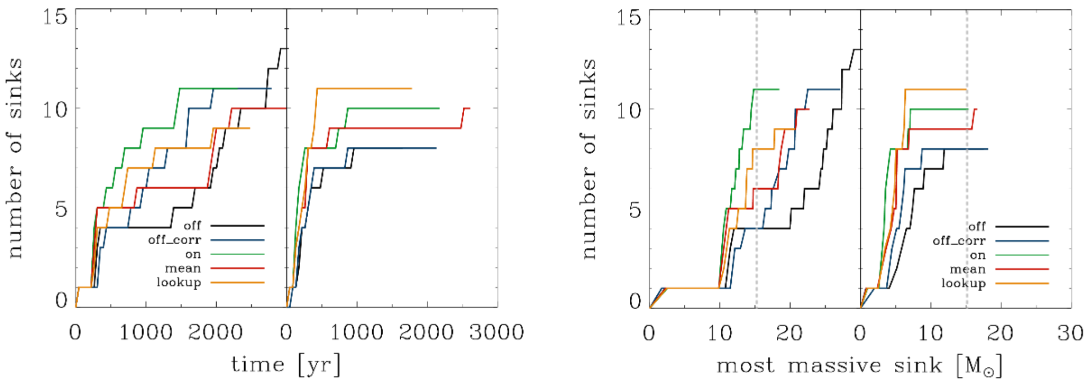

Figure 4.12: Number of sink particles as a function of time (left plot) and as a function of the most massive sink particle (right plot) for different cooling approaches. These plots are based on two different realisations of the synthetic initial conditions (left/right within plots). The horizontal grey dashed lines on the right hand side indicate the moment when the most massive sink particle has a mass of $15M_{\odot}$.

properties and the number of protostars beyond this point. Furthermore, fragmentation is a highly chaotic process and we can not base our conclusions on only two realisations.

Consequently, we have to increase the statistics and analyse further properties of the collapse to see, whether different cooling implementations have an influence on the fragmentation behaviour. As already seen in section 1.3.4 there are different fragmentation criteria. The quantification and comparison of these criteria yields a much more general and fundamental analysis than merely the number of sink particles.

We compare the two runs based on cosmological conditions with the Sobolev approximation and the lookup method. Since one run might cool faster, the clouds might not collapse synchronously. In order to compare the simulations at the same stages of the collapse anyway, we define several criteria and assign the corresponding output files. An overview of these criteria and other important quantities of the collapse are given in Table 4.2 for the lookup runs and in Table 4.3 for the Sobolev runs. For both methods individually, we combine data from the run with the small accretion radius (which crashes quite early) and the run with a larger accretion radius. Even though the choice of accretion radius does not have any influence on the large-scale behaviour of our cloud, there is a decrease in the number of sink particles for this transition. Since the superposition of both simulations is the best alternative to both resolve the first part of the collapse with high spatial resolution and the later stages as long as possible, we nevertheless stick to this.

One remark about the binning, smoothing and scatter of the following plots: Generally, each simulation contains about 20 million particles, but we can not plot all these data points at once. Furthermore, SPH particles have a smoothing length, which should be considered for projections of individual quantities. Hence, we use

label	criterion	time [yr]	#sinks	$m_{\mathrm{acc}}[M_\odot]$	$m_{\mathrm{max}}[M_\odot]$	r_{acc}[AU]
a	$n \lesssim 10^{10}\,\mathrm{cm}^{-3}$	-893	0	-	-	3
b	$n \lesssim 3 \times 10^{13}\,\mathrm{cm}^{-3}$	-22.6	0	-	-	3
c	$n \lesssim 3 \times 10^{14}\,\mathrm{cm}^{-3}$	-5.2	0	-	-	3
d	first sink	0	1	0.163	0.163	3
e	$m_{\mathrm{acc}} \simeq 1.6 M_\odot$	8.7	3	1.565	0.594	3
f	$m_{\mathrm{acc}} \simeq 5 M_\odot$	33.9	2	5.054	2.942	20
g	$m_{\mathrm{acc}} \simeq 10 M_\odot$	99.2	2	9.923	5.493	20

Table 4.2: Overview and nomenclature of different snapshots as a reference for the following plots. Contains data from the two simulations (with small and larger accretion radius) which are based on the cosmological initial conditions and use the *lookup* method. The criteria guarantee comparability with the Sobolev runs. m_{acc} is the total mass accreted by all sink particles, whereas m_{max} is the mass of the most massive sink particle. The comparison of these values indicates that the sink particles are almost equally massive at each time. Since we combine two different simulations, the number of sink particles decreases between snapshot e and f. Although this is physically not realistic, it is the best option we could do in order to follow the collapse and fragmentation as long as possible.

label	criterion	time [yr]	#sinks	$m_{\mathrm{acc}}[M_\odot]$	$m_{\mathrm{max}}[M_\odot]$	r_{acc}[AU]
a	$n \lesssim 10^{10}\,\mathrm{cm}^{-3}$	-898	0	-	-	3
b	$n \lesssim 3 \times 10^{13}\,\mathrm{cm}^{-3}$	-19.1	0	-	-	3
c	$n \lesssim 3 \times 10^{14}\,\mathrm{cm}^{-3}$	-7.0	0	-	-	3
d	first sink	0	1	0.298	0.298	3
e	$m_{\mathrm{acc}} \simeq 1.6 M_\odot$	13.9	1	1.623	1.623	3
f	$m_{\mathrm{acc}} \simeq 5 M_\odot$	37.4	1	5.067	5.067	20
g	$m_{\mathrm{acc}} \simeq 10 M_\odot$	103	1	9.914	9.914	20

Table 4.3: Overview and nomenclature of different snapshots as a reference for the following plots. Contains data from the two simulations (with small and larger accretion radius) which are based on the cosmological initial conditions and use the *Sobolev* approximation. The criteria guarantee comparability with the lookup runs. m_{acc} is the total mass accreted by all sink particles, whereas m_{max} is the mass of the most massive sink particle. One should keep in mind that we combine two different simulations in order to follow the collapse and fragmentation as long as possible.

two plotting routines:

- Radius/density/enclosed mass are binned and the particular quantity is the mass weighted mean within each bin. An equidistant binning might overinterpret bins which contain only few particles. Therefore, we start with 128 (logarithmically) equidistant bins and recursively split the bin which contains the most particles and merge those bins which contain fewest particles until the minimal and maximal number of particles in each bin is within a factor of 10^4. We do generally not plot the scatter of the individual bins, because it might be confusing and does rarely contain any additional information.

- For projections of a certain quantity onto the plane, we create two dimensional histograms - one histogram of the required quantity and a second one of the smoothing lengths. Combining these two histograms and smearing out the desired quantity based on the smoothing kernel yields the final projection. Indeed, it might be interesting to see, where the protostars are in these projections. However, the protostars are either too tiny to be seen or they are too large and might cover other interesting characteristics of the projection. Therefore, a compilation of their positions can be found in the appendix (Figure B.1 to Figure B.4).

4.3.1 Collapse

First of all, we want to analyse the collapse for the lookup method, because on the one hand we expect them to be the most realistic simulations. Thus, we can see the general collapse behaviour and afterwards focus on those quantities which are relevant for fragmentation. On the other hand, we can directly compare the results of our new method to the findings of previously published studies of primordial star formation. Since we are particularly interested in the differences in the optically thick regime and the fragmentation behaviour, we do not track the complete collapse, but rather follow the last $\sim$ 1000yr. Profiles of the density, enclosed mass, H_2 abundance and temperature at different times of the collapse are shown in Figure 4.13. The radial profile of the density has the expected $n \propto r^{-2.2}$ slope in the outer regime (compare cetion 1.3.3). Since the enclosed mass only accounts for the gas mass, its radial slope steepens again after formation of the first sink particle. The H_2 fraction depends strongly on the density, because it is mainly formed in three-body reactions at a density of around $10^{10}\,\mathrm{cm}^{-3}$ (see section 1.3.1). Hence, we merely see any evolution with time. The temperature as a function of density shows the typical features of the collapse of primordial gas (see e.g. Yoshida et al. 2006). The dip between $10^9 - 10^{10}\,\mathrm{cm}^{-3}$ characterises the interplay between the release of binding energy in three-body H_2 formation reactions and the almost optically thin H_2 line cooling.

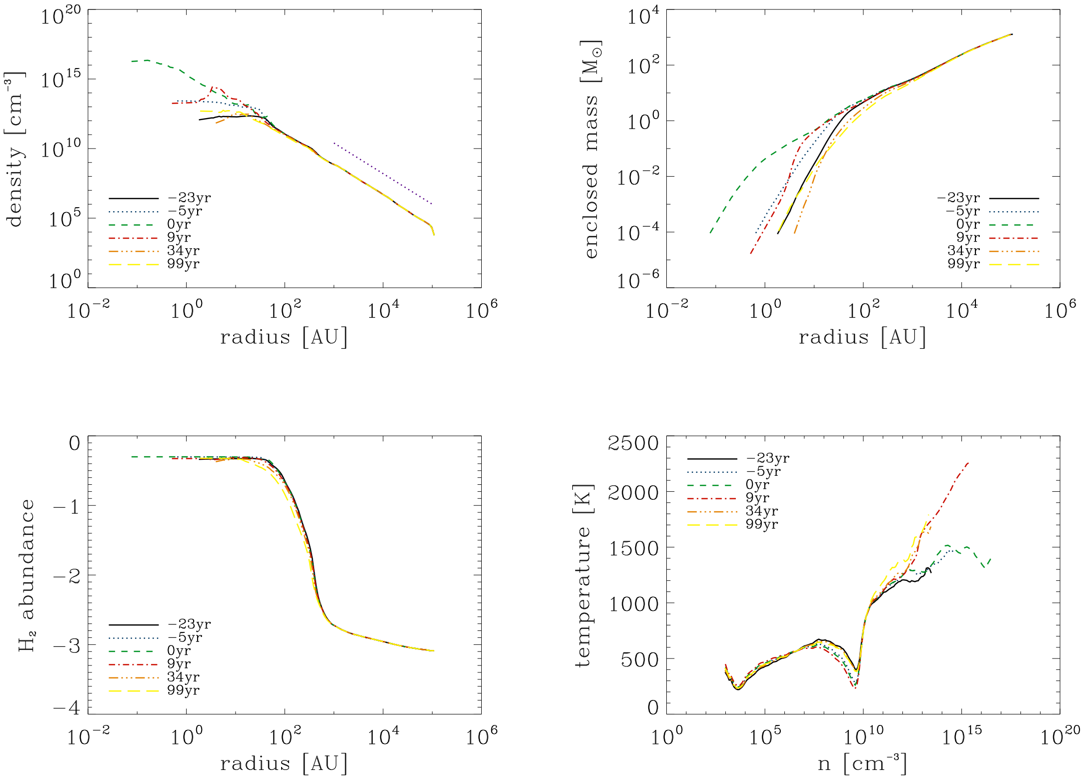

Figure 4.13: Different profiles of the collapse for the snapshots b–g. Top left: radial density profiles and the expected $n \propto r^{-2.2}$ slope in purple. Top right: enclosed gas mass as a function of radius. Bottom left: radial profile of the logarithmic H_2 abundance ($x_{H_2} = 0.5$ corresponds to fully molecular). Since this is mainly a function of density, we do not see any considerable change with time. Bottom right: temperature as a function of density.

Density

Since the dominating force on large scales is gravity, we first want to focus on the matter distribution of the cloud. The general density structure can be seen in Figure 4.14. The density profiles clearly show the formation of two clumps which leads to the formation of several sink particles. The elongated structure with two density peaks is already present some years before the formation of the first sink particle.

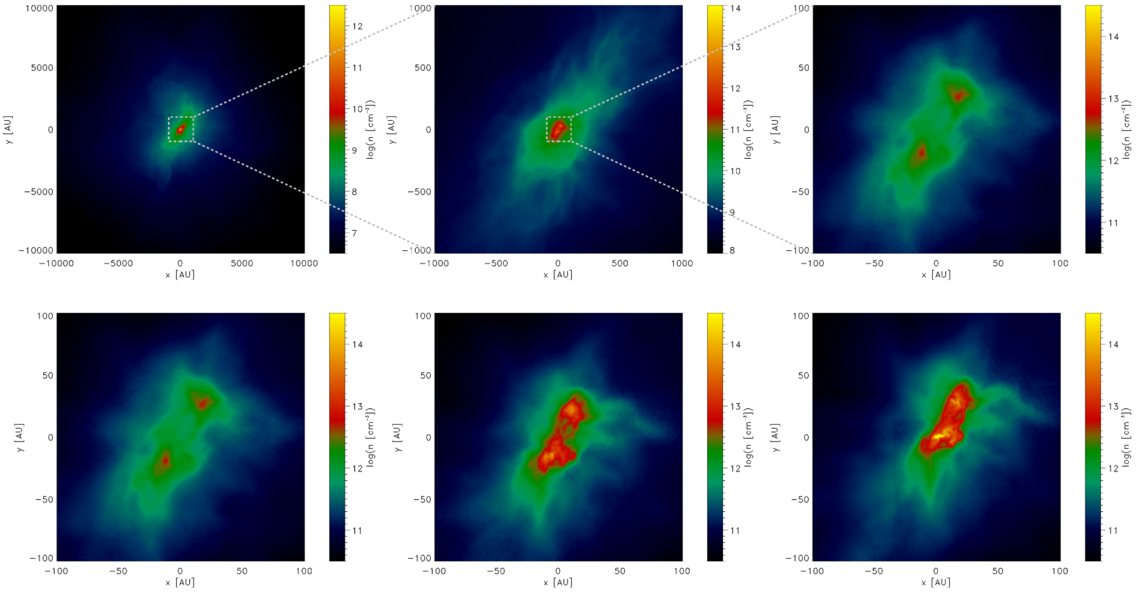

Figure 4.14: Density profiles of the snapshots b (top) and b–d (bottom). Top: zoom on star forming region 22.6yr before the first sink particle form (mind the different colour scalings). Bottom: Time evolution from snapshot b to the formation of the first sink particle (which is formed exactly in the centre of this last snapshot).

Opacity correction

In order to determine the regions and length scales on which the H_2 cooling becomes optically thick and the opacity correction actually has to be applied, Figure 4.15 illustrates a zoom on the central region of the cloud. From this figure it is clear that the opacity correction is only relevant in the inner part of the cloud and we can focus on this region. A time evolution of this region can be seen in Figure 4.16. The effects of opacity correction are most dominant around formation of the first sink particles. At the beginning of the collapse, the density is not yet so high and the opacity corrections does not deviate strongly from a value of one. Although the density increases during the collapse, the cloud might flatten with time (compare section 5.1.4) and the effective, angle-averaged opacity correction is even closer to one at the end of our simulation.

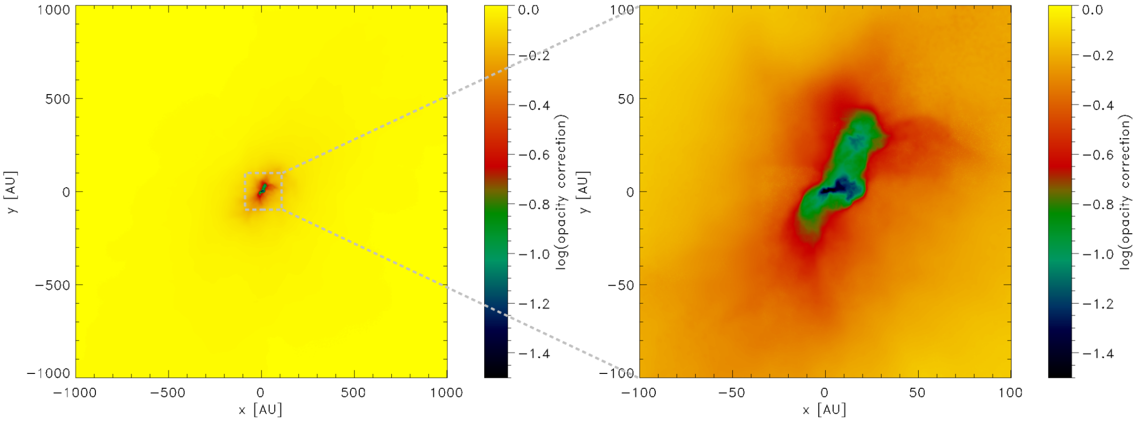

Figure 4.15: Opacity correction maps and zoom on region of interest for snapshot d (formation of the first sink particle).

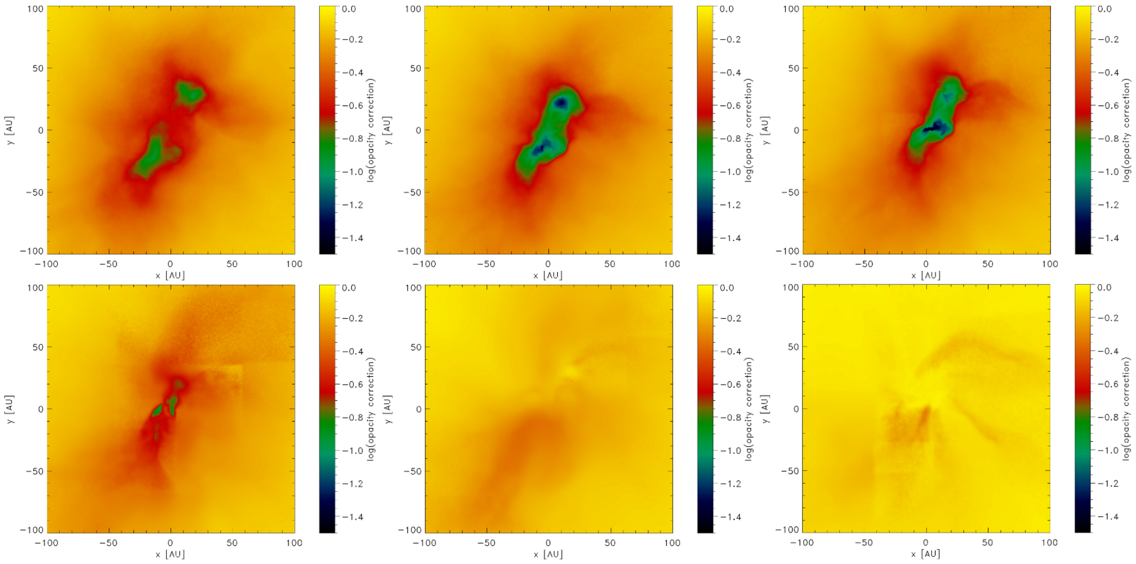

Figure 4.16: Time evolution of the opacity correction for snapshots b (top left) to g (bottom right). The effects of opacity correction are most pronounced around formation of the first sink particle (top right), whereas its influence decreases for later stages of the collapse.

Temperature

The cooling has direct influence on the temperature profile of the cloud, which can be seen in Figure 4.17. Since we are dealing with star formation in the early Universe, the temperatures are generally higher than for present-day star formation ($T_{\mathrm{CMB}} \simeq 60\mathrm{K}$, Equation 1.6). Although the temperature distribution seems to be very inhomogeneous on larger scales (whose deviations from spherical symmetry is discussed in section 4.3.1), it is roughly constant in the central 200AU.

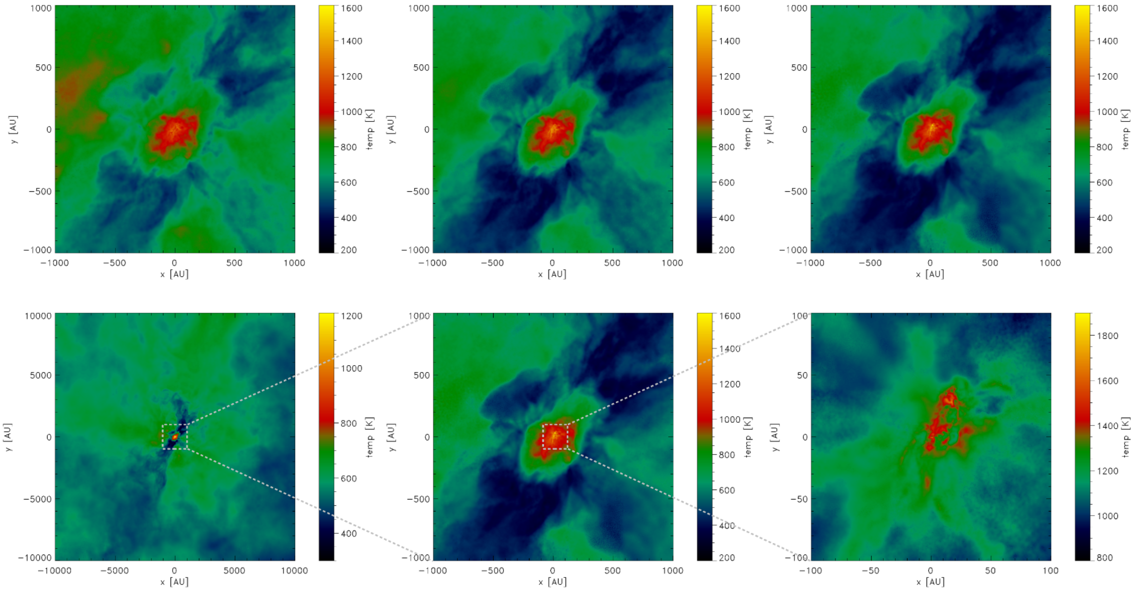

Figure 4.17: Temperature profiles of the snapshots b–d (top) and d (bottom). Top: time evolution from 22.6yr before the first sink particle form to the formation of the first sink particle. Bottom: zoom on star forming region at formation of the first sink particle (mind the different colour scalings). The snapshots with a side length of 2000AU clearly show a cold diagonal pattern. These deviations from sphericity is discussed in section 4.3.1.

Velocities

The opacity correction and different fragmentation criteria depend on characteristic velocities of the collapse. The radial profiles of these velocities are illustrated in Figure 4.18. While the radial profile of the sound speed and the Keplerian velocity remains almost the same during the collapse, the other velocities generally increase with time. Since the opacity correction is based on relative gas velocities, a higher radial velocity might boost the Doppler-shift of lines, therefore increases the photon escape probability and hence decreases the temperature by a higher cooling rate. As long as the tangential velocity is smaller than the Keplerian velocity, the disc is rotationally supported. This criterion is valid for regions with $r \gtrsim 50\mathrm{AU}$.

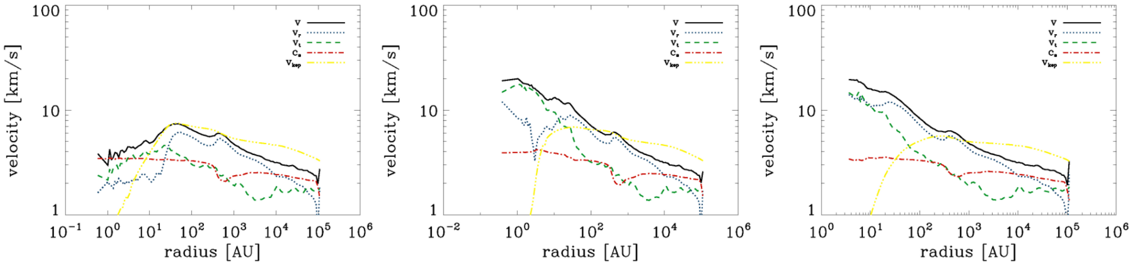

Figure 4.18: Radial profiles of different characteristic velocities for the snapshots c (left), e (middle), and f (right). Absolute (rms) velocity v (black solid), absolute value of the radial velocity v_r, which is generally pointing inwards (blue dotted), tangential velocity v_t (green dashed), sound speed c_s (red dash-dotted), and Keplerian velocity v_{kep} (yellow dot-dash-dotted).

Accretion Rate

The accretion rate quantifies the ability of the cloud to transport matter inwards and is illustrated in Figure 4.19. If the cloud is not able to forward gas inwards efficiently enough, the gas accumulates somewhere in the radial shells and probably fragment to form a new protostar. Since these are averaged profiles, this effect is not very pronounced, but the accretion rate as a function of enclosed mass peaks at some points, which might be an indicator for further fragmentation.

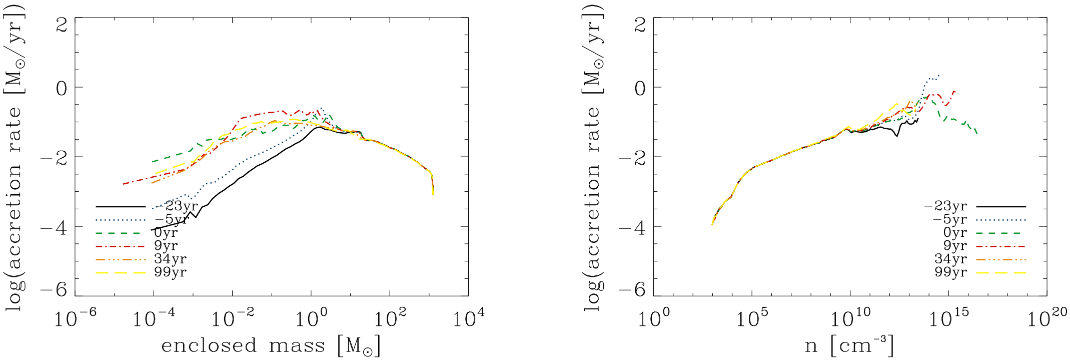

Figure 4.19: Mass accretion rate ($M_{\text{acc}} = 4\pi r^2 \rho v_r$) through spherical shells as a function of enclosed mass (left) and density (right). A peak in the accretion rate indicates that mass can not be transported inwards rapidly enough.

Timescales

A very convenient way to quantify the collapse and identify relevant processes is the comparison of different timescales, as it can be seen in Figure 4.20. While the radial profile of the free-fall time, the sound-crossing time and the orbital period

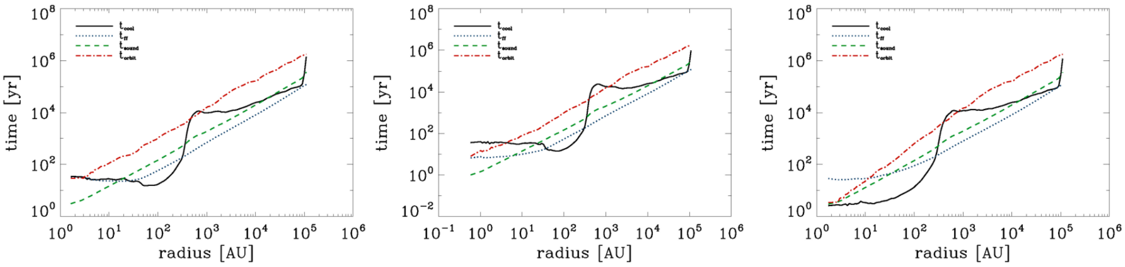

Figure 4.20: Radial profiles of different characteristic timescales for the snapshots b (left), c (middle), and g (right). Cooling time t_{cool} (black solid), free-fall time t_{ff} (blue dotted), sound-crossing time t_{sound} (green dashed), and orbital period t_{orbit} (red dash-dotted). Generally one can say, the smaller the time scale, the more dominating the process is.

can roughly be described by power laws, the cooling time can be classified into two regimes: a value of $t_{\text{cool}} = 10-100$yr for the inner ~ 100AU and a value $t_{\text{cool}} > 10^4$yr for regions beyond 1000AU. Since the free-fall time is always (except for the inner ~ 10AU) below the sound-crossing time, we can conclude two things. On the one hand, the cloud is gravitationally unstable (compare 1.3.4). On the other hand, possible artefacts due to the cut out of the whole cloud (which propagate roughly with sound speed) can not affect the process of star formation in the centre. Of special interest are those regions, where the cooling time is below the free-fall time ($r \simeq 100$AU), because fragmentation is promoted in these regions, as we see in the next section.

Stability Criteria

Finally, we analyse the fragmentation behaviour of the cloud. As we have seen before, there are different criteria, thresholds and regimes for fragmentation (see section 1.3.4). The three most common ones are probably the Gammie criterion (Equation 1.46), the Toomre parameter (Equation 1.45), and the comparison of cooling to free-fall time. The time evolution of the latter criterion can be seen in Figure 4.21. If $t_{\text{cool}} < t_{ff}$ the cloud can locally contract instead of globally collapse. The inner region seems to be unstable all the time, whereas the conditions for the outer regions change during the collapse. The radial profiles of this criterion are illustrated in Figure 4.22. The dip around $r \simeq 100$AU indicates the region where the cloud is most susceptible to fragmentation. Nevertheless, one single criterion is not sufficient in order to judge whether one should expect fragmentation or not (compare section 1.3.4). Therefore, we also want to include the other two criteria. The combination of all three criteria should be a valid quantification for fragmentation. Three maps of these criteria can be seen in Figure 4.23. Whereas the Gammie criterion and the comparison of times almost yield the same qualitative profile, the map of the Toomre parameter looks comparatively inhomogeneous. Hence, a quantifiable comparison of these criteria is given in Figure 4.24. If we require all three

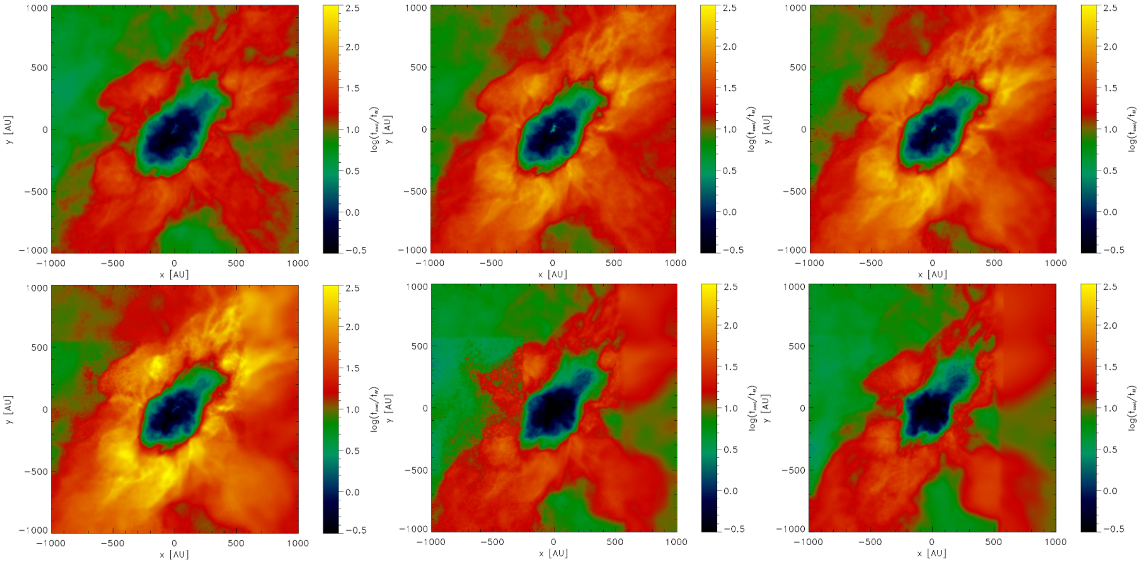

Figure 4.21: Sequence of snapshots b (top left) to g (bottom right), illustrating the stability criterion $t_{\rm cool}/t_{ff}$. Regions with $\log(t_{\rm cool}/t_{ff}) < 0$ might be susceptible to fragmentation. Whereas the inner ~ 100AU are unstable, the outer region appears to be stable against fragmentation.

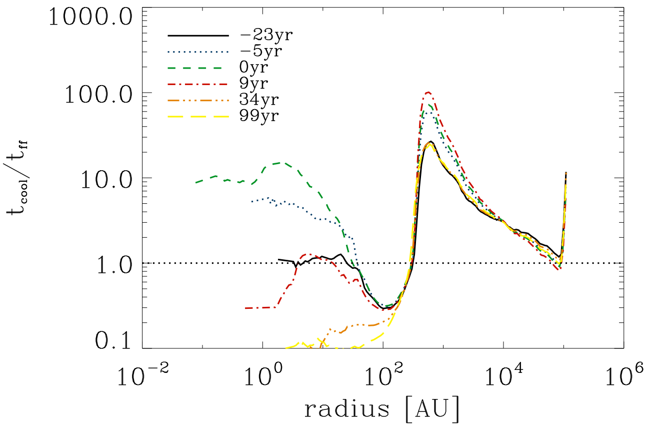

Figure 4.22: Radial profiles of $t_{\rm cool}/t_{ff}$. Below the black dotted line, we expect the gas to be gravitationally unstable and thus susceptible to fragmentation. While there is a ~ 50AU stable "island" in the centre until formation of the first sink particles, this region dissolves at later time.

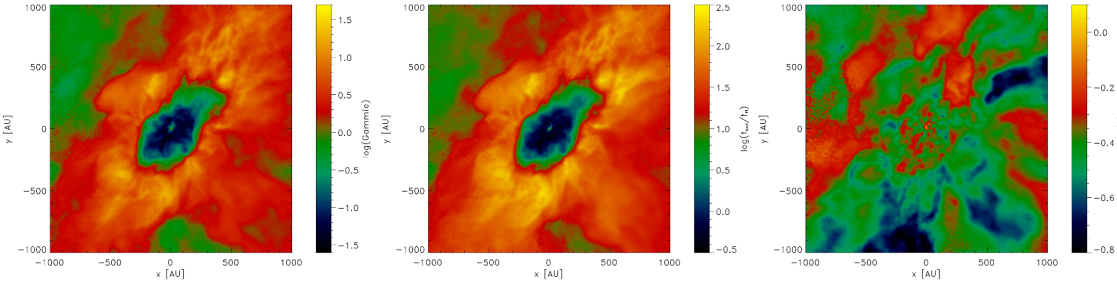

Figure 4.23: Different (in)stability criteria at formation of the first sink particle (snapshot d). Left: Gammie criterion. Middle: $t_{\rm cool}/t_{ff}$. Right: Toomre parameter. While the Gammie and cooling time profile qualitatively look the same, the map of the Toomre parameter is much more inhomogeneous.

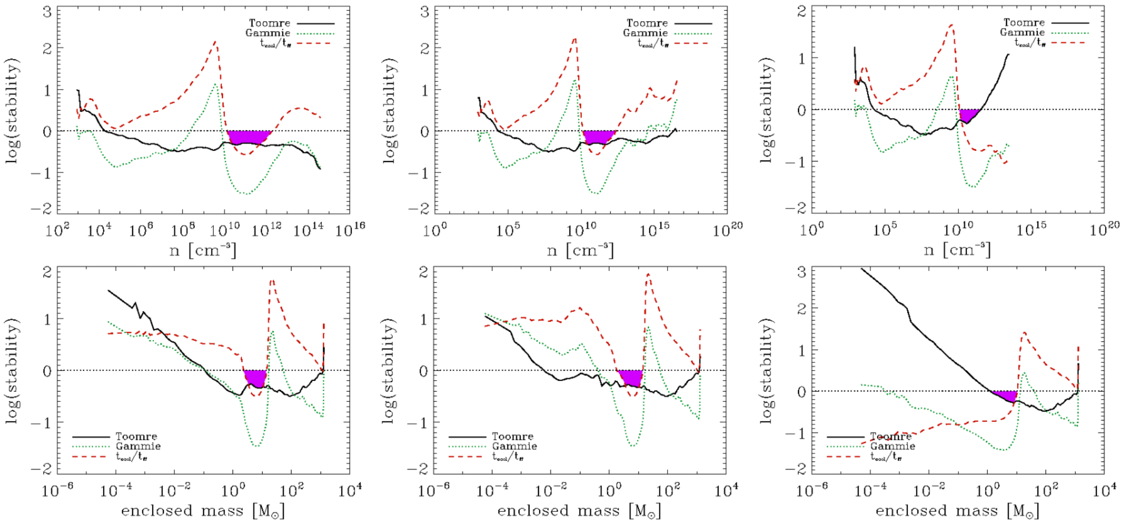

Figure 4.24: Different (in)stability criteria as a function of density (top) and enclosed mass (bottom). The plots show different stages of the collapse: c (left), d (middle), and f (right). Since we require all instability criteria to be fulfilled for the cloud to fragment, we illustrate these regions in purple. Interestingly, the Gammie criterion is fulfilled in these regions anyway and does not add an additional restriction. Hence, regions with densities of $10^{10} - 10^{12}\,\mathrm{cm}^{-3}$ and an enclosed mass of $1 - 20 M_\odot$ are most susceptible to fragmentation.

criteria to be fulfilled in order for the gas to fragment, these plots yield a quite exact prediction, where fragmentation should occur. In regions with densities between $10^{10}\,\mathrm{cm}^{-3}$ and $10^{12}\,\mathrm{cm}^{-3}$ the gas is most likely to fragment. This corresponds to an enclosed gas mass of $1 - 20M_\odot$.

Deviation from Spherical Symmetry

As we have seen before and as Figure 4.25 additionally illustrates, the collapse is not spherically symmetric. Even on large scales, the collapse is not isotropic, as the profile of the radial velocity shows. These deviations from spherical symmetry are due to the turbulent initial conditions and torques that act on the gas cloud. Since the Sobolev approach is a one-dimensional approximation that assumes spherical symmetry, it might not be able to capture the structure of the collapse. In order to show that these deviations from spherical symmetry are not just odd projection effects, Figure 4.26 shows the temperature projection along different axis. Since

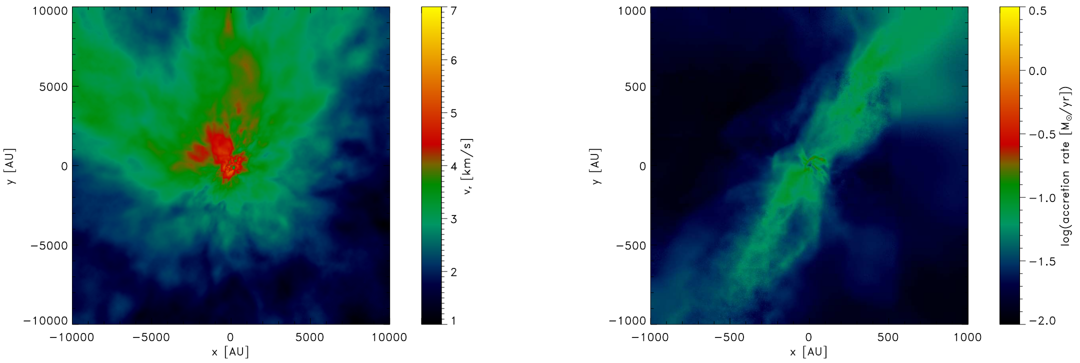

Figure 4.25: Profiles of the radial velocity (left) for snapshot b and the mass accretion rate (right) for snapshot g. These plots exemplarily illustrate that the collapse of a primordial cloud is by no means spherically symmetric.

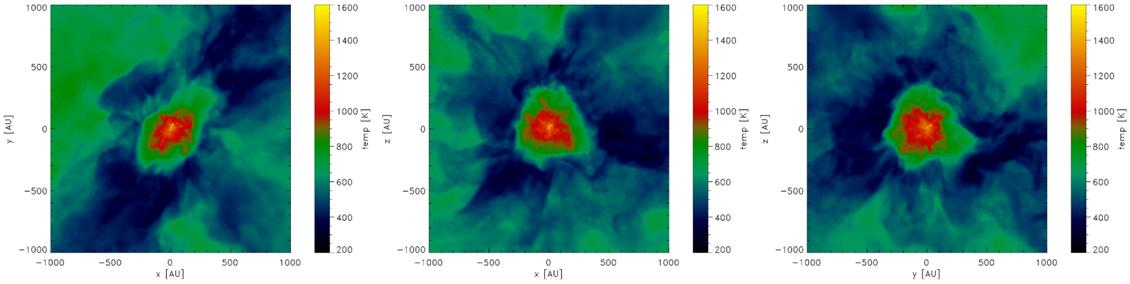

Figure 4.26: Temperature maps for snapshot d projected along the z- (left), y- (middle), and x-axis (right). Obviously the collapse is not spherically symmetric but rather there are individual radial streams of cold gas.

we see cold streams of gas, which point irregularly into different directions, we can conclude that the collapse is not spherically symmetric.

4.3.2 Comparison of Methods

In the last section we have extensively analysed the collapse and fragmentation behaviour of the lookup runs. In this section, we want to compare the basic quantities of these runs to the runs using the Sobolev approximation. At this point, we want to strengthen the fact that both runs only differ in the determination of effective column densities for the opacity correction of H_2 cooling. The runs start from exactly the same initial conditions and start to differ when entering the optically thick regime. Figure 4.27 shows the temperature as a function of density for both simulations before entering this regime. Hence, we can be sure that all subsequent differences do only rely on the different cooling implementations.

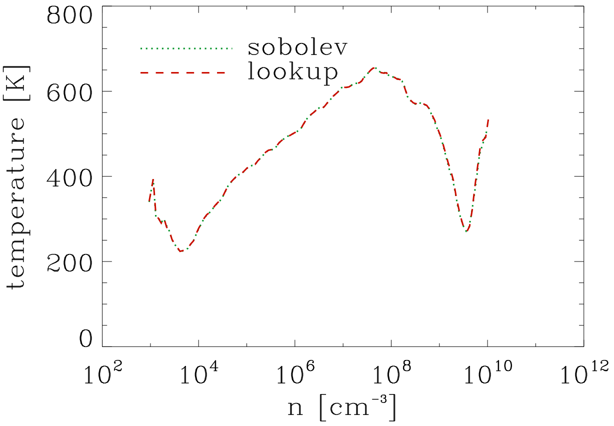

Figure 4.27: Temperature as a function of density for snapshot a. Up to the moment when the gas enters the optically thick regime, both simulations are completely identical.

Opacity correction

The first quantity to compare is naturally the opacity correction. Figure 4.28 illustrates the time evolution of the opacity correction for both methods. While the spatial distribution of the opacity correction seems to be smoother for the lookup run, the distribution is comparatively structured for the Sobolev approximation. Additionally, we see another important difference. Using the lookup method yields values for the opacity correction close to one at the end of the simulation, whereas the Sobolev approximation yields smaller photon escape fractions. Obviously, the Sobolev approximation is not able to capture the flattening of the cloud (see section 5.1.4). Furthermore, the Sobolev-based simulation develops only one central core, while an elongated core with two peaks is formed in the lookup run. Since the

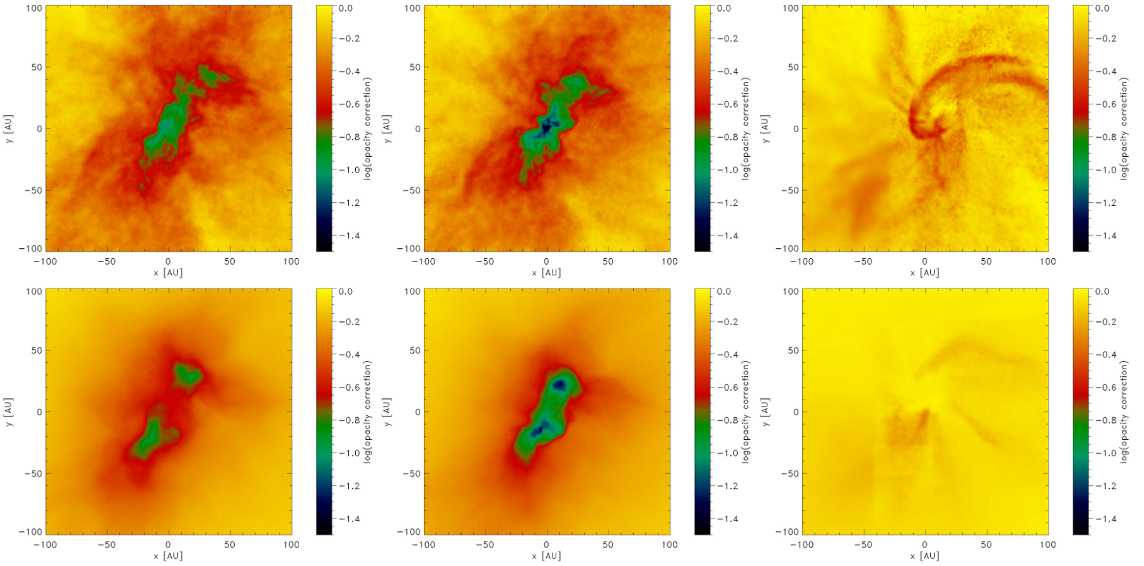

Figure 4.28: Opacity correction maps for the Sobolev method (top) and the lookup method (bottom) at different times of the collapse: b (left), c (middle), and g (right). The opacity correction appears to be smoother for the lookup approach.

opacity correction has a direct influence on the cooling rates, we are consequently interested in the H_2 cooling rates, which are illustrated in Figure 4.29. Surprisingly, the cooling rate is not much higher for the lookup run, although the photon escape fractions are higher. This can be explained by the cooling implementation: due to the presumably higher cooling rate in the lookup run, the thermal equilibrium is reached for lower temperatures. Thus, the cloud simply remains cooler instead of increasing its cooling rate significantly.

Temperature

The temperature maps for the two different methods are shown in Figure 4.30. The hot gas is more centrally concentrated for the Sobolev-based run, whereas the hot gas is fluffily distributed in the inner region for the lookup run. As already mentioned above, the gas in the Sobolev run is generally hotter, which can also be seen in Figure 4.31. The difference of temperatures in this inner regime can be up to ~ 500K, which has significant influence on the fragmentation behaviour, as we see below.

Density

A comparison of the density profiles can be seen in Figure 4.32. While the cloud appears to be more spherically symmetric and has only one density peak for the Sobolev run, the run using the lookup method yields a more elongated core with two density peaks. This second peak leads to the formation of another sink particle.

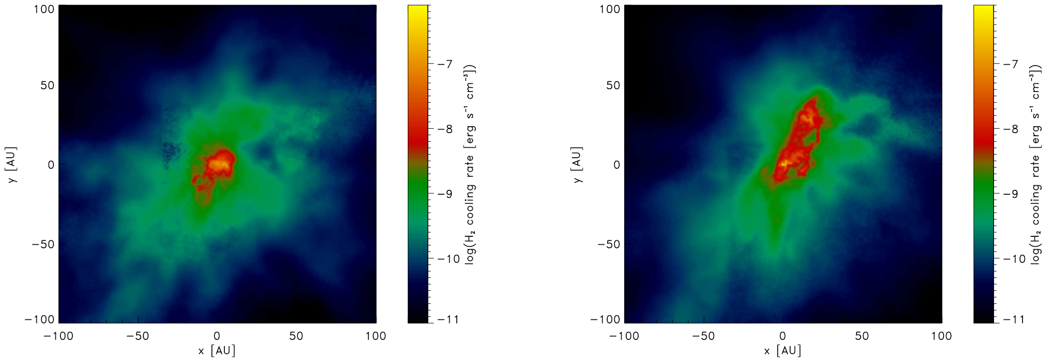

Figure 4.29: H_2 cooling rate for the Sobolev method (left) and the lookup method (right) at formation of the first sink particle (snapshot d). The region of efficient cooling is larger in the right plot.

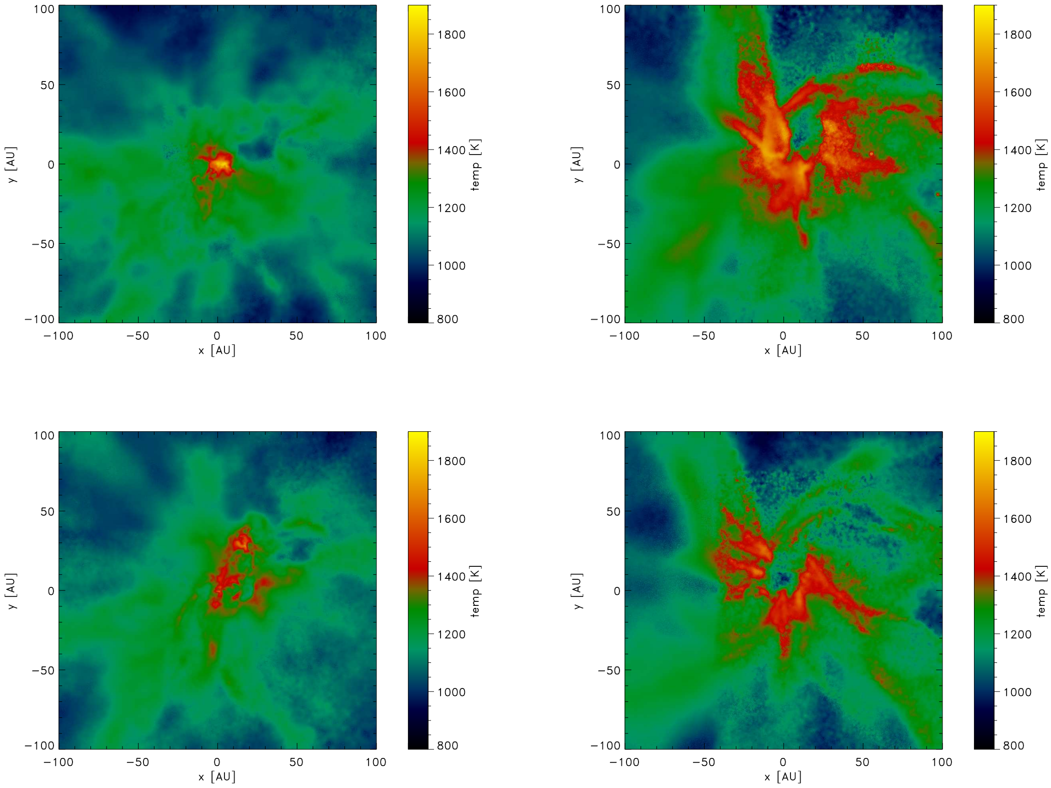

Figure 4.30: Temperature profiles for the Sobolev method (top) and the lookup method (bottom) at different times of the collapse: d (left) and g (right). In the upper plots, the temperature is generally higher.

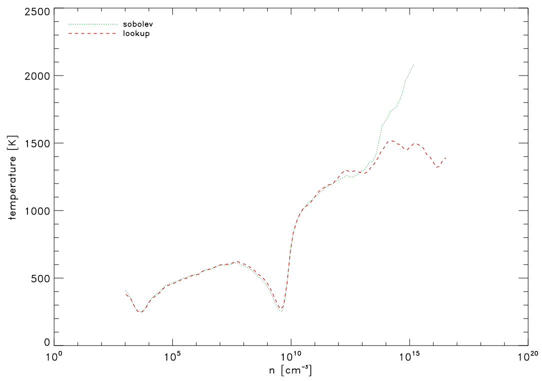

Figure 4.31: Temperature as a function of density (left) and as a function of radius (right) shortly after formation of the first sink particle (snapshot d). Comparison of the Sobolev approximation (green dotted) and the lookup method (red dashed). In the inner, high-density regime, the lookup approach yields lower temperatures by up to $\sim$ 500K.

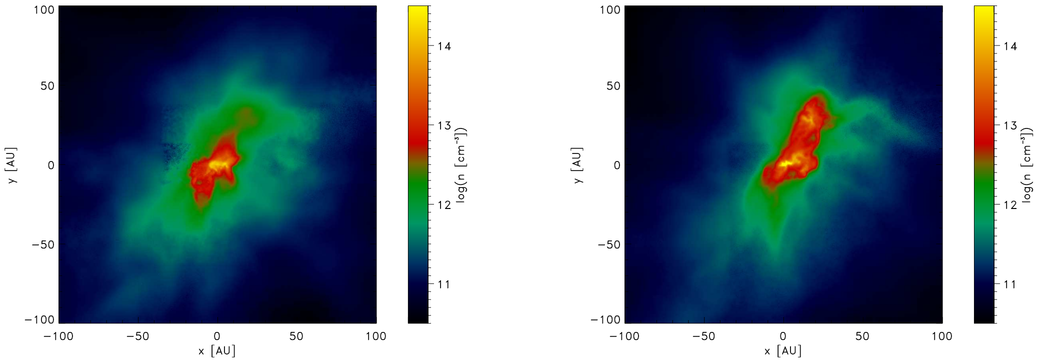

Figure 4.32: Density for the Sobolev method (left) and the lookup method (right) at formation of the first sink particle (snapshot d). For the lookup approach the high-density core is more elongated and about to fragment into two pieces.

Since the chemo-thermal instability (section 1.3.4) might occur independently of the cooling approach, its influence should be present in both simulations. Hence we conclude that this second density peak is an outcome of the new cooling method.

Accretion Rate

As we have seen above, the accretion rate can be an indicator for fragmentation if the gas can not be transported inwards efficiently enough. The maps of mass accretion rates are illustrated in Figure 4.33. While the spherical mass accretion rate is lower and comparatively smooth for the Sobolev-based run, it is more structured and shows a clear off-centre peak for the lookup run. This peak in the mass accretion rate is an indicator for fragmentation, because the gas accumulates in this region and can locally collapse.

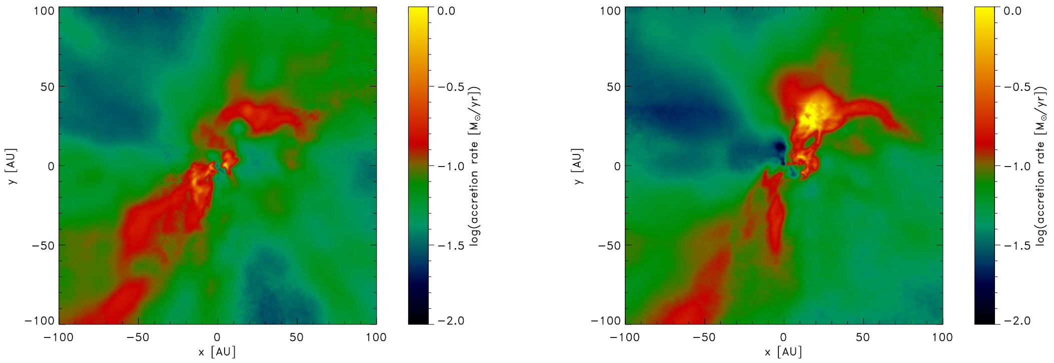

Figure 4.33: Mass accretion rate for the Sobolev method (left) and the lookup method (right) at formation of the first sink particle (snapshot d). The yellow peak in the right plot indicates the birthplace of the first protostar, whereas the smaller peak in the centre leads to the formation of subsequent sink particles.

Stability Criteria

Finally, we compare different fragmentation criteria of the clouds. Figure 4.34 shows the radial and density profile of the Toomre parameter. In the radial profile as well as in the density profile, the value of the Toomre parameter remains longer under the threshold of stability for the lookup run. Hence, the region and density regime where we expect fragmentation to occur is larger in this case. A map of the Gammie criterion is shown in Figure 4.35. Since the value of zero indicates the transition between stable and unstable, there is an obvious trend towards more fragmentation for the lookup-based run. Although the fragmentation behaviour in the central region is almost the same for both cooling approaches, the gas in the lookup method is much more susceptible to fragmentation in the outer region. The ratio of the cooling time over the free-fall time is illustrated in Figure 4.36. Here, we see a clear

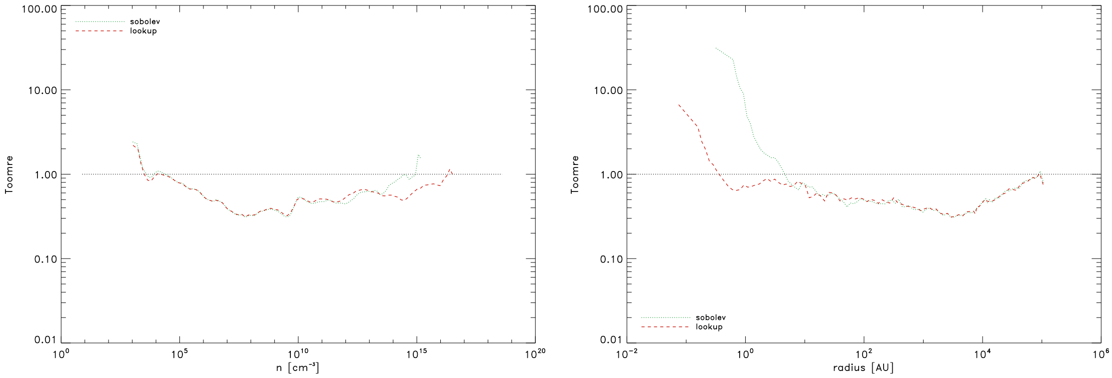

Figure 4.34: Toomre parameter as a function of density (left) and as a function of radius (right) for snapshot d. Comparison of the Sobolev approximation (green dotted) and the lookup method (red dashed). The cloud is susceptible to fragmentation for values below one, which is indicated by the black dotted line. In the inner high-density regime, the lookup value remains longer under this threshold, implying a susceptibility to fragmentation.

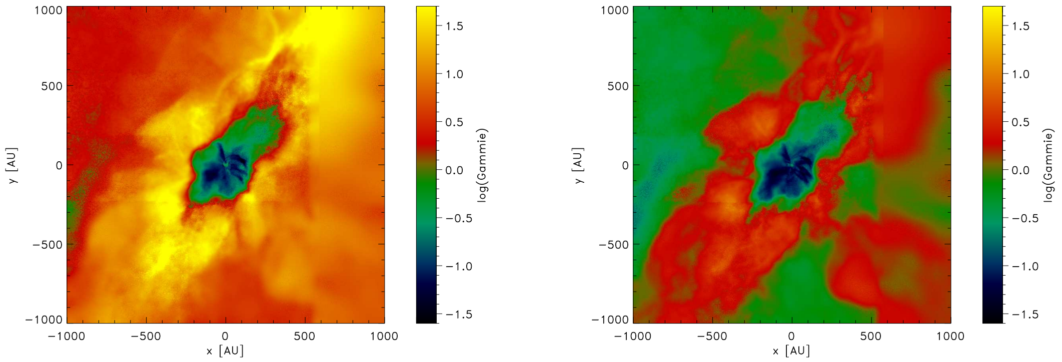

Figure 4.35: Gammie criterion for the Sobolev method (left) and the lookup method (right). 100 years after the first sink particle has formed (snapshot g), there is a huge difference in the fragmentation behaviour. According to the Gammie criterion, the gas in the lookup run is much more likely to fragment.

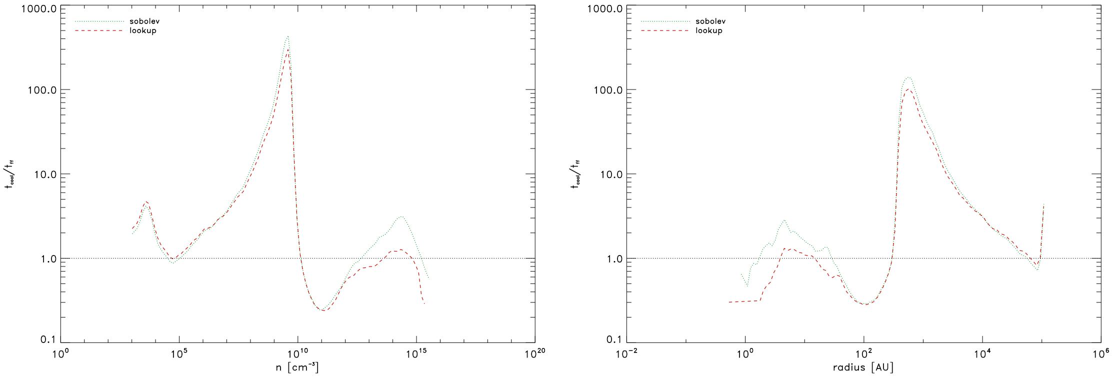

Figure 4.36: t_{cool}/t_{ff} as a function of density (left) and as a function of radius (right) for snapshot e. Comparison of the Sobolev approximation (green dotted) and the lookup method (red dashed). The cloud is susceptible to fragmentation for ratios below one, which is indicated by the black dotted line. While the Sobolev profile is clearly above this threshold in the inner high-density regime, the lookup value is almost completely below it. This illustrates a clear preference for fragmentation in the lookup run.

difference in the inner (~ 30AU) high-density region. While the ratio for the lookup run is almost completely below the critical threshold, it is almost entirely above one for the Sobolev-based run in this regime. Therefore, we expect fragmentation more likely to happen in the lookup run.

Summing up these three stability criteria, the gas is more susceptible to fragmentation in the lookup run than in the Sobolev run, according to each of these three criteria individually.

As a final remark one should mention that we obviously selected individual plots at certain times of the collapse in order to verify our assumptions. Clearly, we can not include all possible plots, profiles, and snapshots in this thesis. However, the general trend presented in this section is present in almost all of the remaining plots. Hence, the selected plots are a representative sample of the collapse quantities.

The main findings of this section can be summarised by these five conclusions:

1. We reproduce the main characteristics of a collapsing primordial cloud.
2. The cooling implementation has a significant influence on the collapse and the fragmentation behaviour.
3. The Sobolev approximation is not able to capture the increase of the photon escape fraction at later stages of the collapse.
4. Several fragmentation criteria individually support the trend towards more fragmentation in the lookup runs, compared to the Sobolev-based ones.
5. The primordial gas cloud is most susceptible to fragmentation in the density regime $10^{10}\,\mathrm{cm}^{-3} \leq n \leq 10^{12}\,\mathrm{cm}^{-3}$.

4.4 IMF

Primordial gas does not contain any metals ($\log(Z_{\mathrm{primordial}}/Z_{\odot}) < -5$, compare Figure 1.3). Hence, the primordial IMF is of special interest, because it defines almost all characteristics of primordial stellar populations. Since no Pop III star has been discovered until today, the IMF can not be constrained observationally but only based on simulations. As already discussed in section 1.3.5, the shape of the primordial IMF is only poorly understood and the scatter and uncertainties are large. Generally, the IMF is expected to be more top-heavy in the early Universe, because Pop III stars tend to be more massive than their present-day counterparts. Hence, we want to find a characteristic mass range and verify this assumption about the primordial IMF based on our simulations. Since we use a sink particle approach, we do not simulate the stellar physics properly. Rather, we use a very simple model for the accretion luminosity feedback and do not consider effects of ionising radiation. Moreover, the current code does not capture merger events, nor do we run the simulation long enough to really determine an *initial* mass function. The only thing we can derive based on our simulations is a characteristic mass scale for primordial protostars, respectively a “sink particle mass function”.

4.4.1 Accretion

Once a protostar has formed, its final mass is mainly based on its ability to accrete surrounding gas. Since for primordial gas the temperature is higher, also the accretion rate is increased (Equation 1.47). The data outputs of our simulations are only at discrete timesteps and therefore the accretion rates of individual sink particles fluctuate intensely, which is unphysical. Hence, we illustrate the accreted mass by all sink particles as a function of time in Figure 4.37. The slope of these plots represents the mass accretion rate of the sink particles and is almost equal for all methods. The mean mass accretion rate for all sink particles in this time interval is roughly $\dot{M} \simeq 0.036 M_{\odot}\mathrm{yr}^{-1}$, while we should keep in mind that 4–11 sink particles have been formed in these simulations. The accretion process is significantly influenced by the characteristics of the most massive sink particle, due to accretion feedback, ionising radiation, and fragmentation induced starvation (compare section 1.3.5). Therefore, we illustrate the mass of the most massive sink particle as a function of time in Figure 4.38. The most massive sink particle (which is generally the first sink particle to be formed) starts with a very high accretion rate ($\dot{M}_1 \simeq 4.4 \times 10^{-2} M_{\odot}\mathrm{yr}^{-1}$) and decreases the accretion to $\dot{M}_2 \simeq 6.6 \times 10^{-3} M_{\odot}\mathrm{yr}^{-1}$ when subsequent sink particles form. The most massive sink particle generally accretes faster for the Sobolev-based runs. Since the overall accretion rate onto all sink particles is roughly the same for the individual methods (compare Figure 4.38), we conclude that more sink particles form in the TreeCol-based runs (which is in compliance with Figure 4.12). These sink particles necessarily have smaller masses than those in the Sobolev-based runs (“fragmentation induced starvation”, compare section 1.3.5).

We can perform a similar analysis for the simulations based on cosmological initial

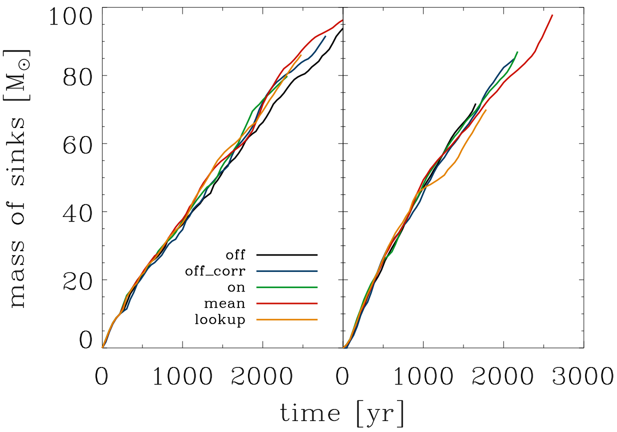

Figure 4.37: Accreted mass of all sink particles as a function of time for different cooling approaches. These plots are based on two different realisations of the synthetic initial conditions (left/right). The overall gas accretion rate is approximately constant with a value of $\dot{M} \simeq 0.036 M_\odot \mathrm{yr}^{-1}$.

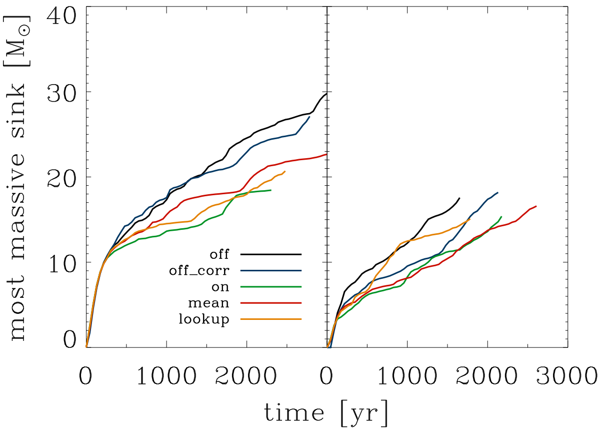

Figure 4.38: Mass of the most massive sink particle as a function of time for different cooling approaches. These plots are based on two different realisation of the synthetic initial conditions (left/right). For both realisations we see the trend that the TreeCol-based runs generally yield smaller masses for the most massive sink particle.

conditions. These simulations capture only a shorter period of the collapse, have less time to fragment and form stars and therefore suffer even more by the lack of statistical evidence. Nevertheless, we follow the collapse with a very high spatial and temporal resolution. A comparison of the accreted mass for individual sink particles and the associate accretion rates are illustrated in Figure 4.39, The lookup-based

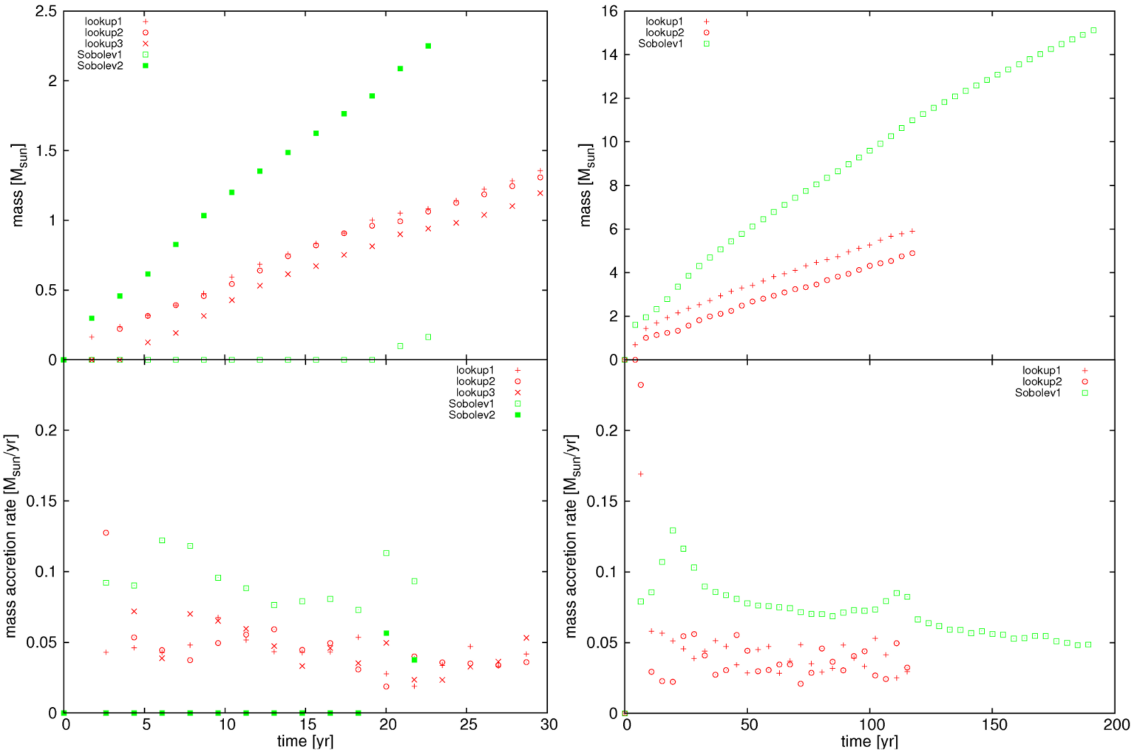

Figure 4.39: Mass of the individual sink particles (top) and accretion rate (bottom) as a function of time. Comparison of the lookup method (red) and Sobolev approximation (green) for the run with an accretion radius of $r_{\rm acc} = 3$AU (left) and $r_{\rm acc} = 20$AU (right). Although the overall accretion rate is roughly the same for all runs and methods, the individual accretion rates onto the sink particles differ, due to the variable number of sink particles in each simulation. Whereas the Sobolev-based simulation tend towards less sink particles and higher individual accretion rate, the lookup-based runs generally create more sink particles with smaller accretion rates.

runs tend to promote fragmentation and hence create more sink particles, whereas only one or two sink particles form for the Sobolev-based runs. Generally, the accretion rates are higher ($\dot{M}_2 = 10^{-2} - 10^{-1} M_\odot \mathrm{yr}^{-1}$) compared to previous findings (see section 1.3.5). If only one sink particle is present, its accretion rate is significantly higher to those cases, where several sink particles competitively accrete gas. Hence, we can conclude that while the Sobolev approximation promotes the creation of a few massive stars, the lookup methods seems to create more low-mass stars. Nevertheless, one should keep in mind the low number of stars and therefore the poor statistical evidence of these findings.

4.4.2 Mass Function of Protostars

Since we can not derive the actual IMF and since all simulations crash at different times, we have to find a criterion at which point in time we want to compare the mass functions. According to Smith et al. (2011), we have not implemented the required physics to follow the protostars beyond the point when the first protostar reaches a mass of $15 M_\odot$. Hence, we use this criterion and illustrate the corresponding sink particle mass functions in Figure 4.40. Since neither the histograms are normalised (total stellar mass might be different for the methods), nor do they include a sufficient number of sink particles, we can not draw a general conclusion about the shape of the IMF. Even the cumulative mass function (see Figure 4.41) does not reveal any trends between the methods. Nevertheless, the cumulative mass function clearly

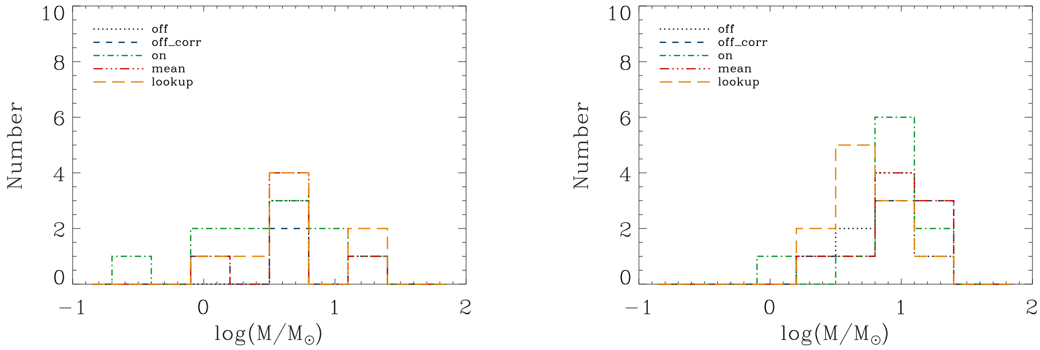

Figure 4.40: Sink particle mass function for different cooling approaches. These plots are based on two different realisation of the synthetic initial conditions (left/right). The trend is the same as in Figure 1.14, although with a much smaller number of protostars.

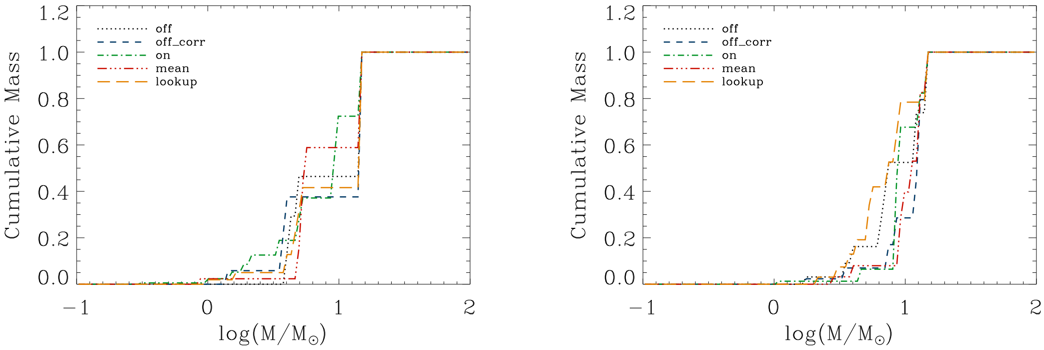

Figure 4.41: Cumulative mass function of the sink particles for different cooling approaches. These plots are based on two different realisations of the synthetic initial conditions (left/right).

identifies the sink particle mass function to be top-heavy (dominated by stars with $M > M_\odot$), whereas the present-day IMF is generally dominated by smaller stars with a characteristic mass of roughly $m_c \simeq 0.2 M_\odot$ Chabrier (2003). Hence, we can confirm that the primordial IMF is shifted towards higher-mass stars, regardless the cooling implementation.
The five most important finding of this section are:

1. The accretion rate onto primordial protostars is very high ($\dot{M}_2 = 10^{-2} - 10^{-1} M_\odot \mathrm{yr}^{-1}$) compared to present-day accretion rates.
2. The overall accretion rate onto all sink particles is almost the same, regardless the implemented cooling approach.
3. Since the lookup methods favours fragmentation, more sink particles form and the individual accretion rates are lower, compared to the Sobolev-runs.
4. Due to the small number of sink particles and thus the low statistical evidence, we can not constrain the shape of the mass function.
5. The primordial mass function is shifted towards high-mass stars, regardless the implemented cooling approach.

5 Discussion

5.1 Why Sobolev Fails

In section 4.2 we have seen that the Sobolev approximation fails in determining the proper effective column densities for H_2 cooling. Although it yields acceptable results up to the formation of the first sink particles, the Sobolev approach breaks down at later phases of the collapse, because it can not capture the evolving dynamical structure. Yet, we want to understand in detail, which assumptions break down, which approximations might be valid and under which circumstances one can still use the Sobolev method. In this section we focus on the Sobolev method, although most of the findings are also valid for other local approaches like the Gnedin or Jeans approximation.

5.1.1 Neglect of True Line Overlap

In his original derivation, Sobolev (1947) considered possible absorption and emission only in the frequency interval $[\nu_0 - \Delta\nu_{\rm th}, \nu_0 + \Delta\nu_{\rm th}]$ (see section 2.1.2). Hence, he neglected all possible absorption events beyond one Sobolev length and therefore underestimated the column density by a factor of 1.694 (Equation 2.12). The appropriate consideration of the overlap is very important as we have seen in section 4.2, although even the uncorrected Sobolev approximation generally overestimates column densities. Consequently, there must be further shortcoming of the Sobolev approximation.

5.1.2 Variations of Velocity Divergence and Density

The Sobolev approximation assumes the velocity divergence and the density to be constant within one Sobolev length. These simplifications avoid the evaluation of integrals along the line of sight but are formally only valid for large velocity gradients. Therefore, we should check, if this assumption of a large velocity gradient is valid and hence the velocity divergence and the density can be considered to be constant within one Sobolev length. In order to check the validity of the assumptions, we analyse several snapshots of different phases of the collapse by performing the following algorithm:

1. We select all particles above the optically thick density threshold $n \geq 10^9\,\mathrm{cm}^{-3}$ because below this density the Sobolev approximation is not applied.

2. We choose a random subset of these particles (every 100th particle, because otherwise the computational effort might be too big).
3. We loop through all chosen particles and for each “target” particle we
    a) determine the Sobolev length $L_{\rm sob}$
    b) estimate the number $N_{\rm sob}$ of all particles within this Sobolev length
    c) loop through all these particles and calculate the deviations of
        - H_2 density $n_{\rm H_2}(i)/n_{\rm H_2}(\rm target)$,
        - thermal velocity $v_{\rm th}(i)/v_{\rm th}(\rm target)$,
        - and the velocity divergence between the target particle and the individual particles within its Sobolev length. In order to compare the velocity divergence $|\vec{\nabla}\vec{v}_{\rm target}|$, we relate it to the discretised velocity gradients $|\vec{v}_{\rm target} - \vec{v}_i|/|\vec{r}_{\rm target} - \vec{r}_i|$.
    d) Finally we create a histogram, based on these deviations. The contributions of the particles are weighted by $N_{\rm sob}$, because otherwise target particles with a large Sobolev length might contribute with disproportional many particles to the histogram. Applying the weighting factor, each target particle contributes with a total count of one.

Based on different runs we verify that these histograms look qualitatively the same, regardless the time of collapse or the initial conditions. Hence, we present two histograms based on the cosmological initial conditions and the Sobolev cooling approach in Figure 5.1. If the Sobolev assumptions might be correct and the quantities are constant within one Sobolev length, the histograms should be very narrow.

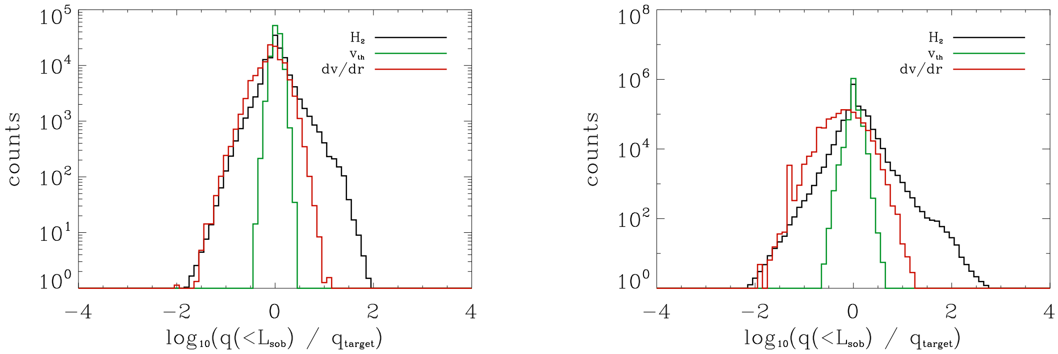

Figure 5.1: Histograms illustrating the deviations of different quantities within one Sobolev length. Based on the cosmological initial conditions at a peak density of $n_{\rm max} \approx 10^{12}\,{\rm cm^{-3}}$ (left) and shortly after formation of the first sink particle (right). The histograms show that especially the H_2 number density varies by more than a factor 100 within one Sobolev length, while the thermal velocity is tolerably constant. It is important to mention that the distributions are not symmetric because otherwise one could argue that these deviations might cancel out.

	n_{H_2}	v_{th}	$\mathrm{d}v/\mathrm{d}r$
below zero	41%	44%	63%
above zero	59%	56%	37%
mean deviation	1.13	1.04	0.76

Table 5.1: Quantification of the histogram's asymmetry (for the right histogram shortly after formation of the first sink particle).

However, H_2 number density, thermal velocity and the gradient of the velocity vary by a factor of up to one hundred. While the thermal velocity seems to be rather constant within one Sobolev length (because it scales as $v_{\mathrm{th}} \propto \sqrt{T}$), the H_2 number density varies most strongly. One should emphasise that the histograms are not symmetric and the contributions below and above zero can not just cancel out. A quantification of this asymmetry is given in Table 5.1. Although this analysis clearly shows the shortcomings of the Sobolev approximation, we should keep in mind that the "counting" of deviations between particles is biased by two effects which are illustrated in Figure 5.2.

- The number of SPH particles increases towards the centre of the cloud and therefore there are systematically more particles with higher densities or velocities.
- There is a smaller fraction of the "Sobolev volume" around a target particle closer to the cloud's centre ($19 - 50\%$) than further away from it. Assuming radially decreasing profiles of the quantities leads to unequal distributions within the Sobolev length.

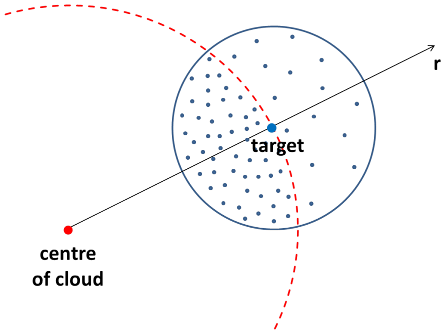

Figure 5.2: Illustration of the two effects, which bias the histograms: due to the SPH approach there is a higher particle density towards the centre of the cloud, which might overestimate their contributions to the histogram, as each particle contributes individually. On the other hand, the fraction of the "Sobolev volume" which is closer to the cloud's centre is smaller than the fraction which is farer away than the target particle.

Although these two effects might cancel out, we should be aware of them when interpreting these histograms.

5.1.3 Angular Dependence of Escape Fractions

Due to tidal forces and an initial angular momentum, the collapse does not proceed spherically symmetric. Spherical symmetry might be a valid assumption on large scales, but breaks down on length scales of star formation. Hence, the escaping photons does not see a smooth distribution of column densities, but rather an inhomogeneous distribution. Exemplary, Figure 5.3 shows the hammer projection of the column density as seen by a particle close to the centre of the cloud before the first sink particle form. In order to quantify the angular dependence of the escape fraction, we use the HEALPix maps of the opacity corrections based on the synthetic initial conditions. For each of the 48 pixels, the exact escape fraction according to the lookup method can be compared to the Sobolev-based escape fraction. The radial profile of the maximal relative deviation

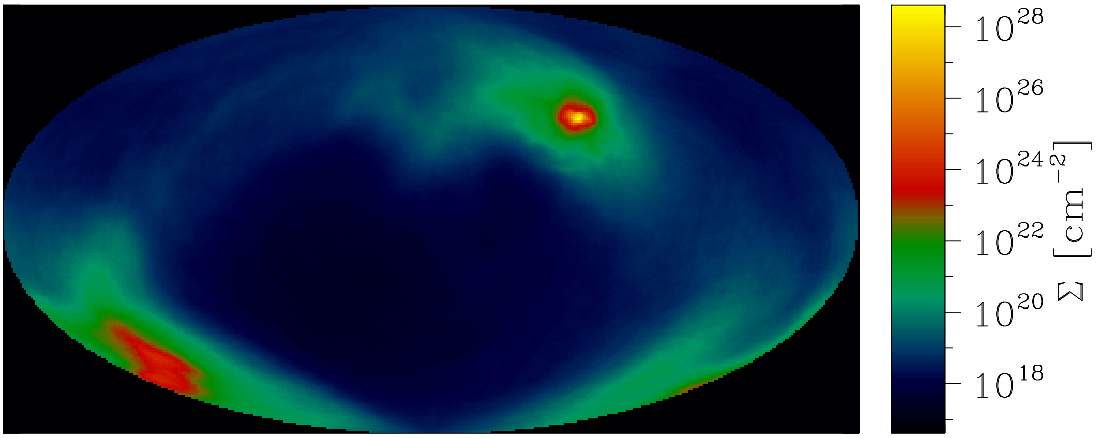

Figure 5.3: Hammer projection of column density for a particle, which is located ∼ 100AU from the cloud's centre of mass, shortly before the first sink particle forms. The distribution of column densities (and therefore photon escape fractions) is inhomogeneous and angle dependent.

$$\frac{\max_{i\in[1,48]} |\beta_{\mathrm{lookup}}(i) - \beta_{\mathrm{sob}}|}{\beta_{\mathrm{sob}}} \tag{5.1}$$

can be seen in Figure 5.4 for different times of the collapse. Especially after formation of the sink particles (bottom plots), the relative deviations are close to one in the inner ∼ 100AU. Although this figure illustrates just the maximal relative deviation, it clearly demonstrates the failing of the Sobolev approximation in modelling inhomogeneous, non-spherical density distributions. In order to verify the angular dependence of opacity correction, we analyse its spread among the HEALPix pixels for each particle individually. Therefore, we plot the radial profile of the maximal spread between the HEALPix pixels as it can be seen in Figure 5.5. Shortly before formation of the first sink particle (top right plot), the opacity corrections in the

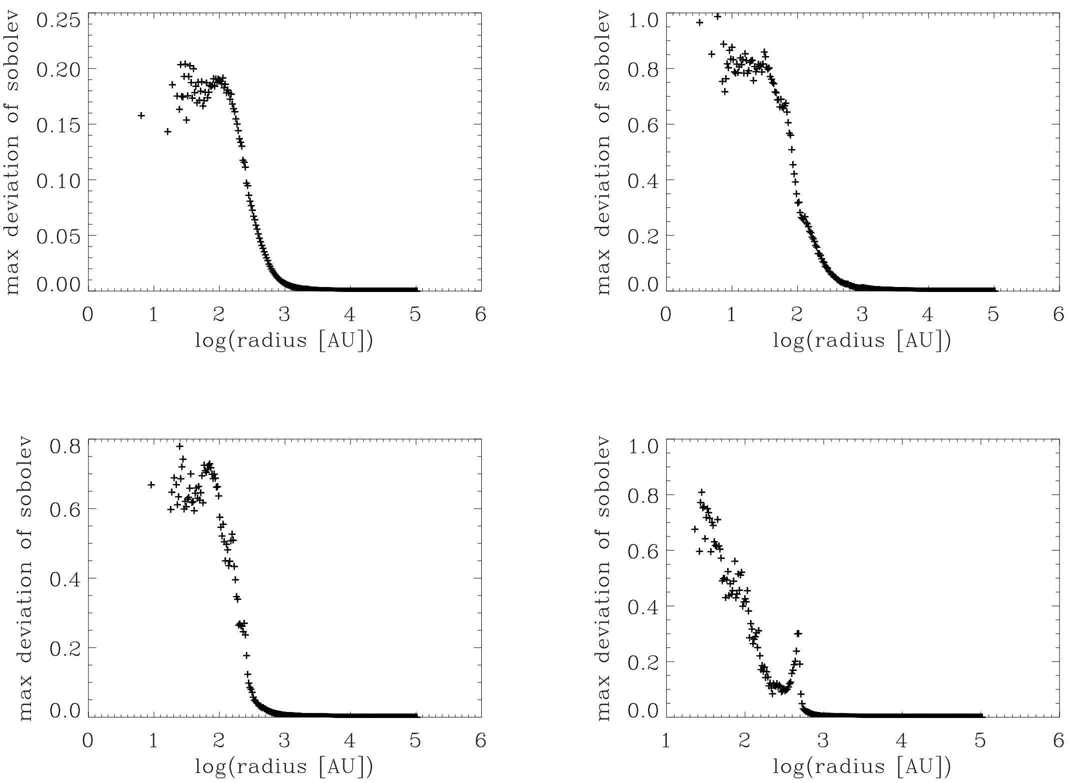

Figure 5.4: Radially binned profiles of the maximal relative deviation between the Sobolev-based opacity correction and the TreeCol-based ones. The snapshots are taken at different times of the collapse (in chronological order from top left to bottom right). For a value close to zero, all 48 pixels yield about the same opacity correction as the Sobolev approximation, whereas for a value close to one, the Sobolev approximation can not capture the very inhomogeneous distribution of the opacity correction around the particles.

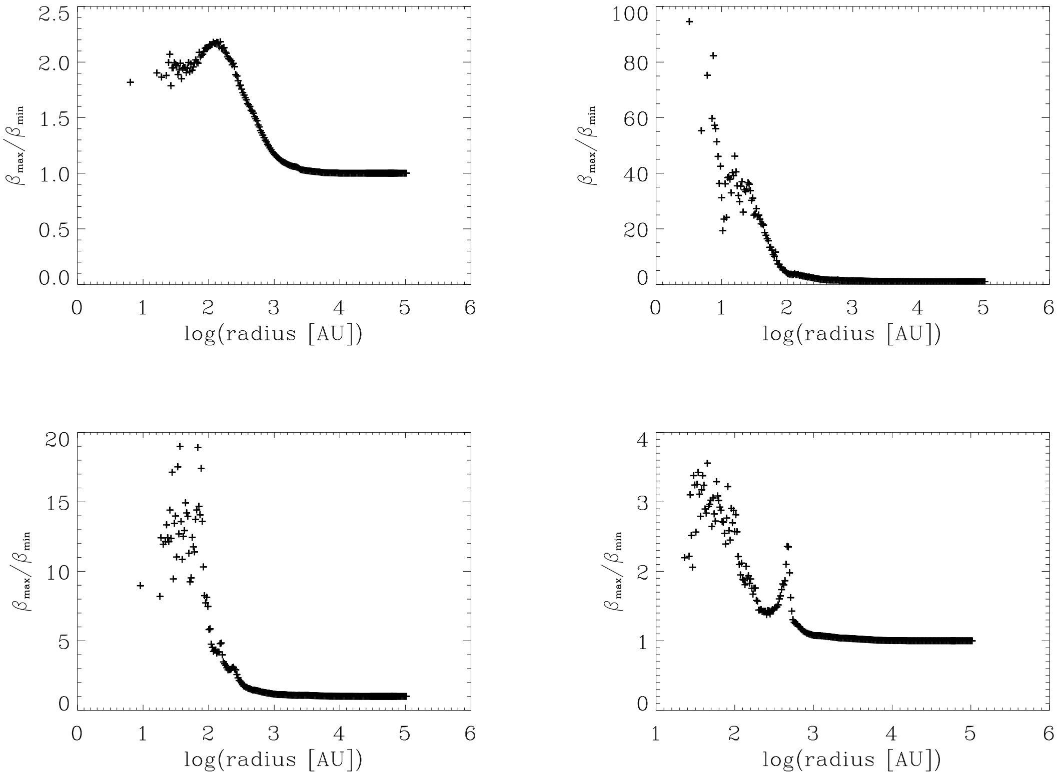

Figure 5.5: Radially binned profiles of the maximal spread of the TreeCol-based opacity corrections. The snapshots are taken at different times of the collapse (in chronological order from top left to bottom right). A value of $\beta_{\rm max}/\beta_{\rm min} = 10$ e.g. means that the opacity corrections in this radial bin vary by a factor of 10 within each HEALPix sphere for the individual particles.

inner ~ 100AU vary by factors of $10-100$. During the further collapse, this value decreases but is still between $2-20$ in the centre of the cloud. The detailed time evolution of this behaviour can be seen in Figure 5.6. The previous plots clearly illustrate that local, isotropic approximations of the column density, respectively opacity correction, have to fail and we need an improved method for the determination of effective column densities.

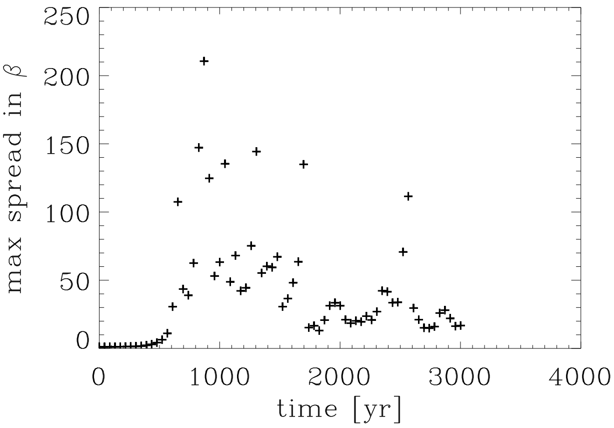

Figure 5.6: Maximal spread of the angular dependent opacity correction as a function of time (formation of the first sink particle at $t \simeq 750$yr). A value of 100 means that there is at least one particle in the simulation, whose values for the opacity correction vary by a factor of 100. Although this illustrates only the most extreme case, the previous figures support the general trend of a non-isotropic opacity correction.

Hirano & Yoshida (2013) also mention this problem during their comparison of different cooling implementations in simulations of primordial star formation. Figure 5.7 shows their plot of the effective escape probability for three orthogonal directions. The slope of the opacity correction for the three orthogonal directions is different, whereas especially the z-direction tends towards higher values. Using TreeCol, we were able to reproduce the direction dependence of the opacity correction but with a better angular resolution. Interestingly, we find a different trend regarding the magnitude of opacity correction. While Hirano & Yoshida (2013) say that "using an isotropic approximation for optically thick H_2 line cooling overestimates the net cooling rate", we find out that an isotropic approximation underestimates the optically thick cooling rate.

5.1.4 Accretion Disc

Since we have seen the effects of a non-spherical collapse (angular dependency of opacity correction), we want to understand and determine the deviations from spherical symmetry. A first qualitative insight into the processes which occur during the collapse is given by Figure 5.8. This is a sequence of snapshots from a movie, illus-

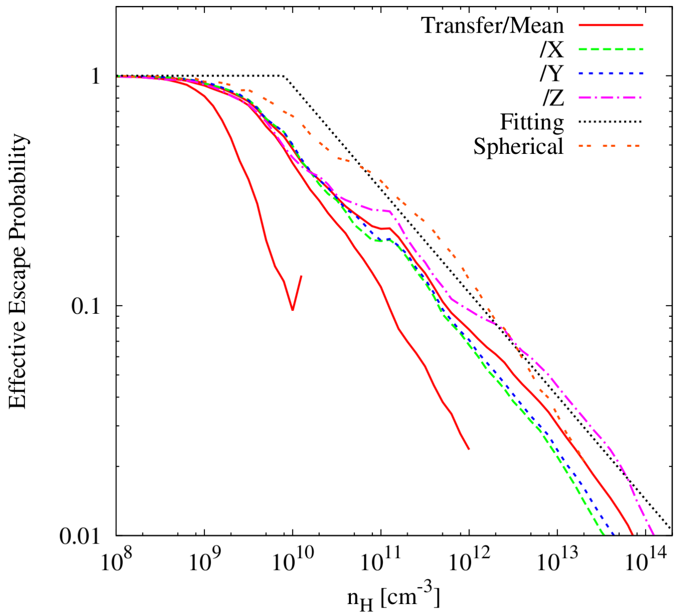

Figure 5.7: Opacity correction as a function of density. The long-dashed, short-dashed, and dot-dashed lines show the three orthogonal components (x, y, and z) when the central density is $n_{\max} = 10^{14}\,\mathrm{cm}^{-3}$. The solid lines show the evolution of the direction-averaged mean value at $n_{\max} = 10^{10}, 10^{12}$ and $10^{14}\,\mathrm{cm}^{-3}$. Adopted from Hirano & Yoshida (2013).

trating the collapse of the cloud based on synthetic initial conditions. The sequence shows the rotation of the central 665AU at the point where 6 sink particles were already formed. The accretion disc is a very prominent feature, which has formed during the collapse and all sink particles lie roughly in this disc. According to Smith et al. (2011), the disc-like structure is a typical feature due to the inability of the halo to transfer angular momentum outwards quickly enough. Hence, it should be clear that the photon escape fraction is enhanced perpendicular to that disc, whereas the medium is optically thick in the disc plane. A local, isotropic column density estimation can not capture this feature and therefore generally underestimates the photon escape probability.

In order to identify the disc and to quantify the ellipticity of the collapsing cloud, we use several methods. The most promising one that was able to capture this trend is the estimation of the ellipticity

$$\epsilon = \frac{a-b}{a}, \tag{5.2}$$

where a is the major and b is the minor axis of the ellipsoid that is generated when we cut out all gas above the optically thick density threshold $n \geq 10^9\,\mathrm{cm}^{-3}$. The time evolution of the ellipticity can be seen in Figure 5.9. While a value of $\epsilon = 0$ might correspond to a spherical cloud, a value of $\epsilon = 0.5$ characterises a cloud whose longest cross section is twice as long as any perpendicular cross section. Hence, we

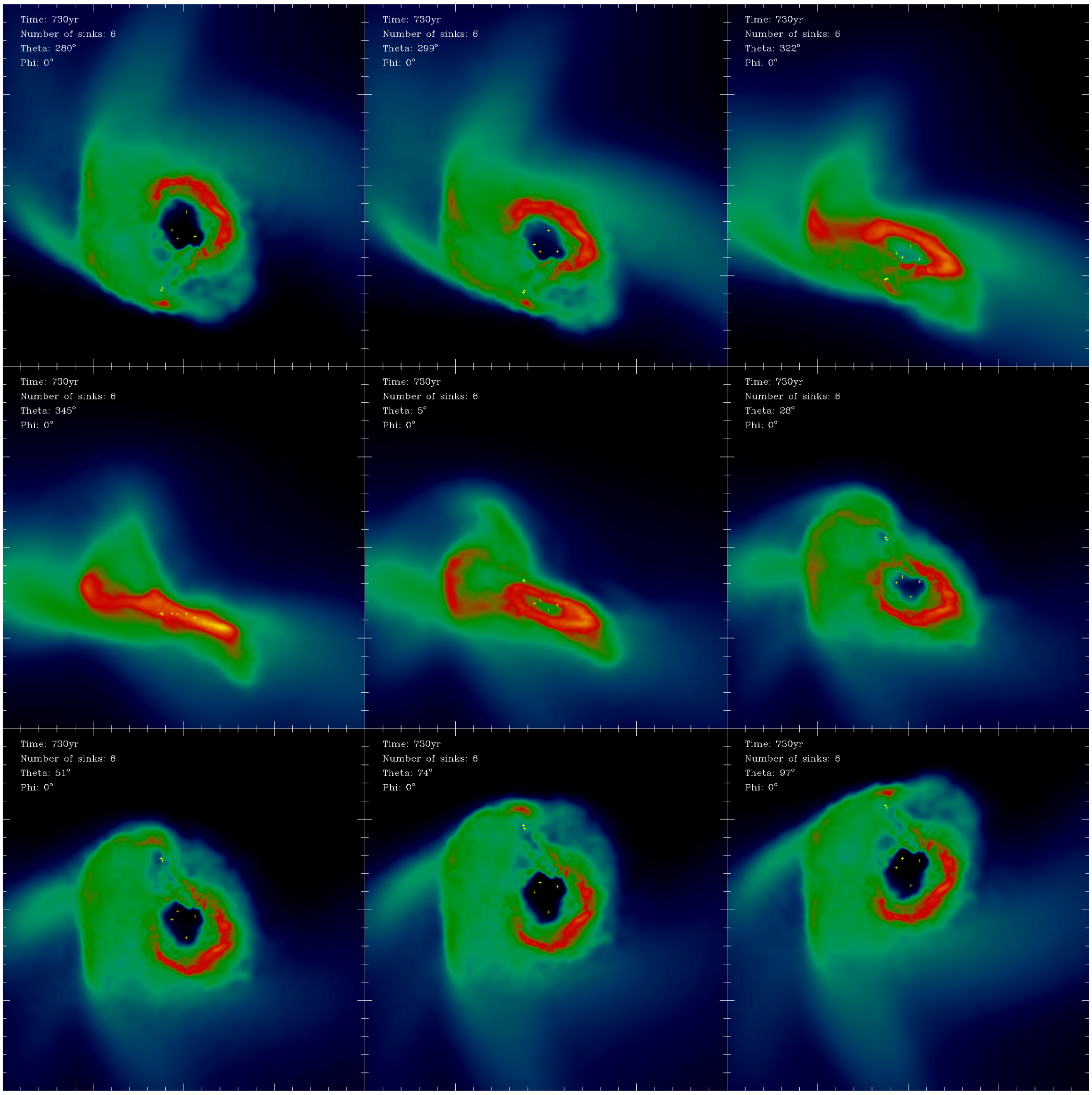

Figure 5.8: Sequence of snapshots illustrating the rotation of the central 665AU (6 sink particles have formed). The colour indicates the density projection and the yellow crosses mark the positions of sink particles. One clearly sees the accretion disc, which has formed and the sink particles lie roughly in this plane.

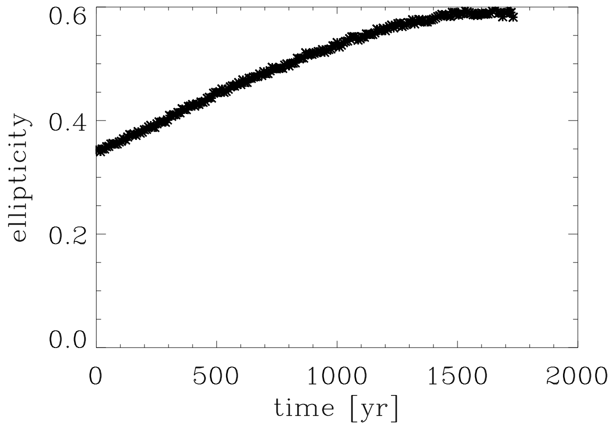

Figure 5.9: Time evolution of the ellipticity for all gas above $n \geq 10^9\,\mathrm{cm}^{-3}$. The simulation is based on synthetic initial conditions and the first sink particle form at $t = 0$. The trend towards higher ellipticities indicates the formation of a disc-like structure.

clearly see the trend of an accretion disc that forms during the collapse of the cloud.

5.2 So Which Method to Use?

A main topic of this Master Thesis is the comparison of different cooling implementations for simulations of primordial star formation. Basically, we can distinguish these methods between those which depend on local properties of the gas and those which determine the effective column densities based on TreeCol. Although the TreeCol-based methods are computationally expensive and slow down the code, we clearly recommend the lookup approach, because it captures the whole collapse of the cloud properly and takes the true line overlaps into account. Regarding the local methods, there is no general answer to this question. Most of these methods assume spherical symmetry and hence their validity breaks down, when a disc forms around the protostars. Since primordial star formation lasts for several thousand years, while we only capture the first hundred years in our simulations, one should use an approach which yields a suitable long-time accuracy. The reciprocal method is the only approach that considers both gradients in density and a spatially varying velocity divergence. Therefore, this method is the most accurate approach for the determination of the effective column density even after subsequent sink particle formation. Whether one uses the corrected or uncorrected reciprocal method seems to be of minor relevance, because whereas the corrected reciprocal method yields more accurate results around the formation of the first sink particle, both methods approximately yield the same results for later stages of the collapse. The two analytical fits might be useful during the collapse of the primordial cloud, but also fail when the disc-like structure starts to form. The commonly used Sobolev method generally overestimates column density and hence underestimates the photon escape fraction. In our simulations, this leads to higher temperatures in the centre of the cloud, less fragmentation and higher masses of the protostars.

5.3 Mergers

The possibility of merging is crucial for a complete theory of star formation, since mergers of protostars do shift the IMF towards higher masses. Pop III protostars are likely to merge during their dynamical formation and subsequent accretion process, because they are large, fluffy objects. Close encounters might either eject at least one star to higher orbits or merge both protostars. According to Greif et al. (2012) and Stacy & Bromm (2013) more than half of the protostars are lost to mergers. Since we have not implemented possible merging in the code, we should at least afterwards try to constrain the possibility of merging events in our simulation. Therefore, we first constrain the protostellar radii using Equation 1.48 and compare it to the spatial separation of the sink particles (see Figure 5.10). Throughout the simulation, the distances between sink particles are larger than their protostellar radii, but as Pop III protostars are large, fluffy objects, they might merge nevertheless. Following Greif et al. (2012), a valid criterion for possible merging is the comparison of the minimum separation of two sink particles to the sum of their protostellar radius at this time (see Figure 5.11). Although the protostars in our simulation seem to be separated sufficiently far enough, we should keep in mind that we only follow the first ~ 200 years, whereas Greif et al. (2012) follows the protostellar evolution for ~ 1000 years after formation of the first protostar.

5.4 Fragmentation Behaviour

Fragmentation is a highly chaotic process and slight changes in the initial conditions or in the implementation of the governing physics can completely change the outcome. Therefore, solely the number of sink particles is not a valid quantification, since we do not have enough realisations for any statistical significance. Nevertheless, we determine and compare different fragmentation criteria for the individual cooling approaches and find out that the lookup method promotes fragmentation according to all criteria. In other words, commonly used cooling approximations generally underestimate the number of Pop III stars and therefore overestimate their mass. Moreover, we have to notice that the disc is just about to form, when we end our simulations. Therefore, the differences between the individual cooling approaches and their effect on fragmentation might even be more pronounced for later stages of the collapse. In any case, we expect more Pop III stars with lower masses than previously expected.

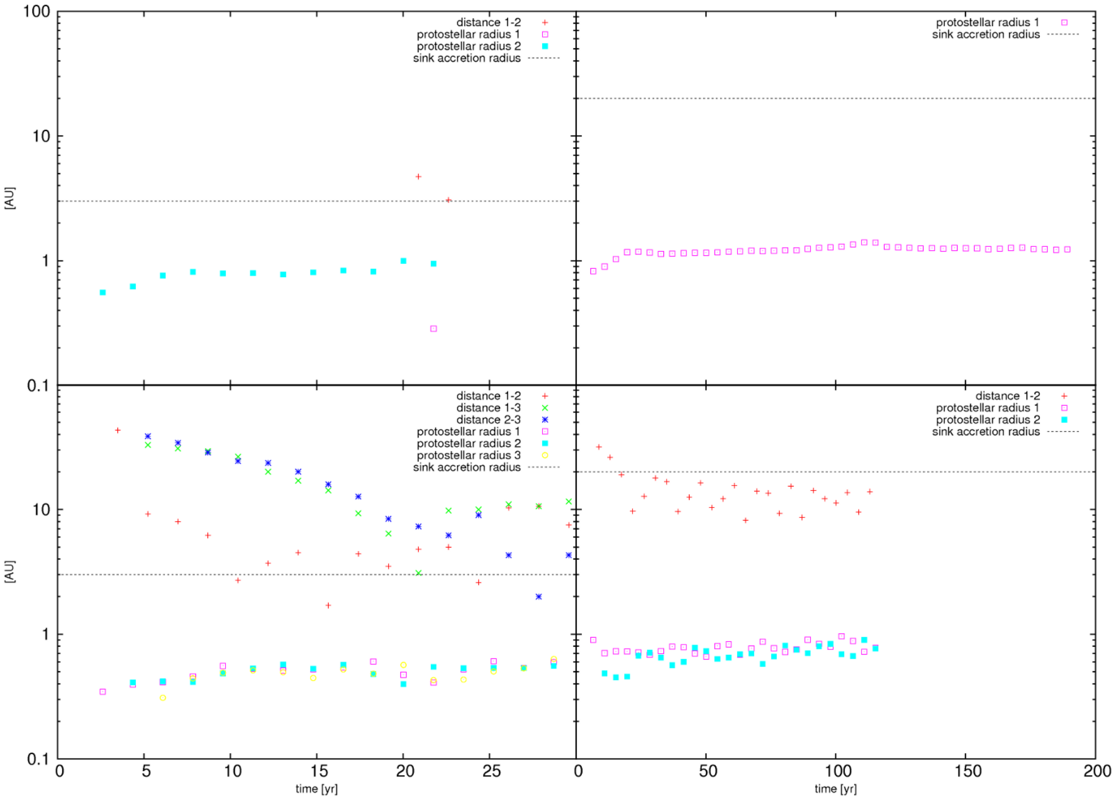

Figure 5.10: Protostellar radii, distances between sink particles, and accretion radii of the sink particles as a function of time for the runs based on the cosmological initial condition. Top: Sobolev approximation. Bottom: lookup method. Left: $r_{\mathrm{acc}} = 3\mathrm{AU}$. Right: $r_{\mathrm{acc}} = 20\mathrm{AU}$. Although the protostellar radius seems to be smaller than the distance all the time, the distance between sink particles might become smaller than the accretion radius of the sink particle.

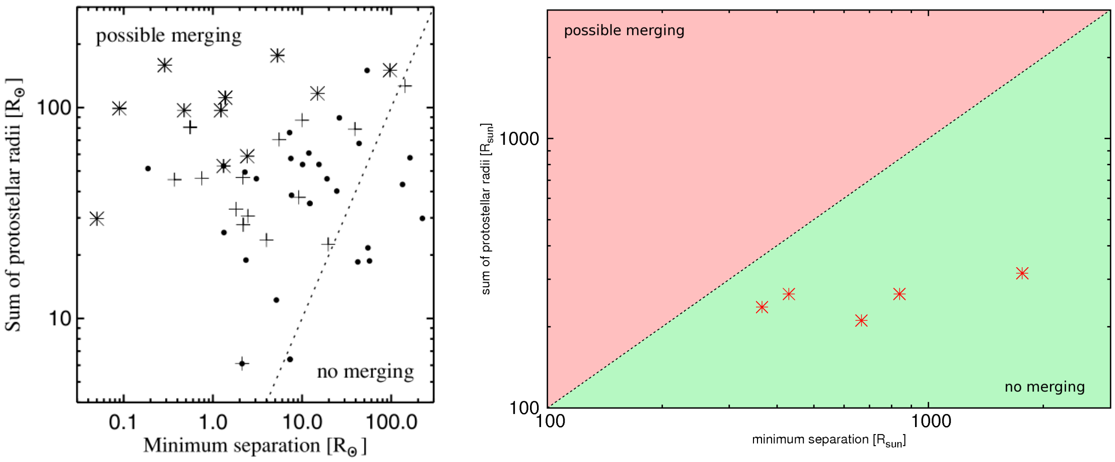

Figure 5.11: Comparison of the minimum separation of each protostar to any other protostar with the sum of the protostellar radii during their closest encounter. Left: plot by Greif et al. (2012) indicating different protostellar masses with different symbols. Almost all protostars experience a possible merging event. Right: data from our simulations based on initial conditions. No protostar experiences a merging event.

5.5 Caveats

There are several open questions, shortcomings and approximations, which one should keep in mind, when interpreting the previously presented results. First of all, our analysis is suffering from a low statistical evidence. All results are based on two realisations of the synthetic initial condition on one set of cosmological initial conditions. Although we run several simulations for each set of initial conditions, statistical statements must be treated with caution and we can not be sure, whether our initial clouds where representative or by some means biased.

Since we follow the fragmentation of the cloud only for the first ∼ 100yr after formation of the first protostar, we miss information about the physical conditions thereafter. Although we only capture a small fraction of the whole star formation process, it is likely that the disc-like structure will proceed to grow and most of our statements remain valid.

Computer simulations are only models for the real physical processes. The approximations, on which these models are based, are mostly valid under the given conditions. However, there are some crucial points regarding the accuracy and completeness of our simulation:

- We do not account for mergers, whereas they seem not to be relevant on the timescales we consider.
- The protostellar model assumes a constant accretion rate and does not include the effects of ionising radiation.
- High uncertainty for the value of several rate coefficients see section 1.3.1.

- No magnetic field, which might influence the collapse (for a detailed discussion of the effects of magnetic fields in primordial star formation see Machida & Doi (2013) and references therein).

Besides, we should also keep in mind that the escape probability, as the theoretical basis for our cooling implementation, is an approximation by itself (e.g. we use one average escape fraction for all photons, instead of determining the individual escape probabilities for each line separately).

5.6 Conclusion

Since H_2 is the dominant coolant in primordial gas clouds, line cooling by molecular hydrogen is a crucial process in the formation of Pop III stars. While the cooling rates in the optically thin regime can be calculated accurately, optically thick cooling is only poorly understood, although it basically influences the temperature profile and fragmentation of the cloud. The commonly used Sobolev approximation has to be corrected for the effect of line overlap. However, since the Sobolev and other approximations of the effective column density assume isotropy and certain quantities to be constant, they all fail in reflecting the actual shape of the cloud. While the cloud flattens and develops a disc during the collapse, the local column density approaches generally yield too small values for the photon escape fraction (mean relative errors of 20%). Only the TreeCol-based methods are able to capture this dynamical feature and consequently yield lower temperatures in the centre of the cloud. Merely a newly invented combination of the Sobolev and Gnedin approximation might reproduce accurate values for the opacity correction, also at later stages of the collapse.

Primordial gas is most susceptible to fragmentation in the density regime from $n = 10^{10}\,\mathrm{cm}^{-3}$ to $n = 10^{12}\,\mathrm{cm}^{-3}$. Whereas local methods tend to suppress fragmentation and result in the creation of few high-mass Pop III stars, the TreeCol-based methods promote fragmentation and therefore cause the creation of more lower-mass stars. Regardless the cooling implementation, the protostars have very high mass accretion rates and the mass function is dominated by high-mass stars.

Part I

Appendix

A Acknowledgements

My studies and the writing of this Master Thesis would not have been possible without the help of many people, whom I would like to thank.

In the first place I want to thank my supervisor Ralf Klessen. In his formative lecture “Theoretical Astrophysics” he strengthened my enthusiasm for this subject. Moreover, he offered me the topic for this thesis and supported my work with a lot of helpful comments and ideas, but however encouraged me to realise my own ideas. In addition, he made it possible for me to join two very interesting astronomical conferences, for what I am very grateful.

Special thanks go to Paul Clark and Simon Glover, from whom I learned a lot about ISM chemistry, primordial star formation, computer simulations, and scientific writing. Besides their informative lectures “Chemistry of the ISM” and “Dark Ages of the Universe”, they helped me to get the code running, answered all my questions, and they supported my work with a lot of helpful discussions and valuable suggestions.

Dominik Schleicher invited me to present my Master project at the university of Göttingen. Hence, I want to thank him and his group for this possibility, interesting discussions, new ideas, and helpful comments.

I thank my office mates Adriana, Carsten, Clio, Roxana, and Sebastian for the enjoyable working (and especially non-working) atmosphere. Special thanks got to Clio, who was my “fellow-sufferer” during this Master project and supported me with a lot of helpful discussions and constructive criticism.

Moreover, I highly appreciate the atmosphere at the institute and the helpful inputs by the members of the star formation group. Especially by Mei, who provided me with the cosmological initial conditions.

Besides all the scientific support, I certainly want to thank my friends (especially Anne and Chris) and family for all the help, affirmation, and support in the last years and especially during the past few weeks. Moreover, I want to thank my Liberian friend Wilfred for not only sharing the common utopia to improve the world by education, but also for collectively realising the teacher workshop projects.

Finally I want to thank Anne, Carsten, Clio, Babsi, Jana, Judith, Mei, and Moritz for cross-reading parts of my Master Thesis and providing me with helpful corrections and ideas of improvement.

B Positions of Protostars

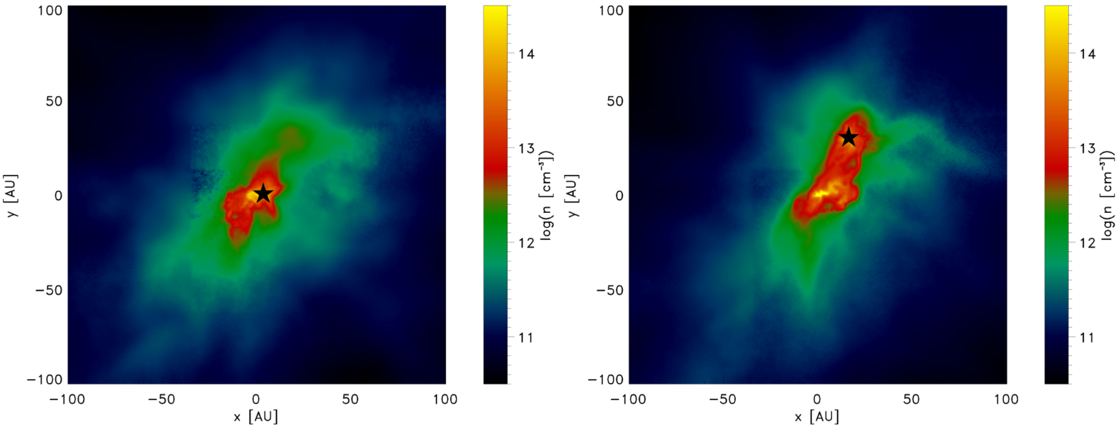

Figure B.1: Positions of sink particles for snapshot d. The size of the protostars correspond to an accretion radius of $r_{\mathrm{acc}} = 3\mathrm{AU}$. Left: Sobolev. Right: lookup.

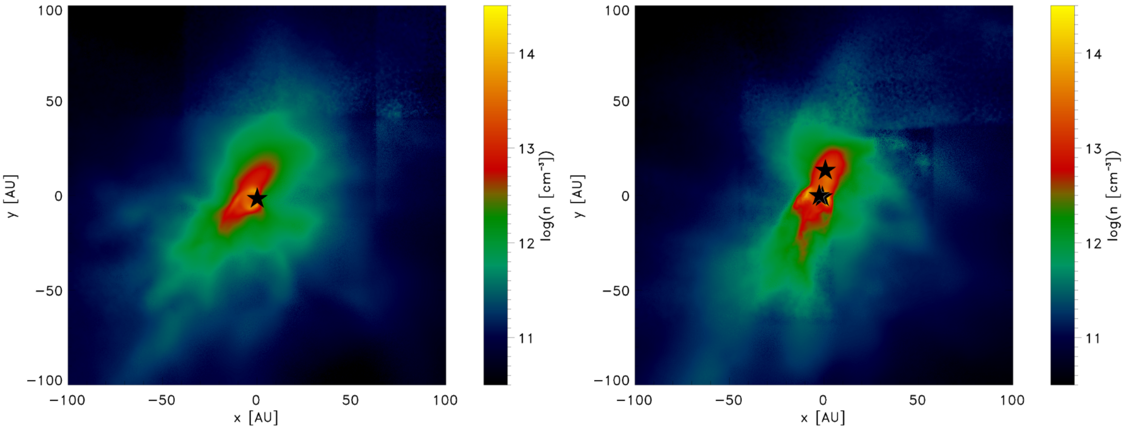

Figure B.2: Positions of sink particles for snapshot e. The size of the protostars correspond to an accretion radius of $r_{\mathrm{acc}} = 3\mathrm{AU}$. Left: Sobolev. Right: lookup.

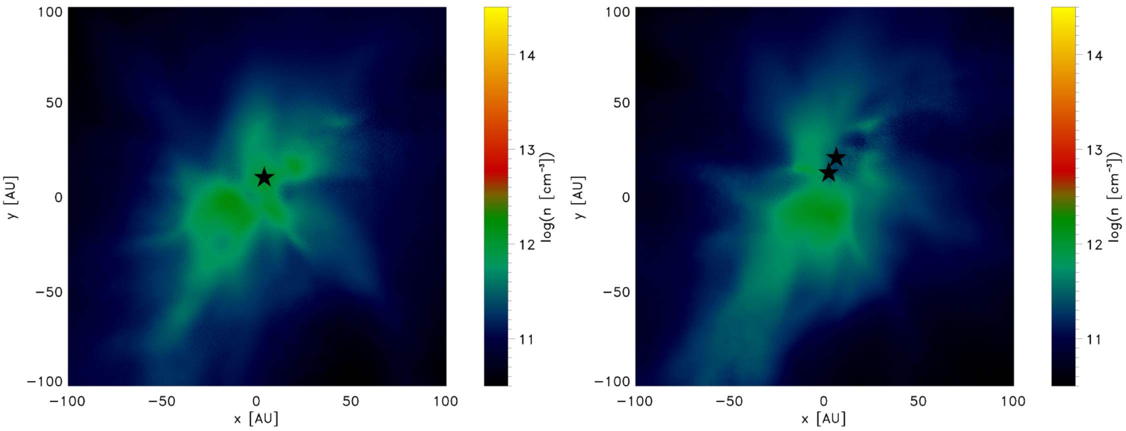

Figure B.3: Positions of sink particles for snapshot f. The size of the protostars correspond to an accretion radius of $r_{\mathrm{acc}} = 3\mathrm{AU}$. Left: Sobolev. Right: lookup.

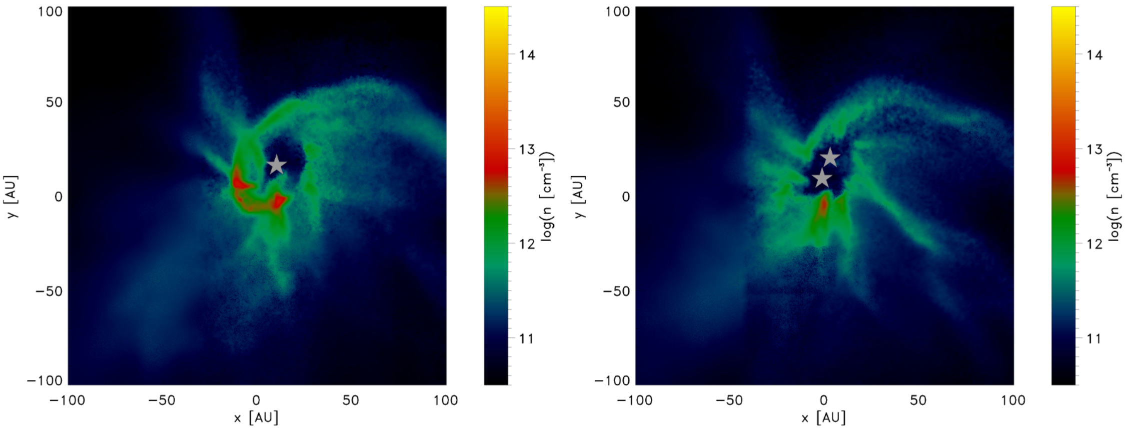

Figure B.4: Positions of sink particles for snapshot g. The size of the protostars correspond to an accretion radius of $r_{\mathrm{acc}} = 3\mathrm{AU}$. Left: Sobolev. Right: lookup.

C Lists

List of Figures

List of Tables

Bibliography

Abel, T., Anninos, P., Norman, M. L., & Zhang, Y. 1998, Astrophys. J. , 508, 518

Abel, T., Anninos, P., Zhang, Y., & Norman, M. L. 1997, New Astron., 2, 181

Abel, T., Bryan, G. L., & Norman, M. L. 2000, Astrophys. J. , 540, 39

—. 2002, Science, 295, 93

Ambartsumian, V. A. 1933, Izvestiya Glavnoj Astronomicheskoj Observatorii v Pulkove, 13

Anninos, P., Zhang, Y., Abel, T., & Norman, M. L. 1997, Nature, 2, 209

Avila-Reese, V. 2006, ArXiv Astrophysics e-prints, astro-ph/0605212

Barkana, R., & Loeb, A. 2001, Physics Reports, 349, 125

Barnes, J. E., & Hut, P. 1989, Astrophys. J. Suppl. Series, 70, 389

Bartelmann, M. 2007, Lecture Notes "Cosmology"

—. 2009, Lecture Notes "General Relativity"

Bate, M. R., Bonnell, I. A., & Price, N. M. 1995, Monthly Notices Roy. Astron. Soc. , 277, 362

Bate, M. R., & Burkert, A. 1997, Monthly Notices Roy. Astron. Soc. , 288, 1060

Benz, W. 1990, in Numerical Modelling of Nonlinear Stellar Pulsations Problems and Prospects, ed. J. R. Buchler, 269

Bergin, E. A., & Tafalla, M. 2007, Ann. Rev. Astron. Astrophys. , 45, 339

Bond, J. R., Cole, S., Efstathiou, G., & Kaiser, N. 1991, Astrophys. J. , 379, 440

Boss, A. P. 1987, Astrophys. J. , 316, 721

—. 1989, Astrophys. J. , 345, 554

Boss, A. P., & Black, D. C. 1982, Astrophys. J. , 258, 270

Bromm, V. 2013, Reports on Progress in Physics, 76, 112901

Bromm, V., Coppi, P. S., & Larson, R. B. 1999, Astrophys. J. Lett. , 527, L5

—. 2002, Astrophys. J. , 564, 23

Bromm, V., Kudritzki, R. P., & Loeb, A. 2001, Astrophys. J. , 552, 464

Bromm, V., & Larson, R. B. 2004, Ann. Rev. Astron. Astrophys. , 42, 79

Bromm, V., Yoshida, N., Hernquist, L., & McKee, C. F. 2009, Nature, 459, 49

Bujarrabal, V., Guibert, J., Nguyen-Q-Rieu, & Omont, A. 1980, Astron. and Astrophys. , 84, 311

Caffau, E., Bonifacio, P., François, P., et al. 2011, Nature, 477, 67

Carlberg, R. G. 1981, Monthly Notices Roy. Astron. Soc. , 197, 1021

Carr, B. J., Bond, J. R., & Arnett, W. D. 1984, Astrophys. J. , 277, 445

Castor, J. I. 1970, Monthly Notices Roy. Astron. Soc. , 149, 111

Chabrier, G. 2003, The Publications of the Astronomical Society of the Pacific, 115, 763

Christlieb, N., Bessell, M. S., Beers, T. C., et al. 2002, Nature, 419, 904

Clark, P. C., & Glover, S. C. O. 2013, Lecture Notes "The Dark Ages of the Universe"

Clark, P. C., Glover, S. C. O., & Klessen, R. S. 2008, Astrophys. J. , 672, 757

—. 2012, Monthly Notices Roy. Astron. Soc. , 420, 745

Clark, P. C., Glover, S. C. O., Klessen, R. S., & Bromm, V. 2011a, Astrophys. J. , 727, 110

Clark, P. C., Glover, S. C. O., Smith, R. J., et al. 2011b, Science, 331, 1040

Couchman, H. M. P., & Rees, M. J. 1986, Monthly Notices Roy. Astron. Soc. , 221, 53

Courant, R., Friedrichs, K., & Lewy, H. 1928, Mathematische Annalen, 100, 32

de Jong, T., Dalgarno, A., & Chu, S.-I. 1975, Astrophys. J. , 199, 69

Dullemond, C. P. 2013, Lecture Notes "Radiative transfer in astrophysics"

Elitzur, M., ed. 1992, Astrophysics and Space Science Library, Vol. 170, Astronomical masers

Emerson, D. 1996, Interpreting Astronomical Spectra

ESA and the Planck Collaboration. 2013, Best Map Ever of the Universe

Federrath, C., Banerjee, R., Clark, P. C., & Klessen, R. S. 2010, Astrophys. J. , 713, 269

Frebel, A., Aoki, W., Christlieb, N., et al. 2005, Nature, 434, 871

Frommhold, L. 1993, Collision-Induced Absorption in Gases (Cambridge: Cambridge University Press)

Galli, D., & Palla, F. 1998, Astron. and Astrophys. , 335, 403

Gammie, C. F. 2001, Astrophys. J. , 553, 174

Gingold, R. A., & Monaghan, J. J. 1977, Monthly Notices Roy. Astron. Soc. , 181, 375

Glover, S. 2000, in The First Stars, ed. A. Weiss, T. G. Abel, & V. Hill, 261

Glover, S. 2005, Space Science Reviews, 117, 445

Glover, S. 2013, in Astrophysics and Space Science Library, Vol. 396, Astrophysics and Space Science Library, ed. T. Wiklind, B. Mobasher, & V. Bromm, 103

Glover, S., Mac Low, M.-M., Smith, M. D., Rosen, A., & Pavlovski, G. 2003, in SFChem 2002: Chemistry as a Diagnostic of Star Formation, ed. C. L. Curry & M. Fich, 296

Glover, S. C. O., & Abel, T. 2008, Monthly Notices Roy. Astron. Soc. , 388, 1627

Glover, S. C. O., & Brand, P. W. J. L. 2003, Monthly Notices Roy. Astron. Soc. , 340, 210

Glover, S. C. O., Clark, P. C., Greif, T. H., et al. 2008, in IAU Symposium, Vol. 255, IAU Symposium, ed. L. K. Hunt, S. C. Madden, & R. Schneider, 3–17

Glover, S. C. O., & Jappsen, A.-K. 2007, Astrophys. J. , 666, 1

Glover, S. C. O., & Savin, D. W. 2009, Monthly Notices Roy. Astron. Soc. , 393, 911

Gnedin, N. Y., Kravtsov, A. V., & Chen, H.-W. 2008, Astrophys. J. , 672, 765

Gnedin, N. Y., Tassis, K., & Kravtsov, A. V. 2009, Astrophys. J. , 697, 55

Goldreich, P., & Kwan, J. 1974, Astrophys. J. , 189, 441

Goldreich, P., & Lynden-Bell, D. 1965, Monthly Notices Roy. Astron. Soc. , 130, 125

Górski, K. M., Hivon, E., Banday, A. J., et al. 2005, Astrophys. J. , 622, 759

Greif, T. H., Bromm, V., Clark, P. C., et al. 2012, Monthly Notices Roy. Astron. Soc. , 424, 399

Greif, T. H., Johnson, J. L., Klessen, R. S., & Bromm, V. 2008, Monthly Notices Roy. Astron. Soc. , 387, 1021

Greif, T. H., Springel, V., & Bromm, V. 2013, Monthly Notices Roy. Astron. Soc. , 434, 3408

Greif, T. H., Springel, V., White, S. D. M., et al. 2011, Astrophys. J. , 737, 75

Haardt, F., Ripamonti, E., Colpi, M., & Ferrara, A. 2002, Astrophys. and Space Science, 281, 479

Haiman, Z., Rees, M. J., & Loeb, A. 1996, Astrophys. J. , 467, 522

Hirano, S., Hosokawa, T., Yoshida, N., et al. 2013, ArXiv e-prints, arXiv:1308.4456

Hirano, S., & Yoshida, N. 2013, Astrophys. J. , 763, 52

Hirasawa, T. 1969, Progress of Theoretical Physics, 42, 523

Hollenbach, D., & McKee, C. F. 1979, Astrophys. J. Suppl. Series, 41, 555

Hosokawa, T., Omukai, K., Yoshida, N., & Yorke, H. W. 2011, Science, 334, 1250

Hosokawa, T., Omukai, K., Yoshida, N., & Yorke, H. W. 2012, in American Institute of Physics Conference Series, Vol. 1480, American Institute of Physics Conference Series, ed. M. Umemura & K. Omukai, 91–96

Hummer, D. G., & Rybicki, G. B. 1982, Astrophys. J. , 254, 767

—. 1992, Astrophys. J. , 387, 248

Hutchins, J. B. 1976, Astrophys. J. , 205, 103

Jappsen, A.-K., Klessen, R. S., Larson, R. B., Li, Y., & Mac Low, M.-M. 2005, Astron. and Astrophys. , 435, 611

Johnson, J. L., & Bromm, V. 2006, Monthly Notices Roy. Astron. Soc. , 366, 247

Kashlinsky, A., & Rees, M. J. 1983, Monthly Notices Roy. Astron. Soc. , 205, 955

Klessen, R. S. 2002, Presentation “Lecture on SPH Basics” held at the EU Network Conference “Numerical Modelling of Young Star Clusters” in Cardiff, Wales

Klessen, R. S. 2011, in EAS Publications Series, Vol. 51, EAS Publications Series, ed. C. Charbonnel & T. Montmerle, 133–167

Kogure, T., & Leung, K.-C. 2007, in Astronomical Society of the Pacific Conference Series, Vol. 362, The Seventh Pacific Rim Conference on Stellar Astrophysics, ed. Y. W. Kang, H.-W. Lee, K.-C. Leung, & K.-S. Cheng, 260

Krumholz, M. R., & McKee, C. F. 2008, Nature, 451, 1082

Landau, L. D., & Lifshits, E. M. 1987, Fluid mechanics (Oxford, England; New York: Pergamon Press)

Larson, R. B. 1969, Monthly Notices Roy. Astron. Soc. , 145, 271

Latif, M. A., Schleicher, D. R. G., Schmidt, W., & Niemeyer, J. C. 2013a, Monthly Notices Roy. Astron. Soc. , 433, 1607

—. 2013b, Monthly Notices Roy. Astron. Soc. , 436, 2989

Le Bourlot, J., Pineau des Forêts, G., & Flower, D. R. 1999, Monthly Notices Roy. Astron. Soc. , 305, 802

Lockett, P., & Elitzur, M. 1989, Astrophys. J. , 344, 525

Lucy, L. B. 1971, Astrophys. J. , 163, 95

—. 1977, Astron. J., 82, 1013

Machida, M. N., & Doi, K. 2013, Monthly Notices Roy. Astron. Soc. , 435, 3283

Matsuda, T., Satō, H., & Takeda, H. 1969, Progress of Theoretical Physics, 42, 219

McKee, C. F., & Tan, J. C. 2008, Astrophys. J. , 681, 771

Molaro, P. 2008, in Astronomical Society of the Pacific Conference Series, Vol. 390, Pathways Through an Eclectic Universe, ed. J. H. Knapen, T. J. Mahoney, & A. Vazdekis, 472

Monaghan, J. J., & Lattanzio, J. C. 1985, Astron. and Astrophys. , 149, 135

Neufeld, D. A., & Kaufman, M. J. 1993, Astrophys. J. , 418, 263

Ohkubo, T., Nomoto, K., Umeda, H., Yoshida, N., & Tsuruta, S. 2009, Astrophys. J. , 706, 1184

Omukai, K., & Nishi, R. 1998, Astrophys. J. , 508, 141

Omukai, K., & Palla, F. 2001, Astrophys. J. , 561, L55

—. 2003, Astrophys. J. , 589, 677

Omukai, K., Tsuribe, T., Schneider, R., & Ferrara, A. 2005, Astrophys. J. , 626, 627

Omukai, K., & Yoshii, Y. 2003, Astrophys. J. , 599, 746

O'Shea, B. W., & Norman, M. L. 2006, Astrophys. J. , 648, 31

—. 2007, Astrophys. J. , 654, 66

Palla, F., Salpeter, E. E., & Stahler, S. W. 1983, Astrophys. J. , 271, 632

Peebles, P. J. E., & Dicke, R. H. 1968, Astrophys. J. , 154, 891

Penston, M. V. 1969, Monthly Notices Roy. Astron. Soc. , 144, 425

Peters, T., Klessen, R. S., Mac Low, M.-M., & Banerjee, R. 2010, Astrophys. J. , 725, 134

Press, W. H., & Schechter, P. 1974, Astrophys. J. , 187, 425

Quinn, T., Katz, N., Stadel, J., & Lake, G. 1997, ArXiv Astrophysics e-prints, astro-ph/9710043

Ripamonti, E., & Abel, T. 2004, Monthly Notices Roy. Astron. Soc. , 348, 1019

Ripamonti, E., Haardt, F., Ferrara, A., & Colpi, M. 2002, Monthly Notices Roy. Astron. Soc. , 334, 401

Sabano, Y., & Yoshii, Y. 1977, Publ. of the Astron. Soc. of Japan, 29, 207

Saslaw, W. C., & Zipoy, D. 1967, Nature, 216, 976

Schaerer, D. 2002, Astron. and Astrophys. , 382, 28

Schleicher, D. R. G., Banerjee, R., & Klessen, R. S. 2008a, Physical Review D, 78, 083005

Schleicher, D. R. G., Galli, D., Palla, F., et al. 2008b, Astron. and Astrophys. , 490, 521

Schleicher, D. R. G., Palla, F., Ferrara, A., Galli, D., & Latif, M. 2013, Astron. and Astrophys. , 558, A59

SDSS. 2008, Online Material: SDSS Legacy Survey (http://www.sdss.org/legacy/)

Silk, J. 1977, Astrophys. J. , 211, 638

—. 1983, Monthly Notices Roy. Astron. Soc. , 205, 705

Smith, R. J., Glover, S. C. O., Clark, P. C., Greif, T., & Klessen, R. S. 2011, Monthly Notices Roy. Astron. Soc. , 414, 3633

Sobolev, V. V. 1947, The Moving Envelopes of the Stars (in Russian) (Leningrad, Russia: Leningrad State Univ. Press)

—. 1957, Soviet Astronomy, 1, 678

—. 1960, Moving envelopes of stars (Cambridge: Cambridge: Harvard University Press)

Solomon, P. M. 1965, PhD thesis, The University of Wisconsin - Madison.

Springel, V. 2005, Monthly Notices Roy. Astron. Soc. , 364, 1105

—. 2010, Monthly Notices Roy. Astron. Soc. , 401, 791

Stacy, A., & Bromm, V. 2013, Monthly Notices Roy. Astron. Soc. , 433, 1094

Stacy, A., Greif, T. H., Klessen, R. S., Bromm, V., & Loeb, A. 2013, Monthly Notices Roy. Astron. Soc. , 431, 1470

Stahler, S. W., & Palla, F. 2005, The Formation of Stars

Stahler, S. W., Palla, F., & Salpeter, E. E. 1986, Astrophys. J. , 302, 590

Stancil, P. C., Lepp, S., & Dalgarno, A. 1998, Astrophys. J. , 509, 1

Stecher, T. P., & Williams, D. A. 1967, Astrophys. J. Lett. , 149, L29

Takeda, H., Satō, H., & Matsuda, T. 1969, Progress of Theoretical Physics, 41, 840

Tan, J. C., & McKee, C. F. 2004, Astrophys. J. , 603, 383

Tegmark, M., Silk, J., Rees, M. J., et al. 1997, Astrophys. J. , 474, 1

Toomre, A. 1964, Astrophys. J. , 139, 1217

Turk, M. J., Abel, T., & O'Shea, B. 2009, Science, 325, 601

Turk, M. J., Clark, P., Glover, S. C. O., et al. 2011, Astrophys. J. , 726, 55

Uehara, H., Susa, H., Nishi, R., Yamada, M., & Nakamura, T. 1996, Astrophys. J. Lett. , 473, L95

Umeda, H., & Nomoto, K. 2003, Nature, 422, 871

Weymann, R. J., & Williams, R. E. 1969, Astrophys. J. , 157, 1201

Whalen, D., O'Shea, B. W., Smidt, J., & Norman, M. L. 2008a, Astrophys. J. , 679, 925

Whalen, D., Van Veelen, B., O'Shea, B. W., & Norman, M. L. 2008b, in IAU Symposium, Vol. 255, IAU Symposium, ed. L. K. Hunt, S. C. Madden, & R. Schneider, 116–120

Wolcott-Green, J., Haiman, Z., & Bryan, G. L. 2011, Monthly Notices Roy. Astron. Soc. , 418, 838

Wright, E. L. 2012, Online Tutorial by Edward Wright on Big Bang Nucleosynthesis: http://www.astro.ucla.edu/ wright/BBNS.html

Yoneyama, T. 1972, Publ. of the Astron. Soc. of Japan, 24, 87

Yoshida, N., Omukai, K., & Hernquist, L. 2008, Science, 321, 669

Yoshida, N., Omukai, K., Hernquist, L., & Abel, T. 2006, Astrophys. J. , 652, 6

Yoshida, N., Sugiyama, N., & Hernquist, L. 2003, Monthly Notices Roy. Astron. Soc. , 344, 481

Zanstra, H. 1934, Monthly Notices Roy. Astron. Soc. , 95, 84

Deposition:

Herewith I declare that I have completed this thesis independently and that I have not used other than the declared sources or materials. Sections that reflect the thoughts or works of others are made known through the definition of sources.

Heidelberg, 22 January 2014 ....